POLITECNICO DI TORINO

Corso di Laurea Magistrale
in Ingegneria Elettrica

Tesi di Laurea Magistrale

System-Level Efficiency Optimization of an Electric Vehicle Traction Drive

Relatore
prof. Paolo Guglielmi

Candidato
Davide Cittanti

Marzo 2018

Acknowledgments

First of all, I would like to thank Brusa Elektronik AG for giving me the opportunity to develop my master thesis in one of the foremost companies in the vehicle electrification field. The stimulating working environment and the availability of well equipped laboratories have significantly contributed to the progress of this dissertation.

Special thanks go to my academic supervisor Prof. Paolo Guglielmi, for his time and experienced advice, especially when mostly needed.

My deepest gratitude goes to my company tutor Riccardo Tinivella. I truly appreciate his interest in my thesis topic and his continuous support during all of my period in Brusa. Every time my work encountered a major roadblock, he has always helped me finding a way through it.

Great thanks go to my friend and colleague Egi, for the amazing and everlasting midnight discussions on power electronics and life philosophy during my stay in Switzerland.

I would also like to acknowledge my friend and course mate Jacopo, who has alleviated my master study days in Torino by forcing me out of home once in a while and getting me to know new places in town. I will never forget our lunch-time talks and our regular unhealthy meals.

I am grateful to my lifelong friends, for being there for me in the moments of need, and to all of the amazing people I've met in my university years, during experiences in Italy and abroad. In a way, they have all contributed to where I am now.

A special thank you goes to my parents and my sister, for their continuous support over the years. None of my studies and achievements could have been possible without them.

Finally, and most importantly, I would like to thank my girlfriend Mimma for her love and understanding during the tough period of my studies. I sure hope to find a better work-lifetime balance in the coming years and to be more present in her life.

Davide Cittanti

Torino, March 2018

Abstract

The automotive sector has recently been on the edge of a drastic structural change due to the advent of vehicle electrification. An increasing number of battery electric (BEV) and hybrid electric (HEV) vehicles is rapidly coming to market. Since batteries are still limited in their energy storage capability and represent a major cost component of the vehicle, the efficiency of the electric traction line becomes of utmost importance. A small increase in the overall system efficiency can directly translate in a smaller battery requirement, thus reducing cost and weight of the vehicle, meanwhile yielding an increase in its range.

The power inverter represents the fundamental energy control unit of an electric vehicle (EV) traction line, since it directly controls the power flow between the battery system and the electrical machine. Power electronic converters in automotive are subject to a strong pressure regarding cost, weight, volume and reliability, thus even the design of a simple 2-level voltage source inverter (VSI) which complies with the required specifics can result in a challenging task. While semiconductor losses represent a relatively small portion of the total system losses, it is extremely important to minimize them, since they directly define the minimum number of paralleled power devices per switch and the overall inverter cooling effort, both of which increase the converter weight, volume and cost.

The electric motor is responsible for the conversion between electrical and mechanical energy, enabling the actual movement of the vehicle. Even though electrical machines are far more efficient than their internal combustion engine (ICE) counterparts, as they normally exceed 90% operating efficiencies, the traction motor still represents the major loss component of the drive train. Therefore, a thorough analysis of the machine loss mechanisms is necessary to face the system efficiency maximization challenge. An optimal motor control strategy is also mandatory to exploit the electrical machine in the best possible way.

The main goal of this work is to provide a comprehensive approach to the optimal design and control of an electric vehicle traction inverter, once a specific motor is chosen or provided. The proposed method tries to define, analyse and quantify the main loss mechanisms of the power converter and the electrical machine, while also investigating their mutual loss interactions. From the inverter design point of view, the aim is to establish the best combinations among the semiconductor device choice, the number of parallel devices per switch, the adopted modulation technique and the operating switching frequency. From the control perspective, the goal is to derive a minimum system loss strategy by deriving the speed-dependent optimal control

trajectories on the motor *dq* current plane. Despite being based on a specific available electrical machine, the proposed holistic approach has general validity and can therefore be extended to other machine types.

Since the main topic of this dissertation regards the maximization of an EV drive train efficiency, accurate and reliable loss models of the system components are needed for the task. First, a semiconductor loss model is derived, based on available manufacturer data. Two different discrete devices are considered, a Si IGBT and a SiC MOSFET, which enable a semiconductor technology comparison. Then, a duty cycle and voltage waveform generation tool is built. Once a modulation technique is implemented, this tool computes the inverter switch duty cycles and generates the output phase voltage waveforms as a function of electrical frequency, switching frequency and reference output voltage value. For the sake of clarity, only a standard continuous modulation technique and an optimal loss clamping discontinuous technique are implemented and compared in this work. From these first two tools it is possible to obtain the inverter output voltage spectrum and the averaged semiconductor losses for a generic load condition (i.e. combination of voltage, current and power factor angle) and operating switching frequency. Moreover, a thermal model of the discrete devices mounted on a liquid-cooled heat sink is built, in order to estimate the semiconductor junction temperature in each operating condition. This allows to establish the minimum number of parallel devices per switch required by the inverter, by considering the worst case application-specific loss condition (i.e. maximum current).

The motor performance and loss models are derived by means of a combination of FEM simulations, to extract flux linkage maps and estimate iron losses, and direct measurements, to obtain the winding resistance, quantify mechanical friction losses and estimate high-frequency time-harmonic losses caused by the inverter supply distortion. For this last purpose, a high-frequency motor loss model is built, capable of estimating the amount of motor harmonic losses as a direct function of the inverter output phase voltage spectrum.

Since the only two system loss components which depend on the switching frequency are the inverter switching losses and the motor time-harmonic losses, which respectively increase and decrease with switching frequency, the presented models can be leveraged to find the optimal trade-off between the two. Therefore, the optimal switching frequency value for a certain inverter design (i.e. choice of semiconductor technology, number of parallel devices per switch, modulation technique) and operating condition (i.e. output voltage and current) can be identified.

A vehicle model is also necessary to complete the system optimization procedure and the reason is double. First, the vehicle specifics and performance requirements define the highest machine overload torque condition, which can directly be translated into the inverter rated current and thus in the minimum number of paralleled semiconductor devices per switch. Second, the combination between the vehicle model and a proper driving cycle profile yields a cloud of the most relevant application-specific load working points. This knowledge is fundamental to effectively choose the optimal operating switching frequency of the inverter. Since this value highly depends on the load condition, weighting this choice on the most relevant working points represents the best possible solution.

Furthermore, the implemented loss models allow to derive inverter and motor losses as a function of the *dq* axis currents and the machine speed. Therefore, it is possible to introduce a motor control strategy which optimizes the overall system efficiency, by minimizing the sum of each “controllable” loss component (i.e. inverter conduction and switching losses, motor copper, iron and time-harmonic losses). As a result, the whole motor torque-speed operating range can be mapped by means of minimum system loss trajectories in the *dq* current plane, yielding a system-level minimum-torque-per-loss (MTPL) control strategy.

With every subsystem model available, a wide optimization procedure is performed and the resulting set of optimal inverter designs is represented by means of efficiency vs cost (η - €) Pareto fronts, where the efficiency is weighted on the vehicle operating points and the cost is proportional to the number of parallel semiconductor devices per switch. One curve is extracted for each semiconductor technology, inverter modulation technique and motor control strategy, while the optimal inverter switching frequency is identified in each case. The results show that the loss-optimal switching frequency value drastically depends on the inverter design combination, reaching values higher than 70 kHz if SiC MOSFET adoption is combined with a discontinuous modulation strategy, while remaining below 30 kHz if Si IGBTs are used.

Finally, one out of the multiple Pareto-optimal inverter designs is selected and the whole traction line efficiency performance is evaluated over the considered driving cycle, while adopting the optimized MTPL control strategy. These results are then compared to a conventional inverter design (i.e. IGBT devices, continuous modulation, 10 kHz) with a standard maximum-torque-per-ampere (MTPA) control strategy, to highlight the enabled loss performance improvements.

Notation

Symbols

A_{f}	vehicle frontal area (m^2)
$A_{\mathrm{th,c\text{-}f}}$	thermal interface area between case and heatsink (mm^2)
B	peak flux density (T)
B_h	h-order harmonic average flux density peak value (V)
C_{r}	vehicle tire rolling coefficient
C_{x}	vehicle drag coefficient
$E_{\mathrm{D,fr}}$	diode forward recovery energy loss (J)
$E_{\mathrm{D,rr}}$	diode reverse recovery energy loss (J)
$E_{\mathrm{T,off}}$	transistor turn-off energy loss (J)
$E_{\mathrm{T,on}}$	transistor turn-on energy loss (J)
E_{off}	semiconductor device turn-off energy loss (J)
E_{on}	semiconductor device turn-on energy loss (J)
F	vehicle total motive force (N)
F_{a}	vehicle aerodynamic drag force (N)
F_{c}	vehicle climbing resistance (N)
F_{r}	vehicle rolling resistance (N)
I	phase current peak value (A)
I_{DS}	semiconductor device drain-to-source current (A)

I_{S1}	peak value of the maximum motor phase current in continuous operation (A)
I_{lim}	peak value of the inverter current limit (A)
I_{max}	maximum peak phase current (A)
I_{ref}	semiconductor device reference on-state current (A)
I_{rrm}	diode reverse recovery peak current (A)
I_h	h-order harmonic current peak value (A)
J_{m}	motor inertia ($\mathrm{kg\,m^2}$)
J_{w}	vehicle wheel inertia ($\mathrm{kg\,m^2}$)
LF	harmonic loss factor ($\mathrm{W/V^2}$)
L_{e}	motor reflected inductance (H)
L_d	d-axis inductance (H)
L_q	q-axis inductance (H)
M	loaded vehicle mass (kg)
M_{eq}	vehicle equivalent mass (kg)
N_{par}	number of paralleled semiconductor devices per switch
P	motor power (W)
P_{Cu}	motor copper losses (W)
P_{Fe}	motor iron losses (W)
P_{cond}	semiconductor averaged conduction losses (W)
P_{harm}	motor time-harmonic losses (W)
P_{m}	motor mechanical losses (W)
P_{pm}	motor permanent magnet losses (W)
P_{sw}	semiconductor averaged switching losses (W)
$P_{\mathrm{tot,D}}$	diode averaged total losses (W)
$P_{\mathrm{tot,T}}$	transistor averaged total losses (W)
$P_{\mathrm{Fe,eddy}}$	iron eddy-current loss component (W)

$P_{\mathrm{Fe,hys}}$	iron hysteresis loss component (W)
Q_{rr}	diode reverse recovery charge (C)
R_{e}	motor reflected resistance (Ω)
R_{s}	stator phase winding resistance (Ω)
$R_{\mathrm{th,c\text{-}f}}$	case-to-fluid thermal resistance (K/W)
$R_{\mathrm{th,j\text{-}c}}$	junction-to-case thermal resistance (K/W)
R_{w}	vehicle wheel radius (m)
T	motor torque (Nm)
T_0	dwell time of the zero vector (s)
T_1	electrical fundamental period (s)
T_{c}	semiconductor device case temperature (°C)
T_{f}	cooling fluid temperature (°C)
$T_{\mathrm{j,D}}$	diode chip junction temperature (°C)
$T_{\mathrm{j,T}}$	transistor chip junction temperature (°C)
T_{j}	semiconductor junction temperature (°C)
T_{m}	motor mechanical resistive torque (Nm)
T_{pm}	permanent magnet contribution to the motor torque (Nm)
T_{r}	reluctance contribution to the motor torque (Nm)
T_a	dwell time of the first vector of the sector (s)
T_b	dwell time of the second vector of the sector (s)
T_s	sampling or switching period (s)
V	phase voltage peak value (V)
V_{DS}	semiconductor device drain-to-source voltage (V)
V_{dc}	DC-link voltage (V)
V_{lim}	peak value of the inverter voltage limit (V)
V_{max}	maximum peak amplitude of the phase voltage (V)
V_{ref}	semiconductor device reference off-state voltage (V)

V_h	h-order harmonic voltage peak value (V)
Z_e	motor reflected impedance (Ω)
δ	skin depth in the iron lamination (m)
η	total system efficiency (%)
η_g	gearbox efficiency (%)
γ	road grade angle (rad)
λ_d	d-axis flux linkage (V s)
λ_q	q-axis flux linkage (V s)
μ_0	magnetic permeability of vacuum (H/m)
$\mu_\mathrm{r,Fe}$	relative magnetic permeability of the core material (H/m)
ω	fundamental angular velocity (rad/s)
ω_m	motor mechanical angular speed (rad/s)
ρ_Fe	electrical resistivity of the iron lamination (Ω m)
ρ_air	air density (kg/m^3)
$\sigma_\mathrm{th,h}$	heatsink specific thermal conductivity (W/m^{2}K)
$\sigma_\mathrm{th,s}$	insulation sheet specific thermal conductivity (W/m^{2}K)
τ	vehicle motor-to-wheel transmission ratio
θ	angle between $\vec{V}$ and the first space vector of the sector (rad)
$\underline{\mu}_\mathrm{e}$	complex magnetic permeability of the core (H/m)
φ	power factor angle (°)
$\vec{L}_{dq}$	dq axis inductance matrix (H)
$\vec{V}$	reference voltage vector (V)
$\vec{\lambda}_\mathrm{pm}$	permanent magnet flux linkage vector (V s)
$\vec{\lambda}_{dq}$	dq flux linkage vector (V s)
$\vec{i}_{dq}$	dq current vector (A)
$\vec{v}_{dq}$	dq voltage vector (V)
a	vehicle acceleration (m/s^2)

dI_{rr}/dt	diode reverse recovery peak current-fall slope (A/s)
f	electrical fundamental frequency (Hz)
f_{sw}	inverter switching frequency (Hz)
f_h	h-order harmonic frequency (Hz)
g	gravitational acceleration (m/s^2)
i_d	d-axis current (A)
i_q	q-axis current (A)
m	inverter modulation index
n	motor speed (rpm)
n_{max}	motor maximum rotational speed (rpm)
p	motor pole pair number
p_{Fe}	specific iron losses (W/kg)
p_{cond}	semiconductor instantaneous conduction losses (W)
p_{sw}	semiconductor instantaneous switching losses (W)
t_{a}	diode reverse recovery current-rise time (s)
t_{b}	diode reverse recovery current-fall time (s)
t_{rr}	diode reverse recovery time (s)
u	vehicle speed (m/s)
u_{max}	vehicle top speed (m/s)
v_d	d-axis voltage (V)
v_q	q-axis voltage (V)

Abbreviations

BEV	Battery Electric Vehicle
CBPWM	Carrier-Based Pulse Width Modulation
CPSR	Constant Power Speed Range
CSI	Current Source Inverter

EMF	Electromotive Force
EV	Electric Vehicle
FEM	Finite Element Method
FFT	Fast Fourier Transform
GaN	Gallium Nitride
HDF	Harmonic Distortion Factor
HEV	Hybrid Electric Vehicle
ICE	Internal Combustion Engine
IGBT	Insulated Gate Bipolar Transistor
IM	Induction Motor
IPM	Interior Permanent Magnet
LUT	Look-Up Table
MOSFET	Metal Oxide Semiconductor Field Effect Transistor
MTPA	Maximum Torque Per Ampere
MTPL	Maximum Torque Per Loss
NdFeB	Neodymium Iron Boron
PCB	Printed Circuit Board
PHEV	Plug-in Hybrid Electric Vehicle
PM	Permanent Magnet
PMASR	Permanent Magnet Assisted Synchronous Reluctance
PMSM	Permanent Magnet Synchronous Motor
PWM	Pulse Width Modulation
RMS	Root Mean Square
SaCo	Samarium Cobalt
Si	Silicon
SiC	Silicon Carbide
SPM	Surface Permanent Magnet

SVM	Space Vector Modulation
SyR	Synchronous Reluctance
THD	Total Harmonic Distortion
UGO	Uncontrolled Generator Operation
VSI	Voltage Source Inverter
WLTC	Worldwide harmonized Light-vehicle Test Cycle
WTHD	Weighted Total Harmonic Distortion

Contents

Chapter 1

Introduction

ELECTRIFICATION represents nowadays the major trend of the automotive industry. In order to comply with increasingly strict CO_2 and pollutant emission regulations, car manufacturers are starting to embrace a higher level of on-board "electrical power", which allows to enhance the vehicle overall fuel efficiency. Developed to address this concern, hybrid electric vehicles (HEVs) have been in the market for quite some time, combining the internal combustion engine (ICE) advantages (i.e. proven technology, long range, low refueling times) with some additional features enabled by the drive train electrification, such as start & stop and regenerative braking. Increasing benefits are obtainable by higher degrees of hybridization, such as the capability of driving in full electric mode for a certain distance and even recharge the on-board battery by means of an external plug, such as in plug-in HEVs (PHEVs). The highest level of drive train electrification is obtained by completely removing the ICE, leading to a vehicle with a fully electric traction line, commonly known as battery electric vehicle (BEV).

BEVs normally show better dynamical performance than their ICE vehicle counterparts, due to the availability of the maximum motor torque at standstill, typical of electrical machines. However, cost parity between corresponding fully electric and conventional vehicles has not yet been reached and it represents a major challenge to be addressed, in order to enable a mainstream adoption of BEVs. The main responsible for this cost difference is the high-voltage traction battery, which represents the single major cost component of a BEV. As of today, batteries face technological limitations in terms of energy density, considerably increasing the weight of the vehicle to achieve an acceptable amount of range. In general, weight is a key performance indicator in automotive: a greater mass requires higher power when accelerating or going uphill (energy which can never be completely recovered), worsens vehicle performance and leads to a stronger chassis construction. Fortunately BEV running costs, related to the vehicle energy consumption and the electricity price, are normally lower than a corresponding ICE vehicle ones and thus help offsetting the initial purchase cost difference. Nevertheless electricity is still not free and, on the contrary, in most European countries can be quite expensive (~ 0.20 €/kWh).

While the purchase cost is of great importance for passenger vehicles, running costs are the most critical aspect for commercial vehicles. Anyway, both cost components can be reduced by improving the overall vehicle efficiency. A higher efficiency yields an increase in the vehicle range for a given battery size or a reduction of the battery size (i.e. reduced purchase cost and weight) for a given amount of range. Lower power losses also mean a decreased energy consumption and thus a lower vehicle running cost.

Specific vehicle design measures can be adopted to reduce the energy required to move the vehicle in the first place. Achieving a more aerodynamic profile and reducing the weight of the vehicle (e.g. by making use of lighter materials in the chassis) both play a big role in increasing "fuel" efficiency. Another major contributor to the vehicle consumption is the energy wasted in the traction line inefficiencies, since each drive train subcomponent (i.e. battery, power converter, motor, gearbox) generates losses during operation. These losses not only reduce the vehicle efficiency, translating in the aforementioned cost consequences, but also increase the temperature of the components, thus requiring adequate cooling systems to remove the loss-generated heat and keep the devices in their functional operating conditions. While being far more efficient than their ICE counterparts, electric traction lines still show room for improvements, which may be obtained by means of adequate design choices and operating strategies. The potential benefit of improving the drive train efficiency is therefore clear, since decreasing losses can translate in further weight, cost and efficiency gains for the vehicle.

1.1 Aim of the Work

The electrical part of a BEV drive train (i.e. excluding the mechanical gearbox) consists of three main subsystem, illustrated in figure 1.1. It is important to note that a BEV can be equipped with more than one motor-inverter pair, in order to enhance the vehicle performance and provide a four-wheel drive capability, however the drive train concept is exactly the same.

The last component, the electric motor, is responsible for the conversion between electrical and mechanical energy and thus enables the actual movement of the vehicle. Electrical machine efficiencies, normally exceeding 90% operating values, are far superior than their ICE counterparts, however the traction motor still represents the drive train component with the highest losses and it is thus very important to identify and address its loss mechanisms.

The motor is supplied by a power electronic converter (i.e. the traction inverter), which feeds the machine stator winding with a variable-amplitude, variable-frequency voltage. The inverter represents the fundamental energy control unit of an electric vehicle traction line, since it can adjust the power flow between the battery system and the electrical machine. The bidirectional power capability of the converter is of utmost importance, since it allows to recover part of the vehicle braking energy (i.e. the so called "regenerative braking"), considerably increasing the fuel efficiency during city driving. Even though the semiconductor losses inside the traction inverter represent a relatively small portion of the total system losses, it is extremely important to minimize them, since they directly define the required number of semiconductor devices and the overall inverter cooling effort, both of which increase the converter weight, volume and cost.

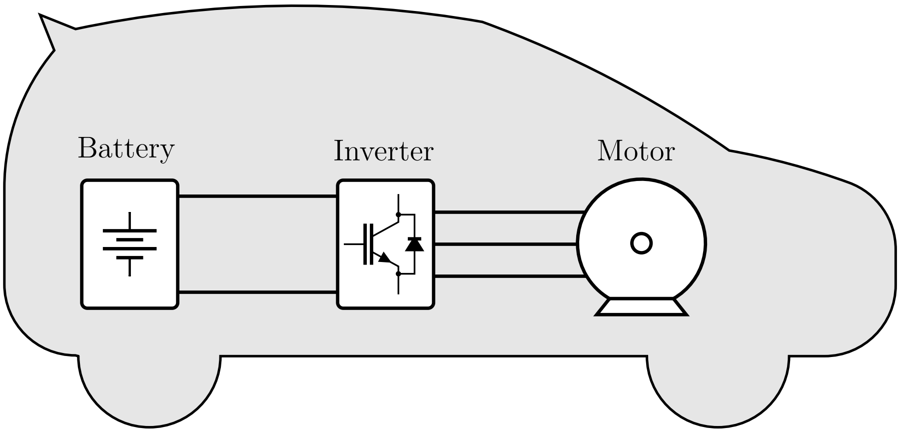

Figure 1.1: Schematic of the traction drive line of an EV, divided in its subsystems.

Finally, the inverter sources the power to supply the traction motor from the high-voltage battery, which represents the vehicle main energy storage element. Battery losses are related to the instantaneous vehicle power request and the chemical processes inside the cells (which determine the battery equivalent series resistance), therefore the efficiency of this subsystem cannot be improved by means of design procedures or control strategies. Once a battery cell chemistry and a total energy storage capacity are chosen, the battery system capabilities in terms of performance and efficiency are determined.

For the aforementioned reasons, this dissertation focuses on the efficiency optimization of the traction inverter and motor subsystems. The main goal of this thesis is to provide a holistic approach to minimize the drive train power losses of a BEV, by means of both design choices and control strategies. The proposed method tries to define, analyse and quantify the main loss mechanisms of the power converter and the electrical machine. While these subsystems are normally optimized individually, some loss mechanisms are generated by their mutual interaction and a true system-level efficiency optimization must take these loss components into account.

From the inverter design point of view, the aim is to establish the best combinations among the semiconductor device choice, the number of paralleled devices per switch, the adopted modulation technique and the operating switching frequency. Inverter filtering components are not considered, since they would overcomplicate the optimization procedure and would go beyond the purpose of this work. Moreover, the motor is not subject to design, since this would open a whole different topic, thus an available electrical machine is chosen. The inverter design is therefore optimized for the selected motor, but the proposed approach has general validity and can be extended to any electrical machine.

From the control perspective, the goal is to derive a minimum system-loss strategy by mapping the speed-dependent optimal control trajectories on the motor *dq* current plane. A model-based control strategy of this kind requires an accurate knowledge of the loss mechanisms of both the power converter and the electrical machine, together with their dependence on operating conditions. Precise loss models are needed, therefore their derivation takes up a great part of this thesis.

Overall, this work presents the design procedure of a traction inverter that meets the vehicle performance requirements and optimizes the drive train efficiency by means of a minimum system-loss control strategy. Although this method is proposed for a specific case study, the here built subsystem models and optimization tools have broader validity. The procedure can be thus extended to a wide range of applications.

1.2 Outline of the Thesis

In order to carry out a system-level efficiency optimization of the whole drive train, accurate and reliable loss models of the system components are needed. This thesis is thus organized in a way that first describes the developed models and finally interlinks them for the total system analysis.

In **chapter 2** the inverter model is described. First, a three-phase 2-level voltage source inverter (VSI) topology is selected. Two discrete power semiconductor devices, belonging to different technologies, are chosen for a performance comparison. Making use of the available manufacturer data, a semiconductor loss model is derived, in order to enable the evaluation of both conduction and switching losses of a generic power device. An inverter thermal model from the semiconductor chip to the liquid-cooled heat sink is also built, to estimate the semiconductor device junction temperature during operation, thus enabling a proper inverter dimensioning (i.e. number of parallel devices per switch) once a worst-case current is specified. Furthermore, a duty cycle and voltage waveform generation tool is created and two different inverter modulation techniques are implemented (i.e. a standard continuous modulation technique and an optimal loss clamping discontinuous technique). This tool computes the inverter switch duty cycles and generates the output phase voltage waveforms as a function of electrical frequency, switching frequency and reference output voltage value. Combining the semiconductor loss model and the voltage waveform generation tool, it is therefore possible to obtain the inverter output voltage spectrum and the averaged semiconductor losses for a generic load condition (i.e. combination of voltage, current and power factor angle) and operating switching frequency. A performance comparison between the two modulation techniques, concerning output voltage harmonic distortion and semiconductor device power losses, is provided in the end of the chapter.

In **chapter 3** the electrical machine loss mechanisms are investigated and the motor model is derived. An available motor is chosen for the case-study, the specific machine topology is described and its electrical and magnetic equations are illustrated. The motor flux and torque maps are then extracted by means of finite element analysis and the peculiar magnetic behaviour of the selected machine is highlighted. Moreover, inverter voltage and current limits are translated into boundary conditions for the motor operating region in the dq current plane. Maximum torque-speed and power-speed curves of the machine are therefore extracted as a function of the inverter rated current. Then, the motor loss mechanisms are described and evaluated, by means of both finite element analysis and measurements, starting from fundamental copper, iron and permanent magnet losses, together with mechanical friction losses. Apart from these loss components, some power losses are generated by the mutual linkage between the power converter and the electrical machine. The inverter induces additional losses in the motor by supplying it with a high-frequency switched output voltage waveform with increased harmonic content. These losses are also known as time-harmonic losses and an attempt at modeling them is carried out, based on the high-frequency machine impedance measurement. This model enables to estimate the total time-harmonic loss contribution as a function of the inverter voltage waveform spectrum. Therefore, the effect of the two different modulation techniques on the additional inverter-induced motor losses can be evaluated.

In **chapter 4** a vehicle model is built, in order to provide the necessary specifics for the inverter dimensioning and some realistic drive train operating conditions for the system-level optimization procedure. The basic equations regarding dynamical resistance to motion are detailed, therefore the necessary force to move the vehicle in different operating conditions can be identified. A reference vehicle is chosen for the investigation and its main data and performance specifics are illustrated. The vehicle performance constraints are then translated into the required motor overload torque capability and thus into the minimum inverter rated current value. Furthermore, a standardized driving cycle profile is selected for an operating condition investigation. The vehicle dynamical model is thus exploited to identify the cloud of most relevant application-specific drive train working points. These points are then clustered and gathered together into a lower number of time-weighted representative points, to be employed in the subsequent optimization procedure.

In **chapter 5** the model-based system-level optimization procedure is described. The loss models of the power converter and the electrical machine, derived in the previous chapters, are interlinked. Therefore, the power losses of the complete drive train system can now be calculated, as a function of the operating condition and the chosen switching frequency. Since the only two system loss components which depend on the switching frequency are the inverter switching losses and the motor time-harmonic losses, which respectively increase and decrease with this design parameter, the aforementioned loss models can be leveraged to find the optimal trade-off between the two. Therefore, the optimal switching frequency value for a certain inverter design (i.e. choice of semiconductor technology, number of paralleled devices per switch, modulation technique) and operating condition (i.e. output voltage and current) can be identified. Furthermore, the derived loss models allow to express inverter and motor losses as a function of the machine *dq* axis currents and rotational speed. By combining these loss maps, it is possible to introduce a motor control strategy which optimizes the overall system efficiency, minimizing the sum of each “controllable” loss component (i.e. inverter conduction and switching losses, motor copper, iron and time-harmonic losses). As a result, the whole motor torque-speed operating range is mapped by means of minimum system loss trajectories in the *dq* current plane, yielding a maximum system efficiency control strategy. With the availability of the most relevant drive train working points, the subsystem loss models and the optimal control strategy, the system-level efficiency optimization procedure is performed and the resulting set of optimal inverter designs is represented by means of efficiency vs cost (η - €) Pareto curves, where the efficiency is weighted on the vehicle operating points and the cost is proportional to the number of parallel semiconductor devices per switch. One curve is extracted for each semiconductor technology and inverter modulation technique, while the optimal inverter switching frequency is identified in each case. Finally, one out of the many Pareto-optimal inverter designs is selected and the whole drive train efficiency performance is evaluated along the considered driving cycle, while adopting the optimized control strategy. These results are then compared to a conventional inverter design with a standard motor control strategy, to highlight the achievable system efficiency improvements.

In **chapter 6** the results of the thesis are summarized and an outlook on possible future work is provided.

Chapter 2

Inverter Model

THE power inverter is the fundamental energy control unit of the EV traction line. Its main function is to convert the available DC battery voltage into three (or more) sinusoidal phase voltages of adjustable frequency and amplitude to drive the traction motor. While the electrical machine has no built-in "intelligence", the power converter does, and it can control the whole drive train power flow. Therefore, any kind of control strategy (i.e. minimum system loss in the present case) must be performed by the inverter itself.

Even though inverters all perform the same voltage-conversion task, many different design solutions exist and identifying the absolute best between them is not straightforward. The first choice that an inverter designer must face regards the *number of output phases* of the converter. This choice is normally dictated by the electrical machine. While three-phase motors are usually adopted, the automotive market is increasingly prone to multiphase solutions [1, 2]. The present work is based on an available three-phase electric motor, therefore the inverter phase number does not represent a decision variable. The second choice regards the *number of levels* by which the output voltage waveform is synthesized: this defines the inverter leg topology. Since BEV drive trains normally work with battery voltages in the range of hundreds of volts, the suitable inverter level number is restricted to 2 or 3. Incrementing levels increases the number of semiconductor devices and driver circuits, while yielding little to no advantages in the system efficiency or power density. An extended comparison between 2-level and 3-level converters for low-voltage variable speed drives is presented in [3, 4] and is not object of this thesis. Since power electronics for automotive is subject to strong cost and reliability pressure, the simplest inverter topology is usually adopted and thus constitutes the choice for this work.

A schematic of the 2-level inverter is shown in figure 2.1. Each one of the three legs has an output terminal in between an upper and a lower switch. These power switches are made up by a transistor (T) and an anti-parallel diode (D), which provide a bidirectional current capability. An input DC-link capacitor is present to smooth the generated current ripple and thus prevent it from reaching the battery.

Throughout this dissertation, the inverter design procedure is considered as a combination of different choices: the adopted semiconductor technology, the number of parallel devices per switch, the implemented modulation strategy and the operating switching frequency. This chapter derives and explains the proposed inverter model.

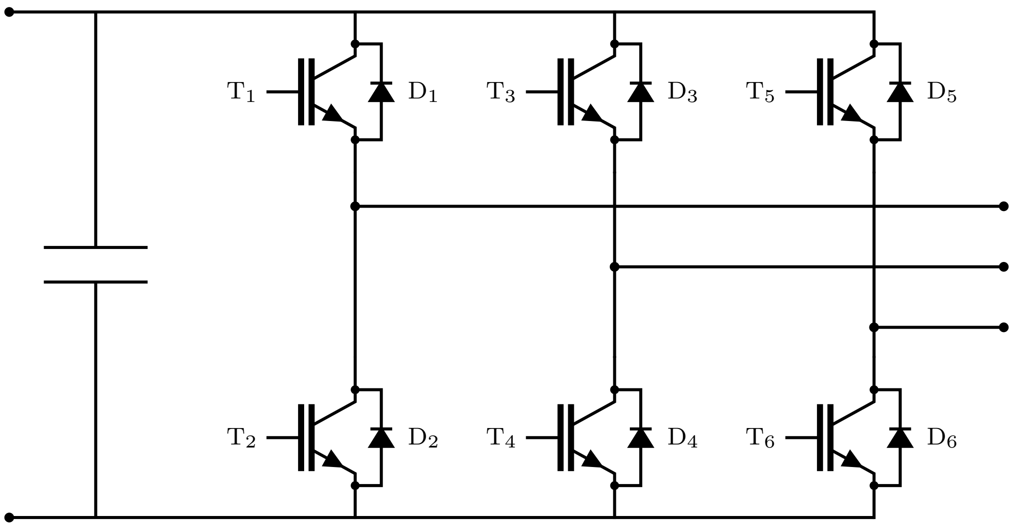

Figure 2.1: Three-phase inverter circuit schematic.

2.1 Semiconductor Devices

Nowadays, industrial three-phase inverters normally adopt insulated gate bipolar transistors (IGBTs) as their switching units. These devices, due to their bipolar nature, show high current capability and high breakdown voltage, together with a considerable switching speed. Despite the continuous improvement of IGBT technology, enhancing both conduction and switching performance, new devices based on modern semiconductor materials, such as Silicon Carbide (SiC) and Gallium Nitride (GaN), are rapidly entering the market. The main candidate which is targeting high power applications, up to now dominated by IGBTs, is the SiC MOSFET. This device is also characterized by high current rating and high voltage breakdown, but it is much more suited for high switching frequencies compared to IGBTs. Another advantage of this technology resides in the SiC capability of withstanding high temperatures (theoretically up to $\sim$ 400 °C). However, this feature has yet to be exploited, since, as of now, no packages suited to sustain similar temperatures exist. It is worth mentioning that SiC chips have a far greater cost per unit area in respect to Silicon (Si) and, although their higher performance helps lowering the required total die area, their overall benefit advantage varies and remains to be proven for different applications [5].

Although a large database of semiconductor devices would gather the best out of the presented optimization process, for clarity reasons only two devices (i.e. one IGBT and one SiC MOSFET) have been selected for this investigation. Still, a performance comparison between the two different semiconductor technologies can be carried out. The main characteristics of the two discrete devices are summarized in table 2.1. Since a fixed DC-link voltage of 400 V is considered throughout this work, both devices have been chosen with a 650 V breakdown voltage. It is also worth noting that, while the SiC MOSFET performance are moderately better than the IGBT ones (as will be shown in the following), its purchase cost is roughly $\sim$ 9 times higher.

Table 2.1: IGBT co-pack [6] and SiC MOSFET [7] device main data.

	IGBT co-pack	**SiC MOSFET**
Manufacturer	Infineon Technologies	ROHM Semiconductor
Model number	AIKW50N65DF5	SCT3022AL
Package	TO-247	TO-247
Blocking voltage	650 V	650 V
Rated current	50 A	93 A
Maximum junction temperature	175 °C	175 °C
Thermal resistance ($R_{\text{th,j-c}}$)	T: 0.55 K/W D: 1.50 K/W	0.34 K/W
Thermal interface area ($A_{\text{th,c-f}}$)	200 mm^2	200 mm^2
Purchase Cost[1]	3.21 €	28.18 €

[1]quote for 1000 pieces

2.2 Semiconductor Loss Model

The semiconductor loss model derived in this section is based on available device datasheet information, directly provided by manufacturers. Therefore, no measurements are required. While this approach neglects the final PCB circuit layout influence on the switching losses of the devices, it allows to easily compare large databases of components by simply importing the specifics provided in their datasheets.

It is important to mention that this model disregards the change in the device performance caused by the semiconductor junction temperature variation. As a consequence, temperature is not considered as a design variable in the optimization process. The main reason behind neglecting this dependence is to alleviate the proposed model and thus speed-up the optimization process. Since losses and junction temperature depend one from the other, the semiconductor loss and thermal models would have to be combined inside an iterative process, just to find a steady-state solution. This process would be needed at the lowest stage of the optimization process, causing an unacceptable increase in computation time. As higher temperature values normally worsen the device conduction and switching characteristics, the worst-case junction temperature from a loss stand-point coincides with the highest junction temperature available. Since manufacturer datasheets normally provide the device characteristics at 150 °C, the semiconductor loss model shown in the following will be based on these data. Moreover, the loss dependence on the junction temperature will be omitted from the equations.

A simple schematic of the IGBT (co-packed with an anti-parallel diode) and the SiC MOSFET are shown in figure 2.2. Since the two devices have different naming conventions for their output pins, collector (C) and emitter (E) of the IGBT will be called drain (D) and source (S) in the following, in order to keep the same notation between the two devices.

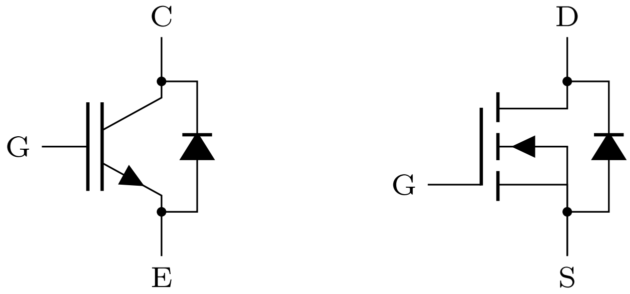

Figure 2.2: Circuit schematics of an IGBT with its anti-parallel diode (left) and a SiC power MOSFET with its body diode (right).

2.2.1 Conduction Losses

Conduction losses derive from the non-ideal on-state behaviour of the semiconductor device. Figure 2.3 shows both forward and reverse conduction characteristics of the two selected power devices. It is worth mentioning that the reverse conduction characteristic of the IGBT belongs to its co-packed anti-parallel diode, since the IGBT is unable to conduct current in the reverse direction. On the contrary, the reverse conduction characteristic of the MOSFET includes the parallel between the semiconductor channel (when the device is turned on) and the natural body diode embedded in the MOSFET structure. Overall, it is shown that the SiC MOSFET conduction behaviour is consistently better than the IGBT one over most of the operating range, especially at low load.

The instantaneous power lost during the on-state depends on the current flowing

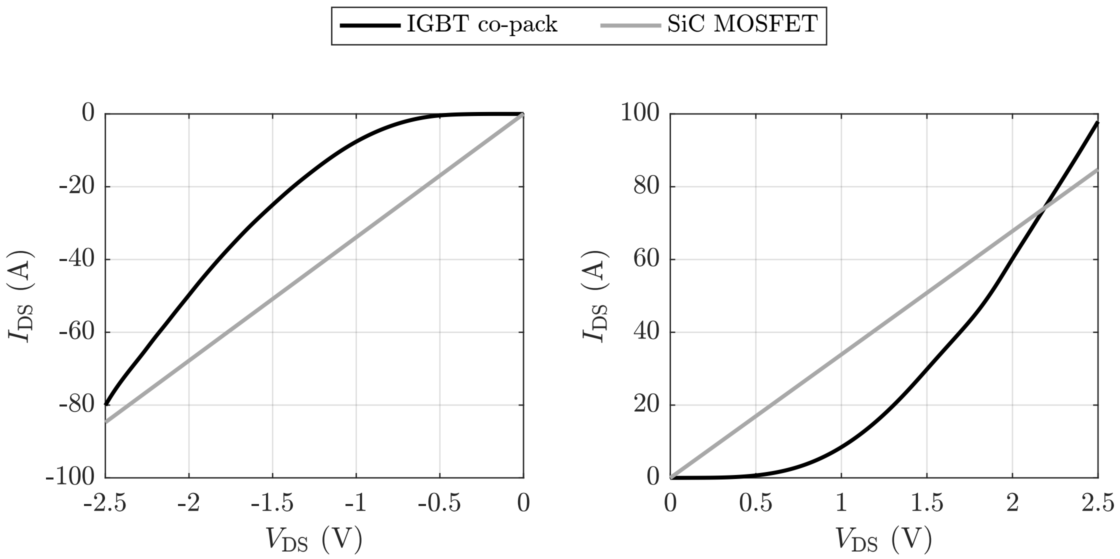

Figure 2.3: Reverse conduction characteristic (left) and forward conduction characteristic (right) of the selected power devices.

through the device and the semiconductor junction temperature (here disregarded):

$$p_{\text{cond}}(t) = I_{\text{DS}}\, V_{\text{DS}}(I_{\text{DS}}) \tag{2.1}$$

Where I_{DS} and V_{DS} are the device drain-to-source current and voltage respectively. The relationship $V_{\text{DS}}(I_{\text{DS}})$ has been implemented by means of a look-up table (LUT). The averaged conduction losses over the electrical fundamental period T_1 can be calculated as:

$$P_{\text{cond}} = \frac{1}{T_1}\int_0^{T_1} p_{\text{cond}}(t)\, dt \tag{2.2}$$

2.2.2 Switching Losses

Switching losses are caused by the instantaneous overlap of non-zero voltage and non-zero current values during the turn-on and turn-off switching transitions of the device. It is worth reminding that switching losses depend on the exact circuit configuration in which the device is operated, therefore different PCB layouts lead to different switching loss values. Although, in order to allow a uniform comparison, the semiconductor devices are considered in the exact same configuration provided by the manufacturer.

The energy lost during a switching transition depends on different parameters, such as the off-state voltage across the device, the on-state current through the device and the semiconductor junction temperature (here disregarded):

$$E_{\text{on}}(I_{\text{DS}}, V_{\text{dc}}) = \begin{cases} E_{\text{T,on}}(I_{\text{DS}}) \left(\dfrac{V_{\text{dc}}}{V_{\text{ref}}}\right) & I_{\text{DS}} > 0 \\ E_{\text{D,fr}} \approx 0 & I_{\text{DS}} < 0 \end{cases} \tag{2.3}$$

$$E_{\text{off}}(I_{\text{DS}}, V_{\text{dc}}) = \begin{cases} E_{\text{T,off}}(I_{\text{DS}}) \left(\dfrac{V_{\text{dc}}}{V_{\text{ref}}}\right) & I_{\text{DS}} > 0 \\ E_{\text{D,rr}} \left(\dfrac{I_{\text{DS}}}{I_{\text{ref}}}\right)^{0.6} \left(\dfrac{V_{\text{dc}}}{V_{\text{ref}}}\right)^{0.6} & I_{\text{DS}} < 0 \end{cases} \tag{2.4}$$

E_{on} and E_{off} are the semiconductor device turn-on and turn-off energy losses, $E_{\text{T,on}}$ and $E_{\text{T,off}}$ are the transistor turn-on and turn-off energy losses, $E_{\text{D,fr}}$ and $E_{\text{D,rr}}$ are the diode forward recovery and reverse recovery energy losses. Moreover, V_{dc} is the inverter DC-link voltage and V_{ref} and I_{ref} are the reference off-state voltage and on-state current at which the transistor switching energy loss curves ($E_{\text{T,on}}$, $E_{\text{T,off}}$) have been measured by the manufacturer.

Equation (2.3) shows that the diode forward recovery energy can normally be neglected, while equation (2.4) extrapolates the reference diode reverse recovery energy for different on-state current and off-state voltage values according to [8]. Since most of the manufacturer datasheets do not directly provide diode reverse recovery energy, the following relationship can be adopted in such cases [9]:

$$E_{\text{D,rr}} = \frac{V_{\text{dc}}\, I_{\text{rrm}}\, t_{\text{b}}}{4} \tag{2.5}$$

where

$$t_{\mathrm{b}} = \frac{I_{\mathrm{rrm}}}{dI_{\mathrm{rr}}/dt} \tag{2.6}$$

This expression is based on the simplifying current and voltage waveforms shown in figure 2.4, where I_{rrm} is the peak reverse recovery current, dI_{rr}/dt is the peak reverse recovery current fall slope, while t_{a}, t_{b} and t_{rr} are the reverse recovery current-rise, current-fall and total times respectively. It must be noted that all of this quantities are always present in the device datasheet.

The I_{DS} dependence of the switching energy loss components is shown in figure 2.5 and has been implemented in the semiconductor loss model by means of a LUT. Figure 2.6 shows a comparison between the total switching energy losses of the selected IGBT co-pack and SiC MOSFET, revealing a ~ 3 times difference between the two. Moreover, it is worth highlighting that both curves have a lower than linear behaviour at low current values (where the diode reverse recovery loss dominates) and a higher than linear behaviour at high current values (where the transistor losses dominate). This effect is particularly important when adding semiconductor devices in parallel, since a lower than linear loss dependence on current means that two devices in parallel yield higher switching losses than one single device. Therefore, from a switching loss point of view, it is no longer useful to add devices in parallel when the linearity threshold in the switching loss curve is reached.

Since the instantaneous power lost in the switching transitions is proportional to the switching frequency of the device, the following expression is obtained:

$$p_{\mathrm{sw}}(t) = f_{\mathrm{sw}} \Big(E_{\mathrm{on}}(I_{\mathrm{DS}}, V_{\mathrm{dc}}) + E_{\mathrm{off}}(I_{\mathrm{DS}}, V_{\mathrm{dc}}) \Big) \tag{2.7}$$

Where f_{sw} is the switching frequency. The averaged switching loss over the fundamental period can be calculated as:

$$P_{\mathrm{sw}} = \frac{1}{T_1} \int_0^{T_1} p_{\mathrm{sw}}(t)\, dt \tag{2.8}$$

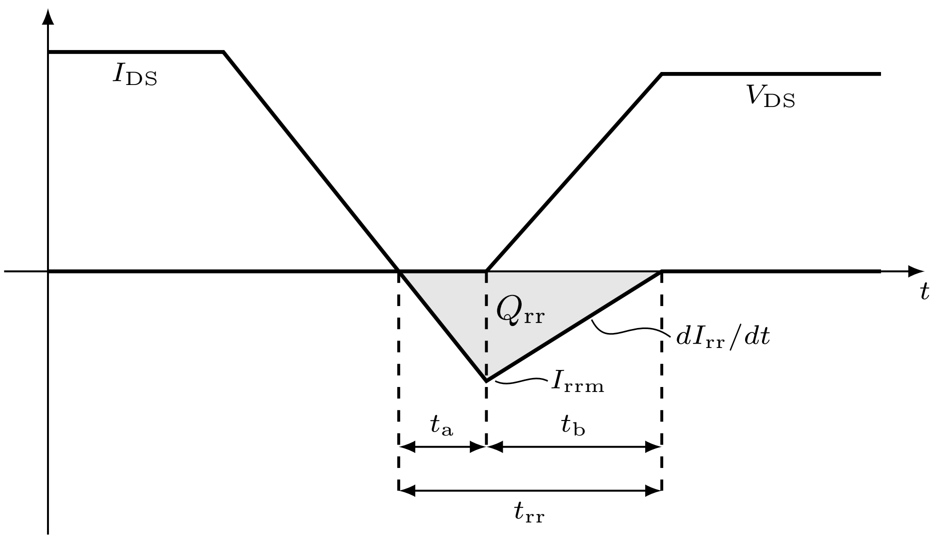

Figure 2.4: Diode reverse recovery simplified current and voltage waveforms.

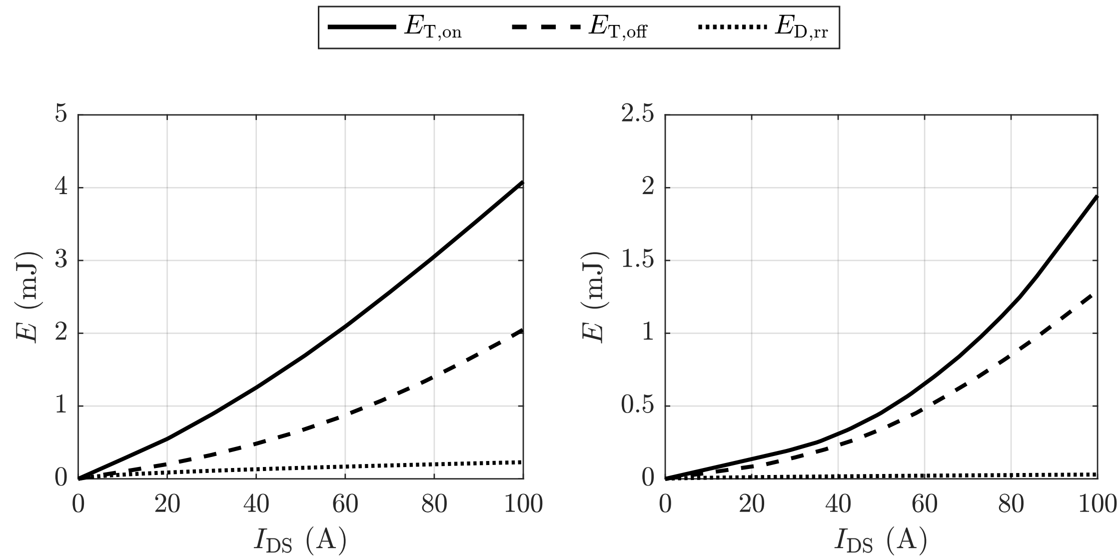

Figure 2.5: I_{DS} switching energy loss dependence for the selected IGBT co-pack (left) and SiC MOSFET (right).

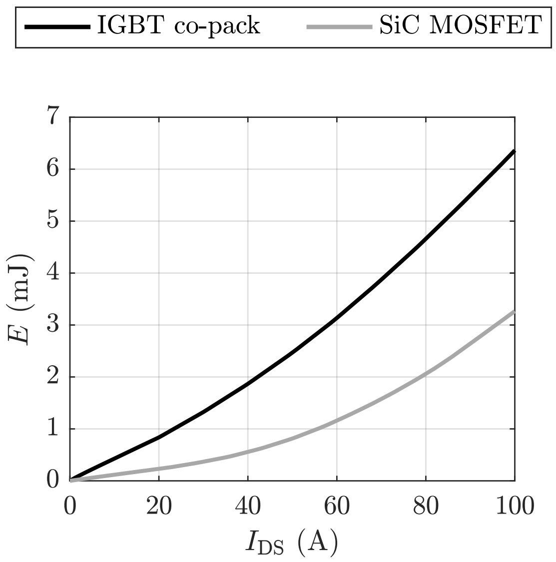

Figure 2.6: Total switching energy loss dependence on current.

2.3 Semiconductor Thermal Model

Even though this work disregards the semiconductor temperature influence in the optimization process, a thermal model of the power devices is still required to estimate the device junction temperature, which sets the upper limit to the allowable power losses. A cross-section of a TO-247 packaged device, mounted on a heatsink unit through a thermal interface material (i.e. the insulation sheet), is shown in figure 2.7. Moreover, the simplified equivalent thermal resistance network of the previous arrangement is shown in figure 2.8. This model and the subsequent calculations are based on the following assumptions:

- the heat flow is one-dimensional;
- the temperature is homogeneous over the whole interface between materials;
- there is no horizontal heat spreading outside the TO-247 package;
- there is no thermal interaction between parallel devices located next to each other.

Figure 2.8 shows the main thermal resistance difference between the IGBT co-pack and the SiC MOSFET. While the TO-247 package of the IGBT contains two semiconductor chips (i.e. one is the transistor and one is the diode), the MOSFET package contains only one chip (i.e. the die is made up by transistor and body diode). This results in two different semiconductor junction temperatures in the first case and in one unique temperature in the second:

$$\text{IGBT:} \quad \begin{cases} T_{\text{j,T}} = T_{\text{f}} + R_{\text{th,c-f}} \left(P_{\text{tot,T}} + P_{\text{tot,D}} \right) + R_{\text{th,j-c,T}}\, P_{\text{tot,T}} \\ T_{\text{j,D}} = T_{\text{f}} + R_{\text{th,c-f}} \left(P_{\text{tot,T}} + P_{\text{tot,D}} \right) + R_{\text{th,j-c,D}}\, P_{\text{tot,D}} \end{cases} \tag{2.9}$$

$$\text{MOSFET:} \quad T_{\text{j}} = T_{\text{j,T}} = T_{\text{j,D}} = T_{\text{f}} + \left(R_{\text{th,c-f}} + R_{\text{th,j-c}} \right) \left(P_{\text{tot,T}} + P_{\text{tot,D}} \right) \tag{2.10}$$

T_{f} is the cooling fluid temperature, $T_{\text{j,T}}$ and $T_{\text{j,D}}$ are the transistor and diode junction temperatures, $R_{\text{th,c-f}}$ and $R_{\text{th,j-c}}$ are the case-to-fluid and junction-to-case thermal resistances, $P_{\text{tot,T}}$ and $P_{\text{tot,D}}$ are the transistor and diode averaged total losses (i.e. sum of conduction and switching losses).

The thermal data of the two devices are summarized in table 2.1. The thermal interface area $A_{\text{th,c-f}}$ between case and heat sink has been estimated from the physical dimensions of the TO-247 package, while the thermal resistances $R_{\text{th,j-c}}$ between junction and case are provided in the manufacturer datasheet. However, the thermal resistance $R_{\text{th,c-f}}$ between case and fluid depends on the specific application, therefore it can only be calculated once a thermal interface material and a heat sink design are selected. Throughout this work, the following will be considered:

- **Thermal Interface Material:** Electrolube HTC [10]

  $\sigma_{\text{th,s}} = 18 \times 10^3\ \text{W/m}^2\text{K}$.

- **Heatsink Unit:** MeccAl LCP 180x20 [11], water-glycol 50/50 at 8 l/min

  $\sigma_{\text{th,h}} = 6 \times 10^3\ \text{W/m}^2\text{K}$.

Where $\sigma_{\text{th,s}}$ and $\sigma_{\text{th,h}}$ are the specific thermal conductances (i.e. per unit area) of the insulation sheet and the heatsink unit respectively. It is therefore possible to calculate the overall $R_{\text{th,c-f}}$ thermal resistance value:

$$R_{\text{th,c-f}} = \frac{\left(\frac{1}{\sigma_{\text{th,s}}} + \frac{1}{\sigma_{\text{th,h}}} \right)}{A_{\text{th,c-f}}} \approx 1.11\ \text{K/W} \tag{2.11}$$

It is now easy to understand why adding power devices in parallel results in a lower semiconductor junction temperature. Even without considering the benefits of

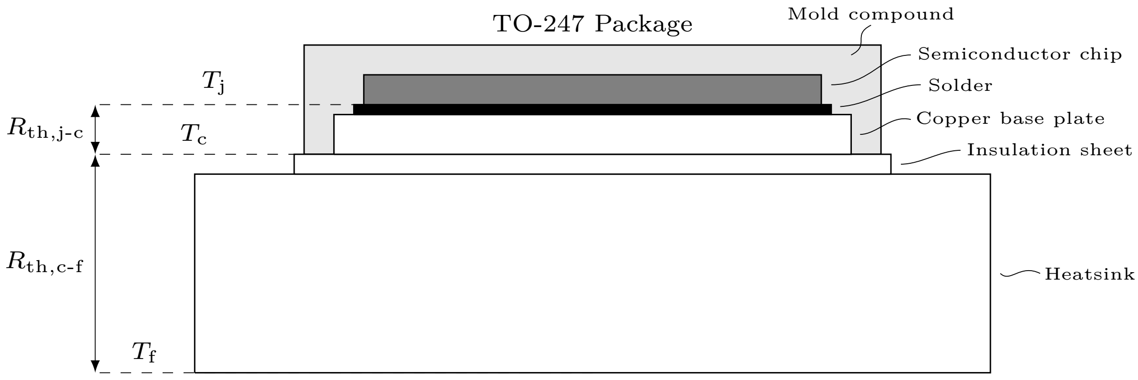

Figure 2.7: Cross-section of a generic semiconductor discrete device mounted on a heat sink with an insulation sheet in between.

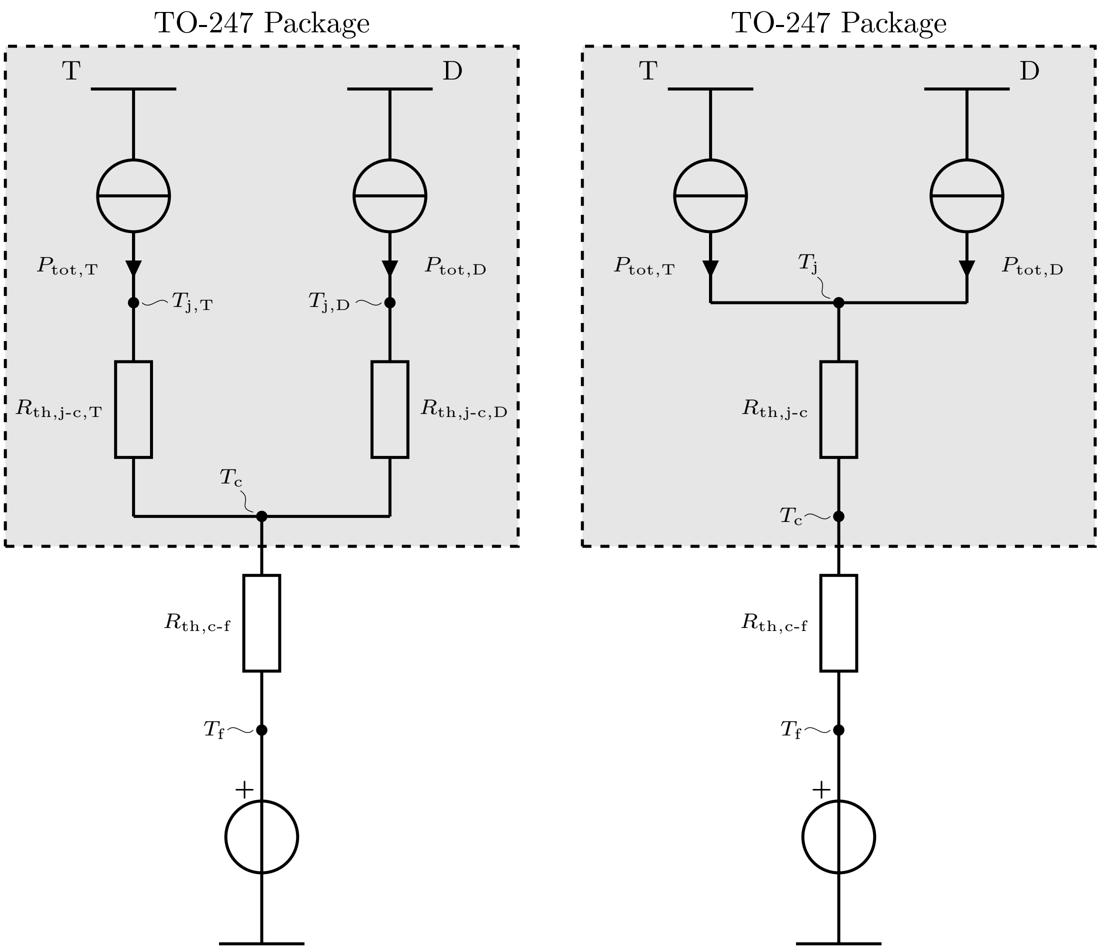

Figure 2.8: Equivalent thermal resistance network of the IGBT co-pack (left) and the SiC MOSFET (right) when mounted on a heat sink.

reduced conduction and switching losses, increasing the number of paralleled devices enlarges the total semiconductor chip area, which is inversely proportional to the overall thermal resistance.

It is worth noting that the here adopted thermal model considers the averaged power losses over the electrical fundamental period to estimate the junction temperature. However, this does not always lead to acceptable results. Since the semiconductor device thermal time constants reside in the range of $\sim 1 \times 10^{-1}$ s, it can be easily understood that power loss cycles with frequencies higher than ~ 10 Hz get "filtered". Therefore, if the electrical frequency values involved in normal operating conditions are high enough, the power loss spikes get damped by the thermal impedance network and do not proportionally translate in a temperature increase of the device. The semiconductor junction temperature thus follows the averaged power loss behaviour and the resistance network can be considered sufficient to estimate the temperature increase. However, if the inverter has been dimensioned on the averaged semiconductor losses and the electrical frequency falls below a certain threshold (i.e. ~ 10 Hz), a current derating strategy must be adopted, in order to avoid reaching even momentarily the semiconductor junction temperature limit. Since conduction losses normally represent the major part of the semiconductor losses and they roughly depend quadratically on current ($p_{\text{cond}} \approx k\, I^2$), the following relation can be adopted to derive an approximate derating strategy:

$$P_{\text{cond}} \approx k \, \frac{1}{T_1} \int_0^{T_1} I^2 \, dt \approx k \, I_{\text{RMS}}^2 \tag{2.12}$$

Where k represents the proportionality factor between the instantaneous conduction losses and the squared current, while $I_{\text{RMS}} = I/\sqrt{2}$ is the root mean square (RMS) current value. For $f \approx 0$ the semiconductor temperature rise is determined by the instantaneous power loss, as the averaging period T_1 is too long compared to the thermal time constants. Moreover, one out of three inverter legs could be continuously conducting the full phase current peak value. Therefore, equation (2.12) determines that the maximum current value I_{max} must be derated by a factor of $\sim \sqrt{2}$ to comply with the maximum junction temperature increase. This is schematically represented in figure 2.9, where T is the motor torque and n the motor speed.

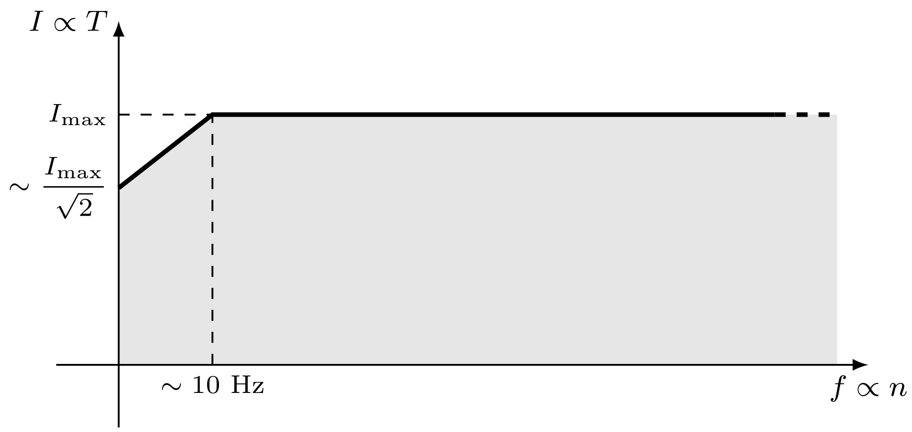

Figure 2.9: Schematic of the current derating strategy.

2.4 Modulation Techniques

Since their conception, three-phase inverters have mostly been controlled by means of Pulse Width Modulation (PWM) techniques [12]. A modulator is needed to generate the command signals to activate/deactivate the inverter switches. The generation of these signals can be obtained in two main different ways [13, 14]:

- **Carrier-Based Pulse Width Modulation** (CBPWM); the switch duty cycles are obtained from the comparison between a modulating wave and a carrier wave.
- **Space Vector Modulation** (SVM); the switch duty cycle are computed directly from the voltage space-vector concept.

It is worth mentioning that SVM has an additional degree of freedom compared to CBPWM, as it can freely choose the order of the commutating legs during the switching period, which enables possible harmonic performance gains. However, this degree of freedom is usually not exploited, since it often leads to suboptimal harmonic performance or additional switching losses [13, 14]: the "two nearest space vectors" approach is commonly adopted, as it will be explained in the following. Therefore, even though the two techniques are vastly different in how they operate, they can yield the same results. A comprehensive explanation of the relationship between CBPWM and SVM is provided in [15].

In order to compare different modulation techniques, a great amount of indices has been defined in literature. The most commonly adopted are described in the following.

The Total Harmonic Distortion (THD) of a voltage waveform without a continuous component is defined as:

$$\mathrm{THD} = \sqrt{\frac{\sum\limits_{h=2}^{\infty} {V_h}^2}{V^2}} \tag{2.13}$$

Where V and V_h are the peak amplitudes of the first and h-th order harmonics of the voltage waveform, however equation (2.13) also works with RMS values. It is worth mentioning that the THD is independent on the modulation technique for 2-level inverters, since it only depends on the amplitude of the DC-link voltage. V_{dc} affects all of the harmonic components except the fundamental one, leading to a change in the THD value. This is well explained in [3].

One quantity which depends on the modulation technique is the Weighted Total Harmonic Distortion (WTHD), defined as:

$$\mathrm{WTHD} = \sqrt{\frac{\sum\limits_{h=2}^{\infty} (V_h/h)^2}{V^2}} \tag{2.14}$$

Where h is the order of the considered harmonic. From its definition, the WTHD takes into account the order of each harmonic, attributing a higher weight to the low-frequency ones. This parameter is particularly useful when comparing the effect of different modulation techniques on the RMS value of the line current. Since most of the electrical loads are inductive, the current harmonic spectrum is equal to the voltage spectrum divided by the reactance factor $2\pi f_h L$, where f_h is the frequency of the h-th order harmonic and L the load inductance.

Even though the two aforementioned indices are commonly adopted for comparison purposes, they will not be used in this work. Since the major aim of the optimization procedure is to maximize the system efficiency, only the modulation impact on power losses is of direct interest and neither of the two introduced indices provides the desired information. In the rest of the chapter, the Harmonic Distortion Factor (HDF) index will be adopted for a performance comparison between modulation techniques:

$$\mathrm{HDF} = \sqrt{\sum_{h=2}^{\infty} (V_h/h)^2} \tag{2.15}$$

The HDF definition is simply a non-normalized version of the WTHD. This index is more useful than the previous one since it provides a general idea of the total harmonic content of the voltage waveform. Furthermore, every voltage harmonic is divided by its order, allowing a differentiation of modulation techniques based on how far is the harmonic content shifted in respect to the fundamental frequency. As will be shown in chapter 3, this index provides a qualitative behaviour of the effects of different modulation strategies on the motor time-harmonic losses.

In this work only SVM will be considered, because of its aptitude for easy digital implementation and its space-vector graphical representation, which can be directly related to the dq axis drive control. Nevertheless, the presented modulation techniques can be alternatively implemented with a CBPWM approach.

2.4.1 Space Vector Modulation

A simple circuit schematic of the 2-level inverter connected to a generic load is shown in figure 2.10. Its operation can be described by means of different combinations of

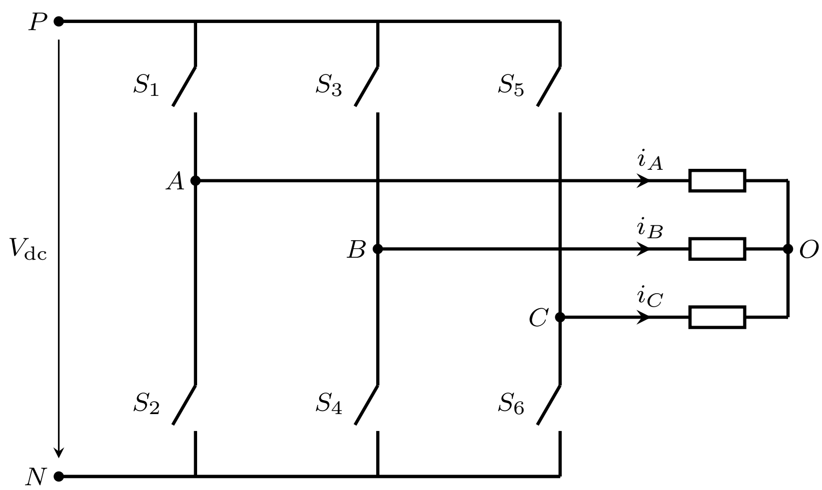

Figure 2.10: Simplified 2-level inverter circuit schematic.

the *switching states* of the three legs. Each inverter leg can only shift between two different states (from which the 2-level name):

- **P** state; the upper switch is on, while the lower switch is off. The generic phase i is connected to the upper DC-link rail and the terminal voltage v_{iN} is equal to V_{dc}.
- **N** state; the lower switch is on, while the upper switch is off. The generic phase i is connected to the lower DC-link rail and the terminal voltage v_{iN} is equal to 0.

There are only 8 available combinations of the inverter legs switching states, which are described in table 2.2. These are commonly known as *space vectors*, since they can be represented as vectors in a diagram, as shown in figure 2.11. Six of them (from $\vec{V}_1$ to $\vec{V}_6$) are called *active vectors* and the connection of their tips forms an hexagon, while the remaining two ($\vec{V}_0$ and $\vec{V}_7$) are called *zero vectors* and they lie in the center of the space vector diagram. It is worth noting that the two zero vectors graphically coincide and are therefore redundant: this redundancy is normally exploited to change the modulation behaviour, thus generating different modulation techniques. The relationship between switching states and space vectors can be derived from:

$$\vec{V}_x = \frac{2}{3}\left(v_{AN,x}\, e^{j0} + v_{BN,x}\, e^{j2\pi/3} + v_{CN,x}\, e^{j4\pi/3}\right) \tag{2.16}$$

Where x defines a space vector and the $2/3$ factor is introduced so that the space vector projections on A, B and C phase directions yield the exact phase voltages v_{AO}, v_{BO} and v_{CO}. The space vectors expressions are collected in table 2.2, while their graphical representation is shown in figure 2.11.

The reference voltage vector $\vec{V}$ rotates at the fundamental angular speed $\omega = 2\pi f$, and can be synthesized by the three nearest space vectors (2 active vectors and the zero vector). Therefore, while the reference voltage vector moves from one sector to another, the switching patterns change and different switches become involved. One complete revolution of the reference voltage vector corresponds to one fundamental period T_1.

Assuming that the sampling (or switching) period T_s is small enough compared to the fundamental period T_1, the reference voltage vector $\vec{V}$ can be considered constant during T_s. $\vec{V}$ is synthesized by the three nearest space vectors, through the *volt-second balancing* principle, which states that the product between $\vec{V}$ and T_s must be equal to the sum of the products between the chosen voltage space vectors and their dwell times. Figure 2.12 shows a highlight of the SVM operation in the first sector. Being T_a and T_b respectively the dwell times of the the first and second vectors of the sector and being T_0 the dwell time of the zero vector, the following expressions are obtained [14]:

$$\begin{cases} T_a = m\, T_s \sin\!\left(\dfrac{\pi}{3} - \theta\right) \\ T_b = m\, T_s \sin(\theta) \\ T_0 = T_s - T_a - T_b \end{cases} \tag{2.17}$$

where θ is the angle between $\vec{V}$ and the first voltage vector of the sector, while m is the modulation index:

$$m = \sqrt{3}\,\frac{V}{V_{\mathrm{dc}}} \tag{2.18}$$

Table 2.2: Space vectors definition.

Space Vector	**Switching State**	**Vector Definition**
$\vec{V}_0$	NNN	0
$\vec{V}_1$	PNN	$\frac{2}{3}\,V_{\mathrm{dc}}\,e^{j0}$
$\vec{V}_2$	PPN	$\frac{2}{3}\,V_{\mathrm{dc}}\,e^{j\pi/3}$
$\vec{V}_3$	NPN	$\frac{2}{3}\,V_{\mathrm{dc}}\,e^{j2\pi/3}$
$\vec{V}_4$	NPP	$\frac{2}{3}\,V_{\mathrm{dc}}\,e^{j\pi}$
$\vec{V}_5$	NNP	$\frac{2}{3}\,V_{\mathrm{dc}}\,e^{j4\pi/3}$
$\vec{V}_6$	PNP	$\frac{2}{3}\,V_{\mathrm{dc}}\,e^{j5\pi/3}$
$\vec{V}_7$	PPP	0

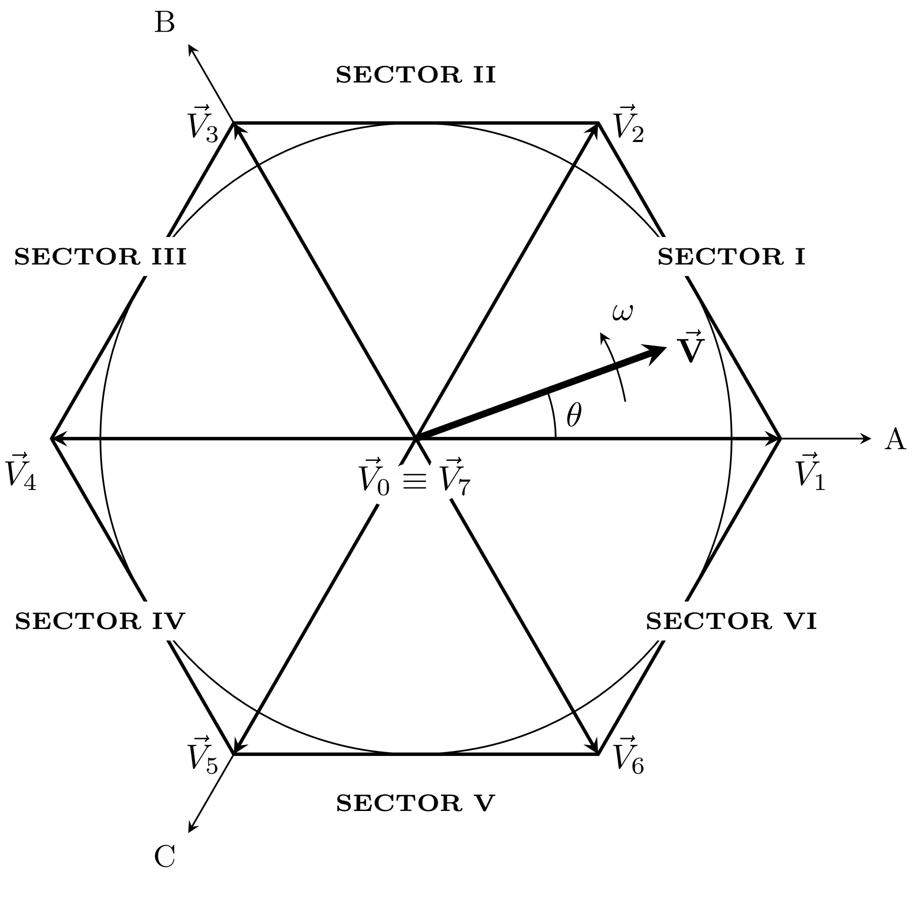

Figure 2.11: Space vector diagram of the 2-level inverter.

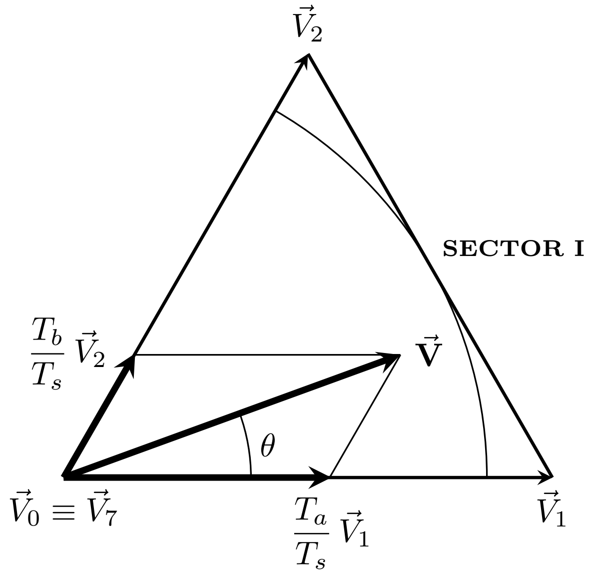

Figure 2.12: Space vector diagram: highlight of sector I.

The maximum amplitude of the obtainable phase voltage in linearity corresponds to the radius of the circle inscribed in the space vector hexagon (see figure 2.11). Being $2/3\,V_{\text{dc}}$ the length of the space vectors, from a simple geometrical relation the maximum peak amplitude of the phase voltage is obtained:

$$V_{\max} = \frac{V_{\text{dc}}}{\sqrt{3}} \tag{2.19}$$

From equations (2.18) and (2.19) it can be derived that the converter is operated in its linear modulation region when $0 \leq m \leq 1$.

SVM is characterized by one additional degree of freedom compared to CBPWM, which lies in the freedom to choose the space vector sequence during T_s. However, this choice has to comply with two major constraints:

- the transition from one space vector to another involves only one inverter leg (i.e. only one out of three switching states in changed);
- the transition of $\vec{V}$ from one sector of the space vector diagram to another must require the minimum number of switching events.

These two constraints ensure that the number of switching events during the sampling period is kept to its minimum. By doing so, the output leg duty cycle signals directly resemble the ones obtainable with a CBPWM approach, except for the fact that SVM can choose to subdivide T_0 into two separate and independent components, applying the two different redundant zero vectors. While this freedom can lead to infinite combinations and thus infinite different modulation techniques, the impact of this variation on the output voltage spectrum is very limited and doesn't yield any proven benefit. Therefore, most of the modulation techniques found in literature can be grouped into two major cathegories [13, 14]:

- **continuous modulation** techniques, also known as 7-segment SVM; T_0 is equally divided between $\vec{V}_0$ and $\vec{V}_7$;

- **discontinuous modulation** techniques, also known as 5-segment SVM; T_0 is totally attributed either to $\vec{V}_0$ or to $\vec{V}_7$, depending on the space vector diagram sector.

Both groups of techniques can be also implemented by means of a CBPWM approach, provided that the correct amount of common-mode (or zero-sequence) voltage is injected [15]. The main difference between the two cathegories lies in the trade-off between the output voltage harmonic distortion and the inverter switching losses [16]. After an extensive literature research and comparison between different modulation strategies, two of them have been selected as candidates for this work: the standard, commonly adopted, 7-segment SVM technique and an optimal adaptive-clamping 5-segment SVM technique. Both modulation strategies are described in the following.

2.4.2 Continuous Modulation (7-Segment SVM)

The conventional continuous SVM technique represents the industry standard. Table 2.3 illustrates the 7-segment switching sequence in each sector of the space vector diagram. It is important to notice that each of the 6 inverter switches turns on and off one time per sampling period T_s. The synthesized voltage waveforms v_{AN}, v_{AO} and v_{AB} are shown in figure 2.13.

Table 2.3: 7-segment SVM switching sequences.

	Switching Segment (Dwell Time)						
Sector	1 ($T_0/4$)	2 ($T_a/2$)	3 ($T_b/2$)	4 ($T_0/2$)	5 ($T_b/2$)	6 ($T_a/2$)	7 ($T_0/4$)
I	$\vec{V}_0$ NNN	$\vec{V}_1$ PNN	$\vec{V}_2$ PPN	$\vec{V}_7$ PPP	$\vec{V}_2$ PPN	$\vec{V}_1$ PNN	$\vec{V}_0$ NNN
II	$\vec{V}_0$ NNN	$\vec{V}_3$ NPN	$\vec{V}_2$ PPN	$\vec{V}_7$ PPP	$\vec{V}_2$ PPN	$\vec{V}_3$ NPN	$\vec{V}_0$ NNN
III	$\vec{V}_0$ NNN	$\vec{V}_3$ NPN	$\vec{V}_4$ NPP	$\vec{V}_7$ PPP	$\vec{V}_4$ NPP	$\vec{V}_3$ NPN	$\vec{V}_0$ NNN
IV	$\vec{V}_0$ NNN	$\vec{V}_5$ NNP	$\vec{V}_4$ NPP	$\vec{V}_7$ PPP	$\vec{V}_4$ NPP	$\vec{V}_5$ NNP	$\vec{V}_0$ NNN
V	$\vec{V}_0$ NNN	$\vec{V}_5$ NNP	$\vec{V}_6$ PNP	$\vec{V}_7$ PPP	$\vec{V}_6$ PNP	$\vec{V}_5$ NNP	$\vec{V}_0$ NNN
VI	$\vec{V}_0$ NNN	$\vec{V}_1$ PNN	$\vec{V}_6$ PNP	$\vec{V}_7$ PPP	$\vec{V}_6$ PNP	$\vec{V}_1$ PNN	$\vec{V}_0$ NNN

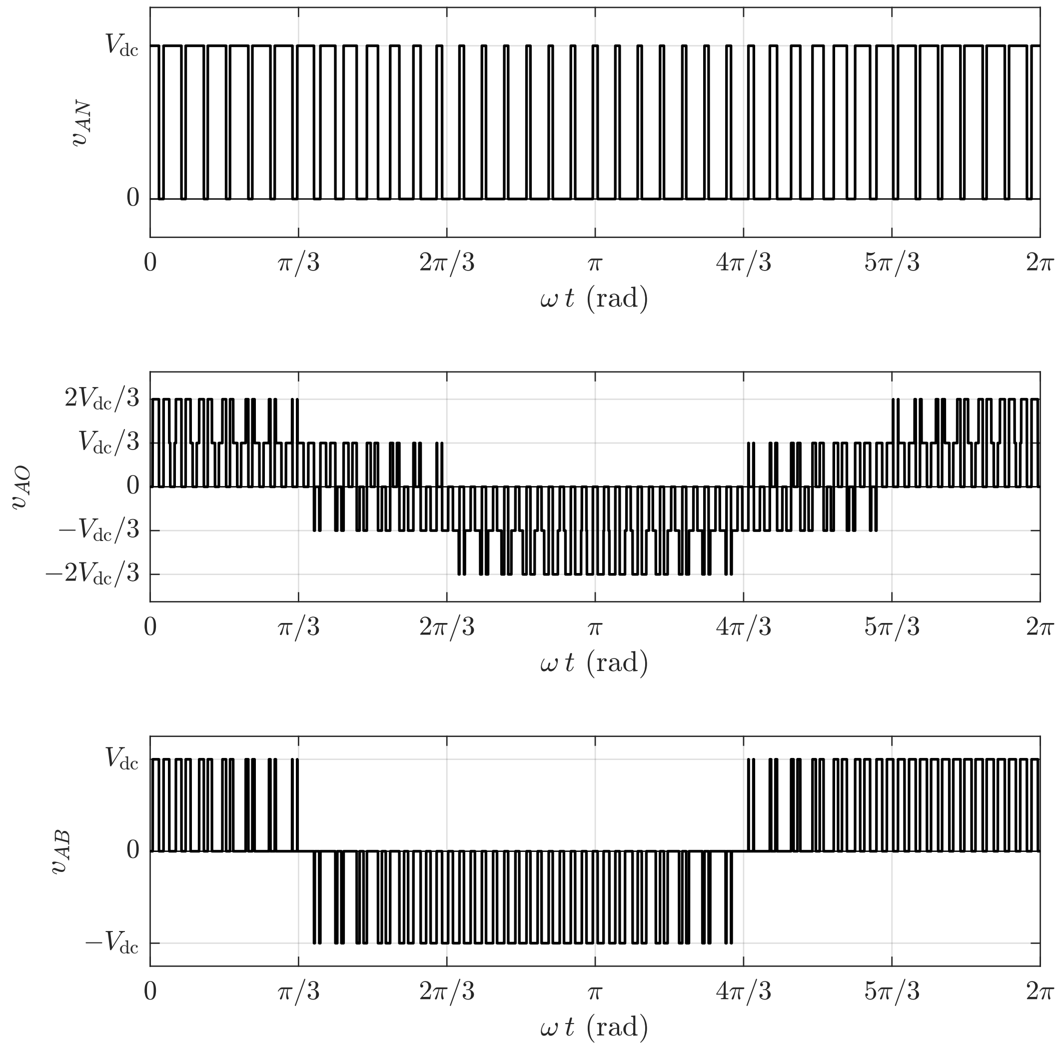

Figure 2.13: 7-segment SVM synthesized voltage waveforms with $V = 150$ V, $f = 500$ Hz, $f_{sw} = 20$ kHz. v_{AN} (top), v_{AO} (middle) and v_{AB} (bottom).

Power Losses

The instantaneous power losses generated by the semiconductor devices belonging to the first inverter leg are shown in figure 2.14, as a function of the space vector angle $\theta = \omega\, t$. The naming convention of transistors and diodes reflects the one illustrated in figure 2.1 at the beginning of the chapter.

Once a modulation technique, a semiconductor device and a certain number of devices in parallel N_{par} are fixed, the averaged inverter losses only depend on:

- **load** conditions:
  - V peak value of the phase voltage (V);
  - I peak value of the phase current (A);
  - φ power factor angle (°);

► inverter **design** parameters:

- f_{sw} switching frequency (kHz);

Therefore, the only parameter available to the designer in the optimization procedure (other than the modulation technique, the semiconductor device and N_{par}) is the switching frequency. It is worth reminding that the inverter DC-link voltage V_{dc} is considered fixed by the application (i.e. 400 V) and the loss dependence on the semiconductor junction temperature T_{j} has been neglected (i.e. temperature fixed to 150 °C).

Figure 2.15 shows the averaged inverter loss dependence on the four aforementioned variables, considering one Infineon AIKW50N65DF5 IGBT per switch and a

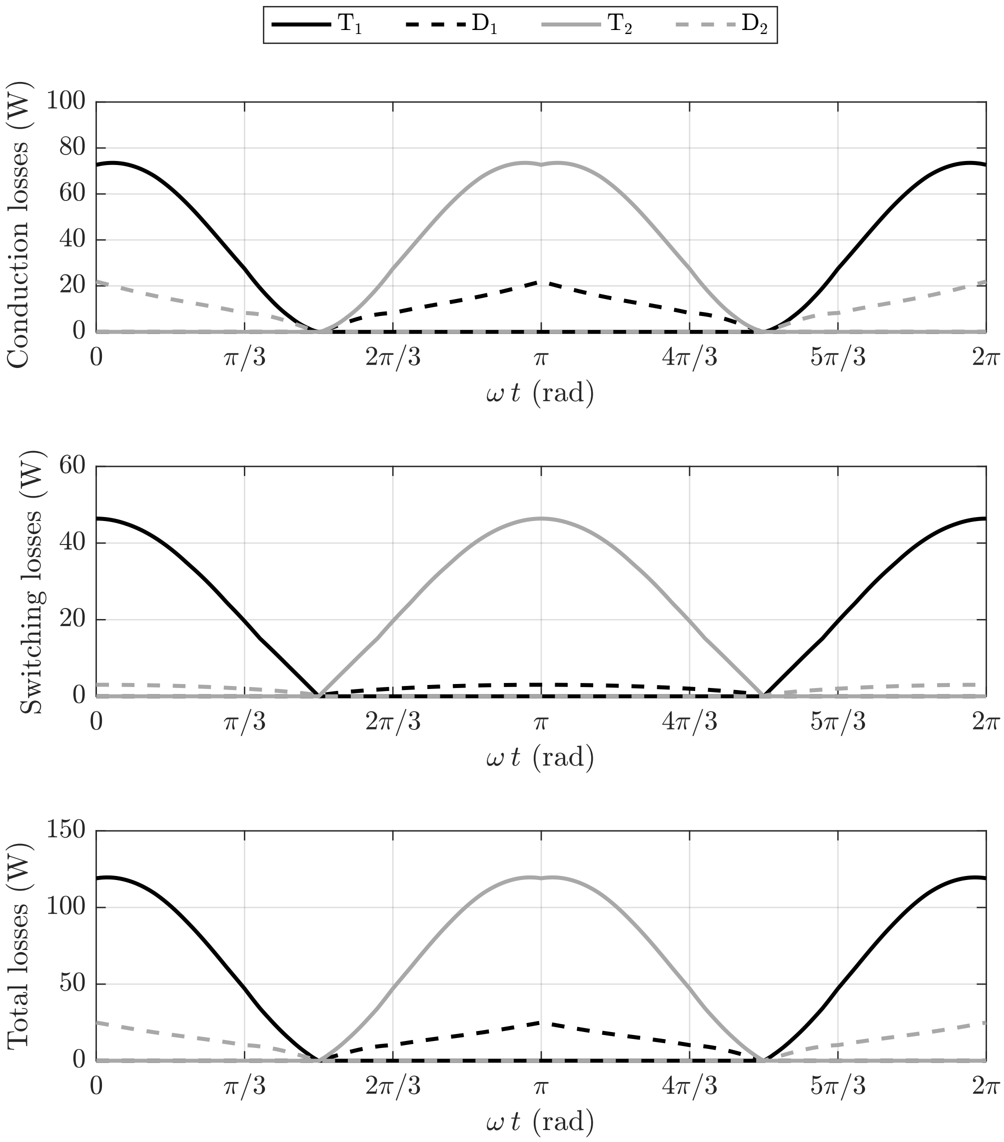

Figure 2.14: 7-segment SVM instantaneous semiconductor losses with one Infineon AIKW50N65DF5 IGBT per switch and V = 150 V, I = 50 A, φ = 0°, f_{sw} = 20 kHz. Conduction losses (top), switching losses (middle) and total losses (bottom).

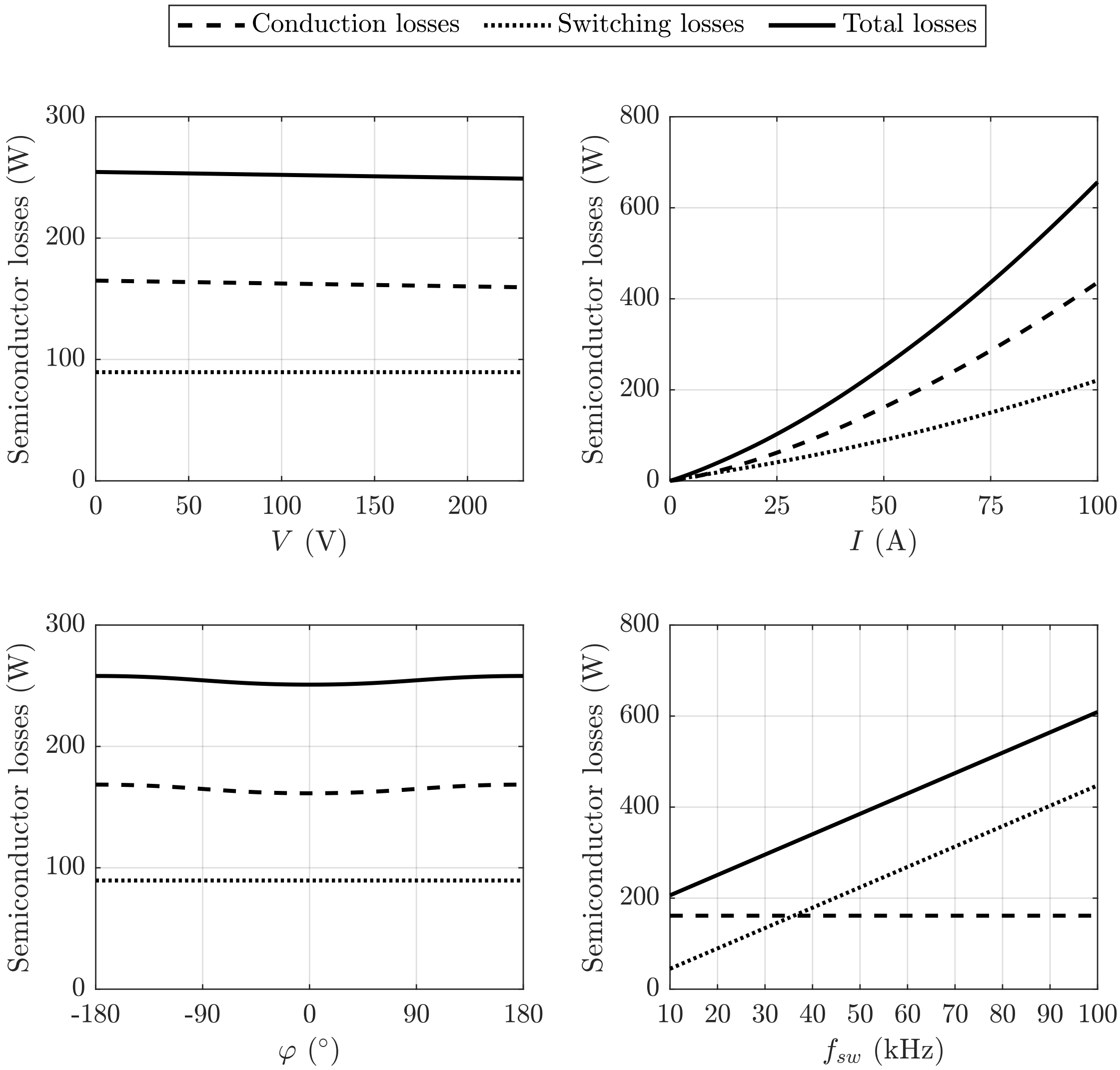

Figure 2.15: 7-segment SVM averaged semiconductor loss dependence on voltage V (top-left), current I (top-right), power factor angle φ (bottom-left) and switching frequency f_{sw} (bottom-right) with one Infineon AIKW50N65DF5 IGBT per switch and $V = 150$ V, $I = 50$ A, $\varphi = 0°$, $f_{\mathrm{sw}} = 20$ kHz.

specific operating condition (i.e. sweeping one variable at a time). The losses are subdivided in their conduction and switching components to highlight their individual behaviours. While conduction losses slightly depend on voltage (i.e. modulation index) and power factor angle, due to the moderate difference between the on-state conduction characteristics of the IGBT and its anti-parallel diode, the switching losses are totally independent on these parameters. However, both loss contributions highly depend on the load current, as shown in the previous sections (figures 2.3 and 2.6). Finally, as expected switching losses increase linearly with the switching frequency, as illustrated in equation (2.7).

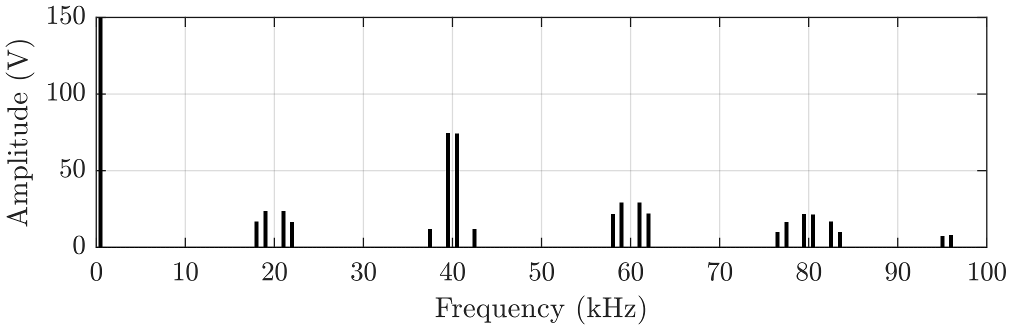

Figure 2.16: 7-segment SVM phase voltage harmonic spectrum with $V = 150$ V, $f = 500$ Hz, $f_{\text{sw}} = 20$ kHz.

Harmonic Distortion

The harmonic spectrum of the phase voltage waveforms is extracted in this work by means of Fast Fourier Transform (FFT). Although being computationally more demanding compared to analytical relations between modulation schemes and their harmonic spectra, FFT can be used to analyse any kind of waveform, without lack of generality. The phase voltage harmonic spectrum of the standard 7-segment SVM technique is shown in figure 2.16. The operating conditions are reported in the caption. The harmonic spectrum changes shape depending on:

- **load** conditions:
  - V peak value of the phase voltage (V);
- inverter **design** parameters:
  - f_{sw} switching frequency (kHz);

The exact shape of the spectrum actually depends also on the fundamental frequency f. However, the index which best allows to compare the consequences of harmonic distortion on the system losses is HDF and it does not depend on f when $f_{\text{sw}} \gg f$, which is most frequently the case. Figure 2.17 shows the HDF dependence on V and f_{sw}. While an increasing voltage amplitude leads to higher harmonic content, higher switching frequencies cause a movement of the harmonics towards higher orders, translating in a reduced HDF.

2.4.3 Discontinuous Modulation (5-Segment SVM)

Discontinuous modulation strategies eliminate one of the zero space vectors from the switching sequence, reducing the number of consecutive switching segments from 7 to 5 (from which the *5-segment SVM* name). This can be done since the two zero vectors are redundant and yield the same result in terms of volt-second balancing. Therefore, they can be used alternatively without restrictions, as long that the total T_0 time is respected. The main advantage of doing lies in eliminating one switching transition in every sample time interval, holding one inverter leg from switching (from

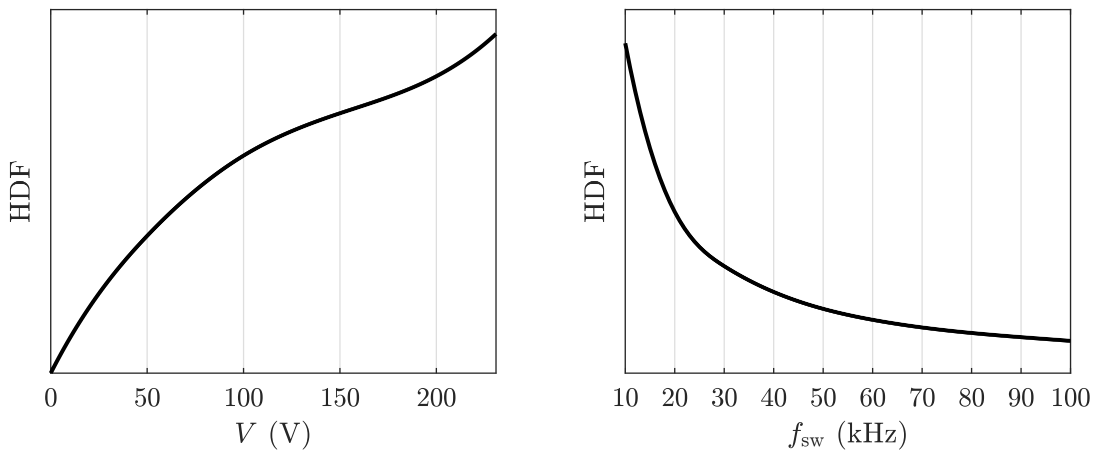

Figure 2.17: 7-segment SVM phase voltage HDF dependence on voltage V (left) and switching frequency f_{sw} (right), with $V = 150$ V, $f_{sw} = 20$ kHz.

which the *discontinuous* name). From a purely theoretical point of view, this would allow to increase the overall switching frequency by a factor of 3/2, while maintaining the same semiconductor losses. However, the harmonic performance of discontinuous modulation techniques are usually worse than the continuous counterparts. Increasing the switching frequency by 50% certainly helps, since moving the harmonics to higher frequencies reduces their influence on the HDF index, but still an overall better performance is not granted and depends on the considered system and its operating conditions. This analysis will be object of the following chapters.

Discontinuous modulation strategies suppress the modulation (i.e. the switching) of each inverter phase leg for a total of 120° per fundamental cycle, clamping the inverter output terminals to either the upper or lower DC-link rail. However, this 120° interval can be subdivided in narrower sections, where different zero space vectors, and thus clamping rails, are chosen. This freedom allows to create many different modulation strategies. The most frequently reported in literature belong to the 120°, 60° and 30° categories, which inherit their name from the width of the implemented clamping intervals [12, 13, 15–18]. While both 60° and 30° clamping strategies equally distribute the switching and conduction losses between the high-side and low-side switches, since they alternatively clamp each phase to the upper and lower DC-link rail, 120° clamping techniques do not, therefore they are not commonly adopted.

The only difference between modulation strategies inside the 60° and 30° categories is the angle around which the clamping interval is centered. This angle is usually chosen equal to the power factor angle φ, since, by doing so, each inverter phase clamping interval is centered around the peak of the respective phase current, avoiding to switch during the highest loss operating condition. This is illustrated in figures 2.18 and 2.19, where the modulation technique adapts its clamping angle to follow φ. It is important to notice that positioning the clamping angle around the power factor angle grants a higher than 1/3 reduction in the switching losses, practically enabling a greater than 50% increase in switching frequency. However, the clamping angle cannot

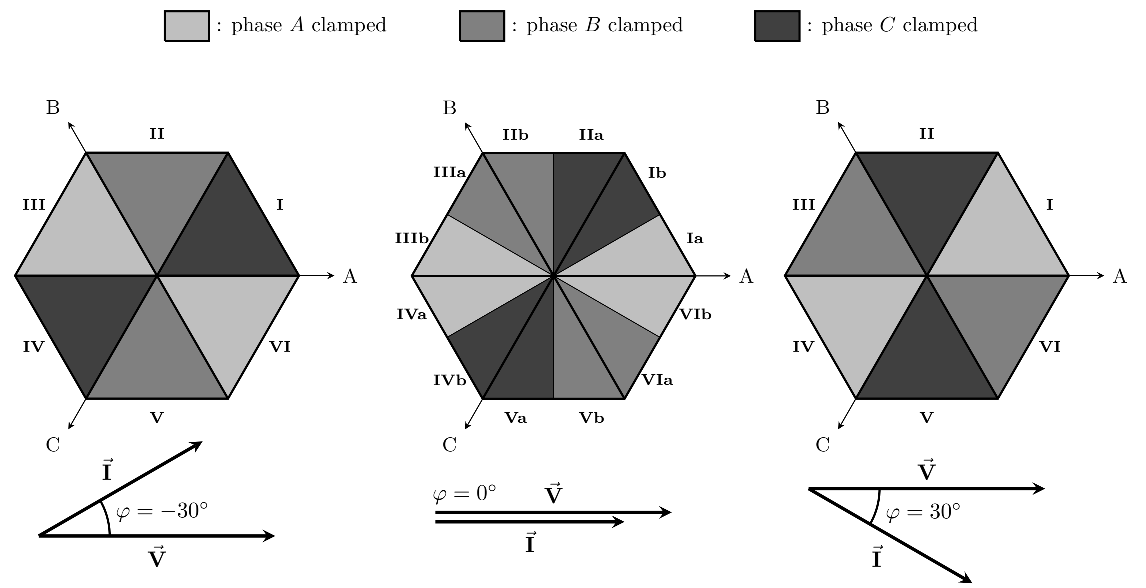

Figure 2.18: Space vector diagrams of the adopted 5-segment SVM, highlighting the clamped phase in each sector. Three different operating conditions are considered: $\varphi = -30°$ (left), $\varphi = 0°$ (middle) and $\varphi = +30°$ (right).

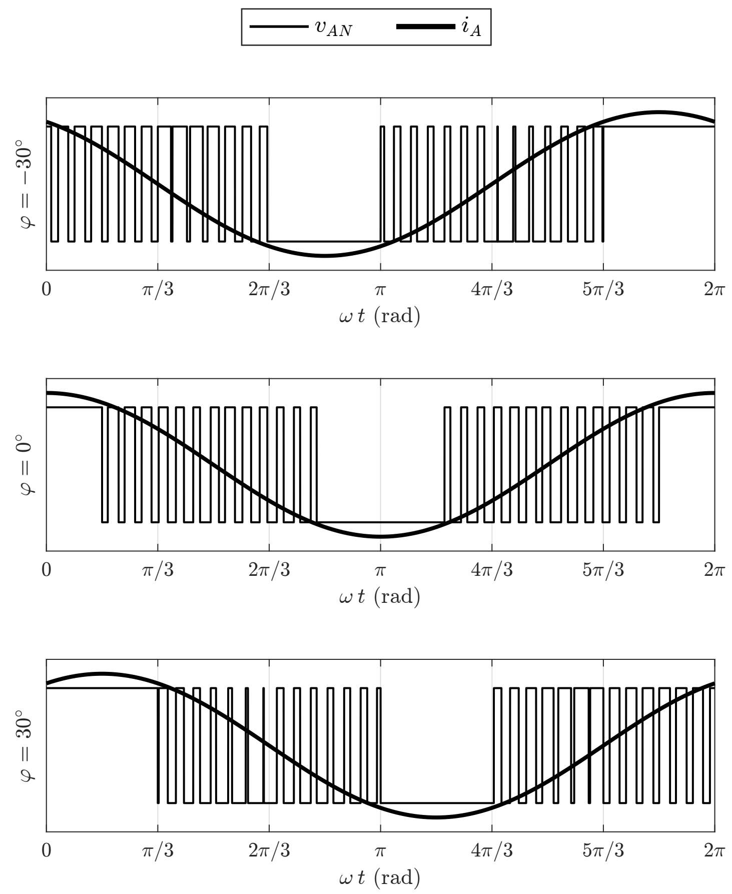

Figure 2.19: 5-segment SVM v_{AN} and i_a waveforms in three different operating conditions: $\varphi = -30°$ (top), $\varphi = 0°$ (middle) and $\varphi = +30°$ (bottom).

follow φ outside of a $\pm 30°$ range and, while alternative strategies can be adopted to mitigate this problem (see [17, 18]), the present work sets the clamping angle to $\pm 30°$ when φ falls outside the respective limit. It is worth mentioning that the $\pm 30°$ clamping range in the motoring direction ($P > 0$) also provides a symmetrical clamping range in the generating direction ($P < 0$), being $150° \leq \varphi \leq 210°$.

While industrial inverters normally work with certain predetermined load conditions, thus a single value of the clamping interval centering angle can be chosen a priori, automotive traction works in an unlimited number of very different operating points and no optimal angle can be chosen preventively. Therefore, the here considered adaptive optimal-clamping discontinuous strategy varies the clamping angle with continuity during operation, ensuring that the optimal modulation strategy is adopted

Table 2.4: 5-segment SVM switching sequences.

	Switching Segment (Dwell Time)									
	Sequence 1					**Sequence 2**				
Sector	1 ($T_0/2$)	2 ($T_b/2$)	3 (T_a)	4 ($T_b/2$)	5 ($T_0/2$)	1 ($T_0/2$)	2 ($T_a/2$)	3 (T_b)	4 ($T_a/2$)	5 ($T_0/2$)
I a	$\vec{V}_7$ PPP	$\vec{V}_2$ PPN	$\vec{V}_1$ PNN	$\vec{V}_2$ PPN	$\vec{V}_7$ PPP	-	-	-	-	-
I b	-	-	-	-	-	$\vec{V}_0$ NNN	$\vec{V}_1$ PNN	$\vec{V}_2$ PPN	$\vec{V}_1$ PNN	$\vec{V}_0$ NNN
II a	-	-	-	-	-	$\vec{V}_0$ NNN	$\vec{V}_3$ NPN	$\vec{V}_2$ PPN	$\vec{V}_3$ NPN	$\vec{V}_0$ NNN
II b	$\vec{V}_7$ PPP	$\vec{V}_2$ PPN	$\vec{V}_3$ NPN	$\vec{V}_2$ PPN	$\vec{V}_7$ PPP	-	-	-	-	-
III a	$\vec{V}_7$ PPP	$\vec{V}_4$ NPP	$\vec{V}_3$ NPN	$\vec{V}_4$ NPP	$\vec{V}_7$ PPP	-	-	-	-	-
III b	-	-	-	-	-	$\vec{V}_0$ NNN	$\vec{V}_3$ NPN	$\vec{V}_4$ NPP	$\vec{V}_3$ NPN	$\vec{V}_0$ NNN
IV a	-	-	-	-	-	$\vec{V}_0$ NNN	$\vec{V}_5$ NNP	$\vec{V}_4$ NPP	$\vec{V}_5$ NNP	$\vec{V}_0$ NNN
IV b	$\vec{V}_7$ PPP	$\vec{V}_4$ NPP	$\vec{V}_5$ NNP	$\vec{V}_4$ NPP	$\vec{V}_7$ PPP	-	-	-	-	-
V a	$\vec{V}_7$ PPP	$\vec{V}_6$ PNP	$\vec{V}_5$ NNP	$\vec{V}_6$ PNP	$\vec{V}_7$ PPP	-	-	-	-	-
V b	-	-	-	-	-	$\vec{V}_0$ NNN	$\vec{V}_5$ NNP	$\vec{V}_6$ PNP	$\vec{V}_5$ NNP	$\vec{V}_0$ NNN
VI a	-	-	-	-	-	$\vec{V}_0$ NNN	$\vec{V}_1$ PNN	$\vec{V}_6$ PNP	$\vec{V}_1$ PNN	$\vec{V}_0$ NNN
VI b	$\vec{V}_7$ PPP	$\vec{V}_6$ PNP	$\vec{V}_1$ PNN	$\vec{V}_6$ PNP	$\vec{V}_7$ PPP	-	-	-	-	-

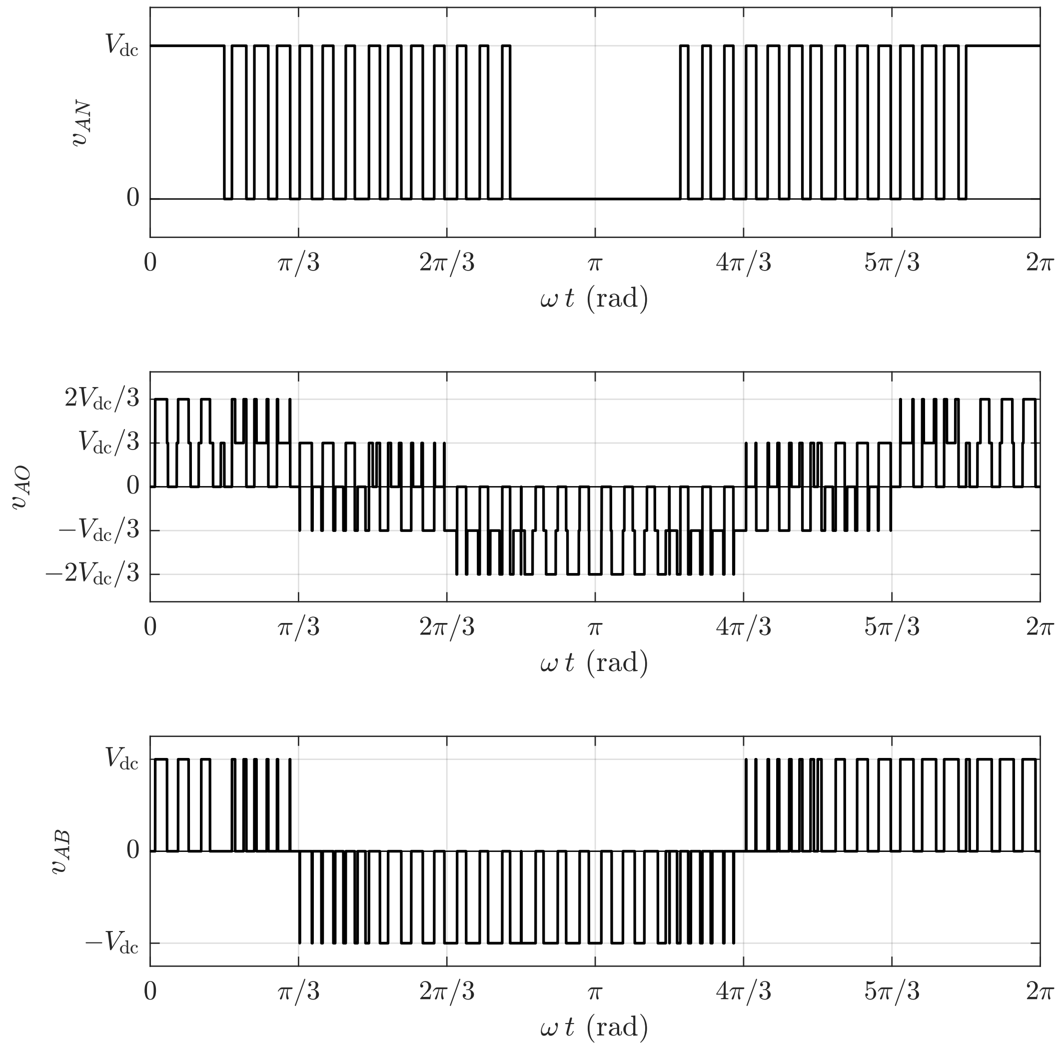

Figure 2.20: 5-segment SVM synthesized voltage waveforms with V = 150 V, $\varphi = 0$ °, f = 500 Hz, f_{sw} = 20 kHz. v_{AN} (top), v_{AO} (middle) and v_{AB} (bottom).

inside a $-30°\leq \varphi \leq +30°$ range, in order to minimize switching losses. While this interval seems quite narrow, the traction motor chosen for this work mostly operates in the mentioned power factor angle range.

Figure 2.18 shows the space vector diagrams in three different phase clamping angle situations, with power factor angle φ values of $-30°$ (*leading*), 0° and +30° (*lagging*) from left to right: the clamped phase in each sector or sub-sector is highlighted. Moreover, figure 2.19 displays the inverter output terminal voltage v_{AN} waveforms together with the phase current i_a. The phase clamping interval is particularly visible, since the output voltage waveform stays constant during a 60° interval centered around the phase current peak.

For clarity reasons, the rest of the section will consider a unity power factor (i.e. $\varphi = 0°$), in order to uniformly compare the waveforms, losses and harmonic distortion with the previously presented 7-segment SVM strategy.

Table 2.4 shows the two different switching sequences of the 5-segment SVM with

$\varphi = 0°$. The two sequences are adopted in different space vector sub-sectors, in order to clamp the wanted phase with a 60° continuity. Since different zero vectors are adopted in each sub-sector, the active vector order must change to ensure only one switching event per space vector transition. This yields an order swap of T_a and T_b dwell times between the two switching sequences. The synthesized voltage waveforms v_{AN}, v_{AO} and v_{AB} are shown in figure 2.20.

Power Losses

Figure 2.21 shows the instantaneous power losses of the semiconductor devices belonging to phase A inverter leg, as a function of the space vector angle $\theta = \omega\, t$. While

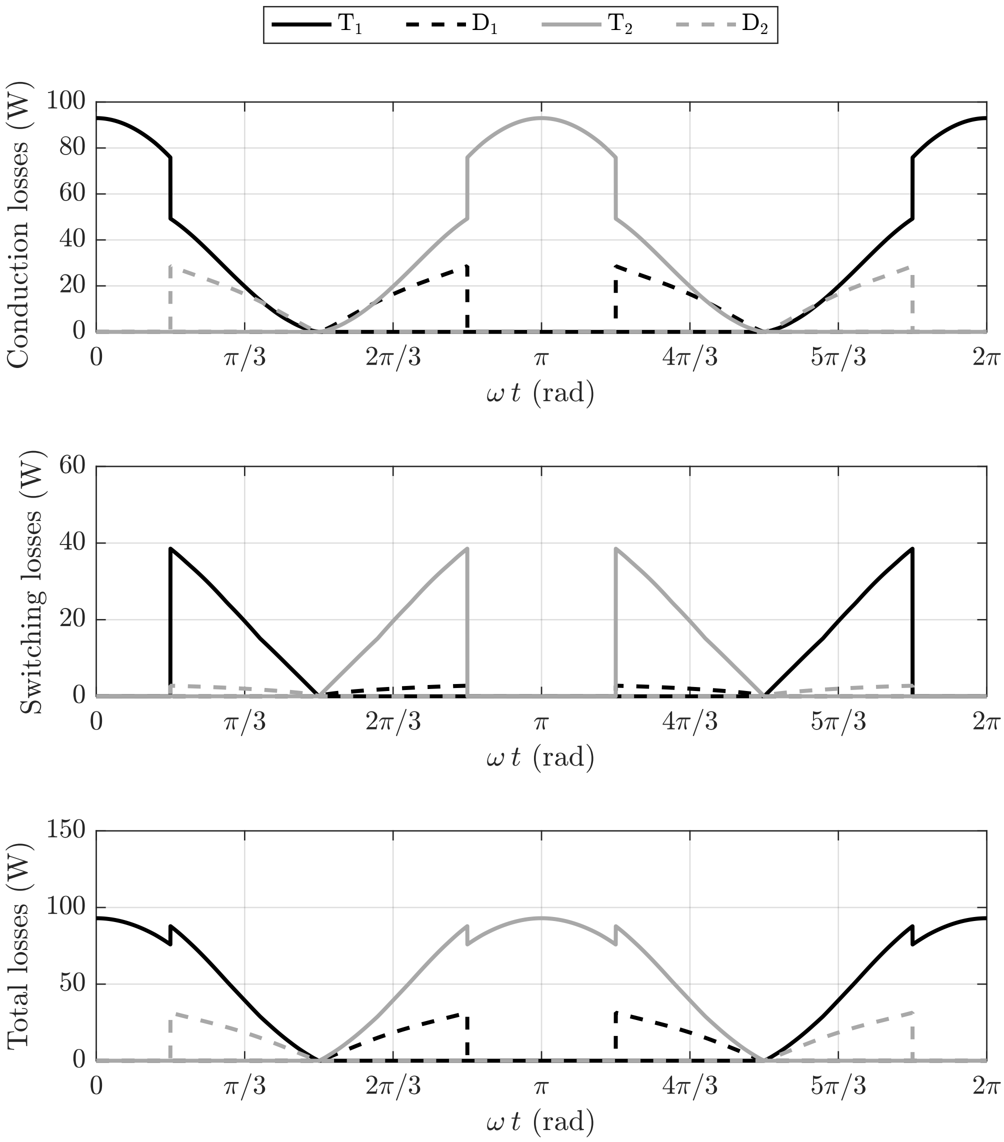

Figure 2.21: 5-segment SVM instantaneous semiconductor losses with one Infineon AIKW50N65DF5 IGBT per switch and V = 150 V, I = 50 A, $\varphi = 0°$, f_{sw} = 20 kHz. Conduction losses (top), switching losses (middle) and total losses (bottom).

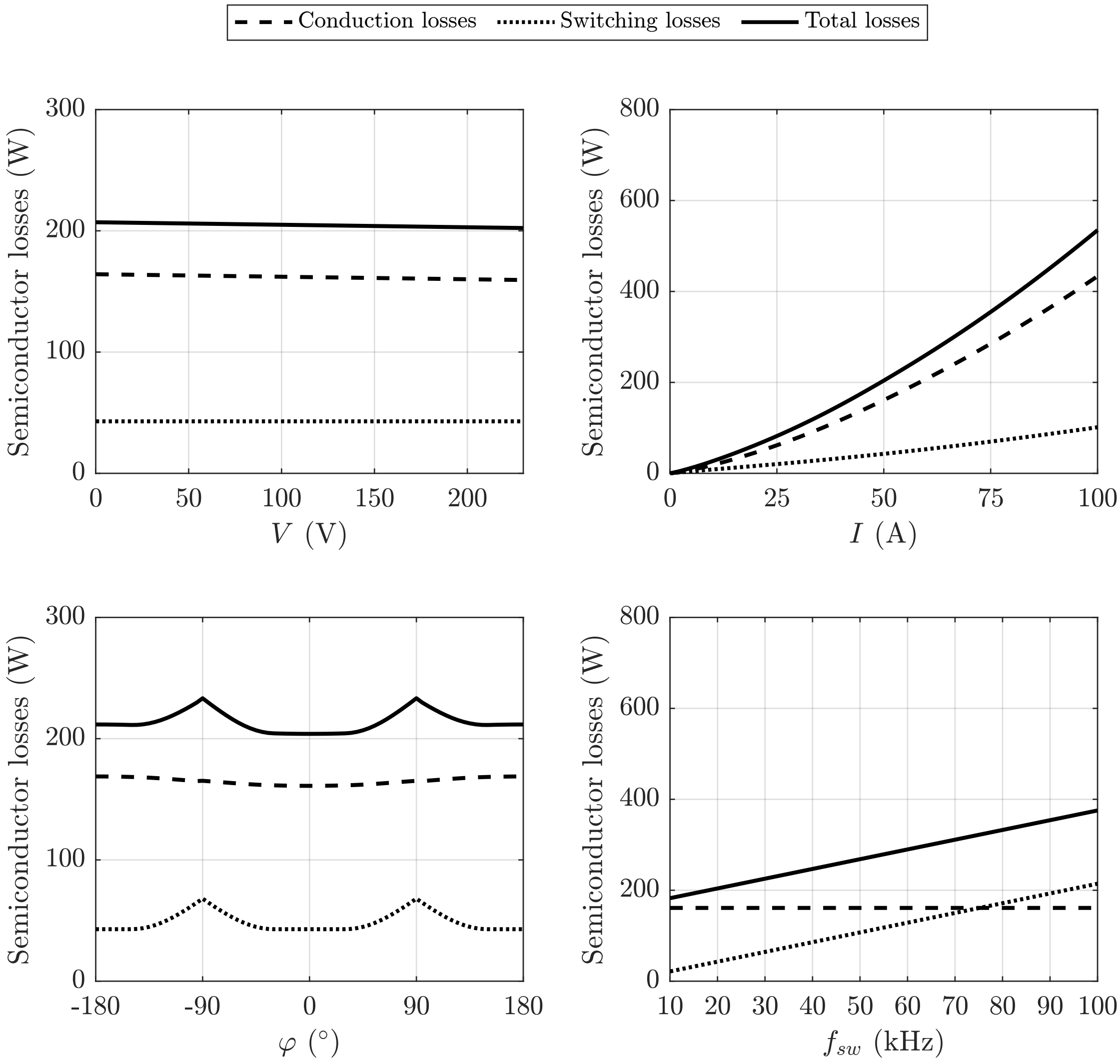

Figure 2.22: 5-segment SVM averaged semiconductor loss dependence on voltage V, current I, power factor angle φ and switching frequency f_{sw} with one Infineon AIKW50N65DF5 IGBT per switch and $V = 150$ V, $I = 50$ A, $\varphi = 0°$, $f_{\mathrm{sw}} = 20$ kHz.

conduction losses remain mostly unchanged from the previous modulation strategy (except for the different subdivision between IGBT and its anti-parallel diode), the absence of switching losses during the two 60° intervals is evident.

The inverter loss dependence on the previously identified four main parameters V, I, φ and f_{sw} is illustrated in figure 2.22. The main difference compared to the 7-segment SVM is the semiconductor loss variation with the power factor angle φ. Both conduction and switching losses do not depend on φ in the $\pm 30°$ range, since the modulation scheme follows the current waveform. However, outside of this range losses start increasing, as the phase clamping is no longer centered on the current peak. As previously mentioned, the present application will not often work outside of the $\pm 30°$ range, thus the semiconductor loss dependence on φ can be neglected for both 5-segment and 7-segment SVM strategies.

It is important to notice that, while averaged conduction losses remain practically unaltered compared to the 7-segment modulation technique (see figure 2.15), switching losses decrease by a factor of 2 when $-30° \leq \varphi \leq +30°$. This is because the IGBT switching losses show a roughly linear dependence on current (see figure 2.6), therefore the averaged losses over the fundamental period can be expressed by:

$$P_{\mathrm{sw},(7)} \approx \frac{1}{\pi}\, k\, I \int_{-\pi/2}^{\pi/2} \cos\theta\, d\theta = \frac{2}{\pi}\, k\, I \tag{2.20}$$

$$P_{\mathrm{sw},(5)} \approx \frac{1}{\pi}\, k\, I \left(\int_{-\pi/2}^{-\pi/6} \cos\theta\, d\theta + \int_{\pi/6}^{\pi/2} \cos\theta\, d\theta \right) = \frac{1}{\pi}\, k\, I \tag{2.21}$$

Where $P_{\mathrm{sw},(7)}$ and $P_{\mathrm{sw},(5)}$ are the averaged switching losses for the 7-segment and 5-segment SVM respectively, while k represents the proportionality coefficient between current and switching losses. It is therefore evident that a factor of ~ 2 exists between the switching losses generated by the two different modulation techniques. Since SiC MOSFET has a more pronounced switching loss dependence on current than the IGBT, the loss reduction benefit will be even higher in this case.

Harmonic Distortion

Figure 2.23 illustrates the phase voltage harmonic spectrum of the implemented 5-segment SVM technique. The shown spectrum relates to the $\varphi = 0°$ modulation case and the operating conditions are reported in the caption. The actual shape of the spectrum depends on where the clamping interval is situated (and thus on φ), but the HDF is mostly independent on it, therefore the harmonic dependence on the power factor angle will be neglected in the following.

Figure 2.24 depicts the HDF dependence on V and f_{sw}. A shape difference compared to the 7-segment SVM can be noticed in the voltage dependence: the HDF is not monotonically increasing and thus shows a peak.

Figure 2.25 shows a comparison between the HDF values of the selected continuous and discontinuous modulation techniques, where the 5-segment SVM switching frequency has been adjusted to generate the same switching loss amount as the 7-segment SVM (i.e. $2f_{\mathrm{sw}}$). The discontinuous modulation strategy shows a considerable HDF advantage towards high modulation index levels (i.e. high V), while having a

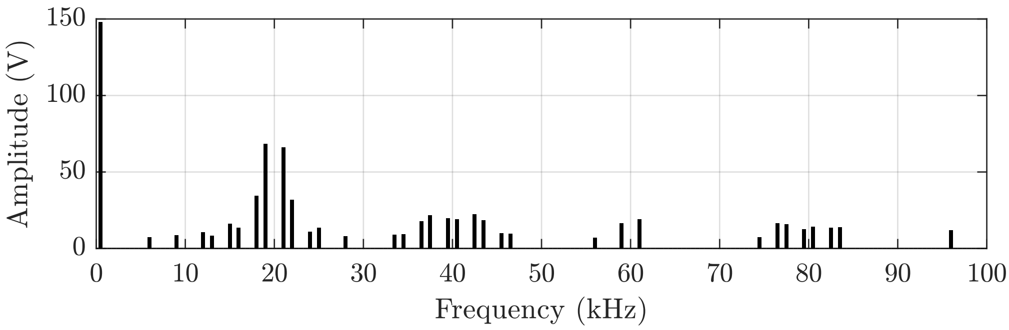

Figure 2.23: 5-segment SVM phase voltage harmonic spectrum with $V = 150$ V, $f = 500$ Hz, $f_{\mathrm{sw}} = 20$ kHz.

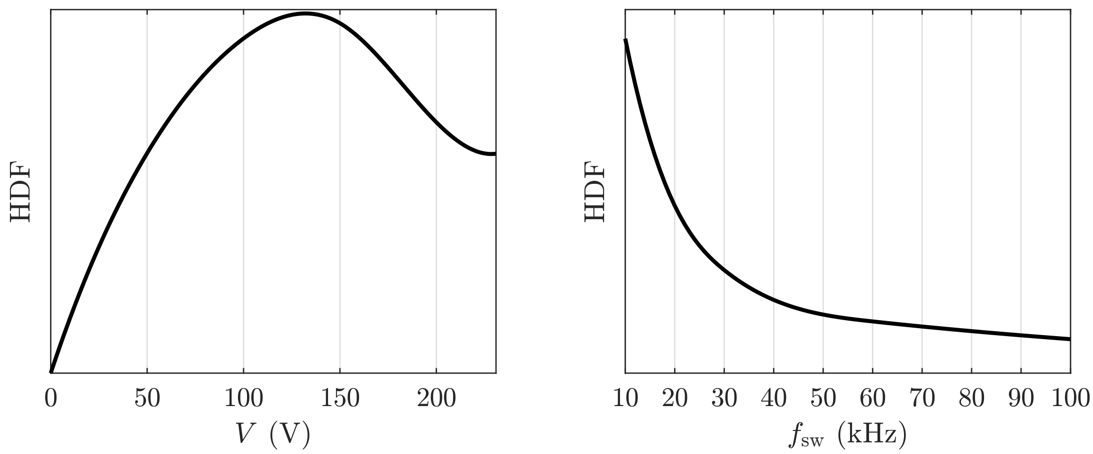

Figure 2.24: 5-segment SVM phase voltage HDF dependence on voltage V (left) and switching frequency f_{sw} (right), with $V = 150$ V, $f_{\mathrm{sw}} = 20$ kHz.

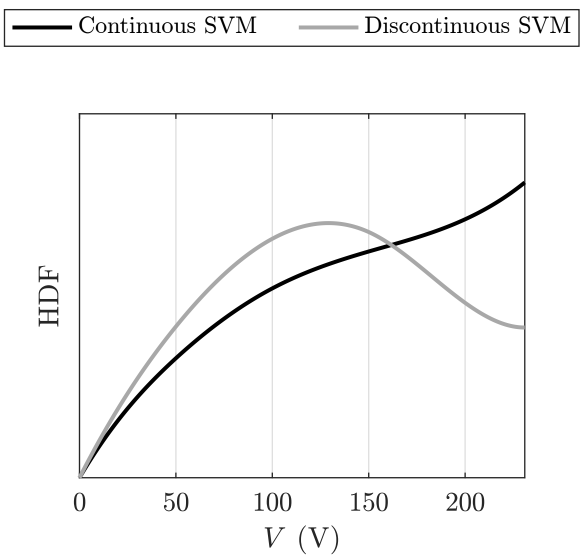

Figure 2.25: 7-segment and 5-segment SVM phase voltage HDF comparison as a function of voltage V with $f_{sw} = 20$ kHz. 5-segment SVM switching frequency adjusted to $2\,f_{sw}$.

slightly worse behaviour than the 7-segment SVM around mid and low voltage values. Therefore, an absolute best modulation strategy cannot be identified.

As already pointed out, choosing between a continuous and a discontinuous modulation strategies is not straightforward. The trade-off between lower switching losses and higher harmonic distortion must be carefully analysed in every operating condition, since semiconductor losses mostly depend on I and f_{sw}, while harmonic distortion depends on V and f_{sw}. However, both terms change with switching frequency. This variable is available to the inverter designer and should be chosen to optimize the system efficiency. In order to find the overall loss minimum, a reliable motor model which interlinks the output voltage spectrum of the converter with the additional inverter-induced motor losses should be available. This is one of the goals of chapter 3.

Chapter 3

Motor Model

Electric vehicle drive trains currently on the market strongly differ one from another for the adopted electrical machine type. A common technology direction has yet to be seen. This is due to the fact that each motor solution shows individual advantages and drawbacks, which can prevail depending on the specific application. Therefore, an absolute optimal design does not exist. However, some machine types have already established themselves as the most appropriate solutions for automotive traction:

- **induction motors (IM)** are mainly adopted for their simplicity (both from the design and the control point of view) and low cost, leveraging a century-long industrial development;

- **permanent magnet synchronous motors (PMSM)** offer some interesting advantages compared to IMs, such as higher efficiency and torque density. However, the high cost of rare-earth magnet materials (i.e. NdFeB, SaCo) and the safety concern regarding uncontrolled generator operation (UGO) can represent an issue in automotive.

It is worth mentioning that a big distinction exists throughout PMSMs, as they are normally categorized by the physical position of the magnets in the rotor. Surface-mount permanent magnet (SPM) and interior permanent magnet (IPM) synchronous machines are therefore distinguished.

SPM machines for traction application are normally designed with concentrated stator coils, which, compared to distributed windings, enhance flux weakening capabilities, decrease winding resistance (shorter end connections) and reduce the manufacturing complexity. However, SPM motors suffer from high eddy current losses in the permanent magnets, because of their physical position (i.e. facing the air gap) combined with the high flux harmonic content introduced by the stator coils. The sintered permanent magnets also need mechanical retention, in order to not detach from the rotor surface when subject to strong centrifugal forces at high speeds.

IPM machines, instead, need a lower amount of permanent magnet material if the rotor is suitably realized with a high saliency structure. This can be achieved by multiple flux-barrier designs, leading to a so-called permanent magnet assisted synchronous reluctance (PMASR) machine. Its name derives from its peculiar rotor structure, which resembles a transverse-laminated synchronous reluctance (SyR) machine with embedded permanent magnets. The magnets "assist" the machine operation, since their contribution to the total flux is normally lower than the one generated by the stator currents. In general, a high level of saliency yields many benefits, such as cost reduction (less permanent magnet material), wider constant power speed range (CPSR), higher overload capability, lower back electromotive force (EMF) during UGO and lower sensitivity to permanent magnet temperature variation. Moreover, the inherent anisotropy of IPMs can be leveraged to implement sensorless control strategies at low speed values, by means of signal superimposition [19].

Overall, the best solution is usually application-dependent and definitely not straightforward. A thorough comparison between electrical machine types for automotive traction application is not object of this dissertation and is provided in [20, 21].

Since the traction motor represents the major loss component of the traction line, an analysis of its loss mechanisms is of utmost importance. This chapter describes the construction and implementation of the motor loss model, while detailing the main simulations and measurements required for the task.

3.1 PMASR Machine

Automotive traction applications normally require the best combination between:

- high torque density;
- high efficiency;
- high overload capabilities;
- wide CPSR;
- low back EMF in UGO;
- low cost.

High torque density and efficiency normally translate in the adoption of permanent magnets. High overload capabilities and wide CPSR are strictly linked and both require a good flux-weakening capability. Finally, low back EMF in UGO and low cost both imply the lowest possible magnet material quantity. The IPM machine category represents a valid candidate to face this challenges. However, an optimal trade-off between the listed performance indices can be only achieved by means of a careful and precise design process. This is thoroughly analysed and described in [22], where the best designs for automotive application are shown to head towards the PMASR machine type. The schematic cross-section of a generic 4-pole PMASR machine with 3 flux barriers is shown in figure 3.1. Throughout this dissertation, the PMSM convention of aligning the d-axis with the permanent magnet flux will be adopted. Therefore, as illustrated in figure, the d-axis is aligned to the direction of maximum reluctance, while the q-axis indicates the path of maximum permeance.

As previously mentioned, the main differences between the PMASR motor and a conventional IPM machine reside in the amount of rotor saliency and quantity of

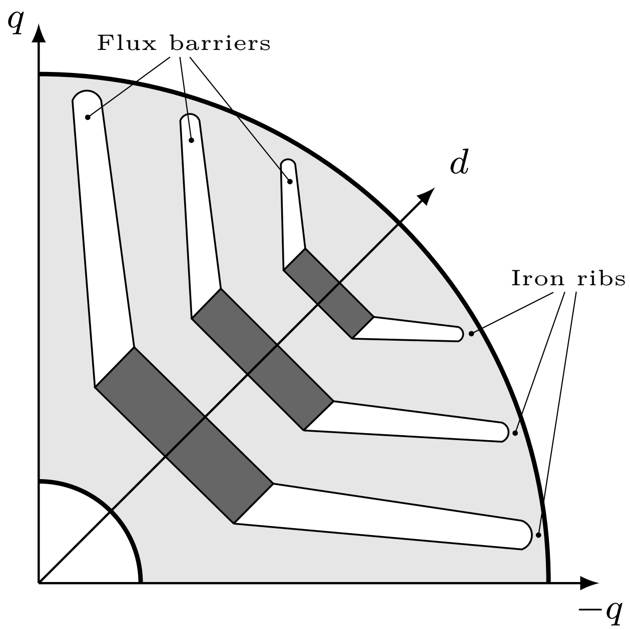

Figure 3.1: Schematic of a PMASR machine pole. The adopted dq reference frame convention is highlighted.

permanent magnets. By increasing the rotor anisotropy, the amount of rare-earth magnet material can be decreased, while maintaining the same torque performance. Moreover, the machine flux-weakening capability and its power factor value can both be enhanced by a suitable design of the total magnet flux.

The motor magnetic model can be expressed by the following vector equation:

$$\vec{\lambda}_{dq} = \vec{L}_{dq} \cdot \vec{i}_{dq} + \vec{\lambda}_{\mathrm{pm}} \tag{3.1}$$

Where $\vec{\lambda}_{dq}$ is the flux linkage vector, $\vec{\lambda}_{\mathrm{pm}}$ the permanent magnet flux vector, $\vec{i}_{dq}$ the current vector and $\vec{L}_{dq}$ the inductance matrix:

$$\vec{L}_{dq} = \begin{bmatrix} L_d & 0 \\ 0 & L_q \end{bmatrix} \tag{3.2}$$

The vector equation can be thus represented by means of two scalar equations in the d and q axis respectively:

$$\begin{cases} \lambda_d = L_d \, i_d + \lambda_{\mathrm{pm}} \\ \\ \lambda_q = L_q \, i_q \end{cases} \tag{3.3}$$

It is important to note that the flux dependence on current is not straightforward. First, L_d and L_q depend on both i_d and i_q. This is due to a relevant cross-coupling saturation effect, which characterizes those machines with high levels of anisotropy. Second, these dependences are highly non-linear, due to the iron behaviour for high flux-density values. λ_d and λ_q are normally directly extracted as a function of i_d and

i_q, thus a better way to express the magnetic equations is:

$$\begin{cases} \lambda_d = \lambda_d\left(i_d, i_q\right) \\ \lambda_q = \lambda_q\left(i_d, i_q\right) \end{cases} \tag{3.4}$$

While being challenging to extract, the magnetic model is extremely important if an accurate control of the motor is required. The magnetic model extraction is the subject of the next section.

Figure 3.2 shows the vector representation of an infinite CPSR design, where $\vec{\lambda}_{\text{pm}}$ has been chosen to exactly compensate the current-generated flux at infinite speed. Dotted lines represent the flux-weakening action of both $\vec{i}_{dq}$ (circle) and $\vec{\lambda}_{dq}$ (ellipse). It is worth noting that at high speed, while $\vec{i}_{dq}$ approaches the d-axis, $\vec{\lambda}_{dq}$ tends to the q-axis direction. The angle between the two vectors increases towards 90°, thus continuing to generate torque and improving the motor power factor.

The electrical model is common to all motor types and can be represented by the following vector equation:

$$\vec{v}_{dq} = R_{\text{s}}\,\vec{i}_{dq} + \frac{d\vec{\lambda}_{dq}}{dt} + j\,\omega\,\vec{\lambda}_{dq} \tag{3.5}$$

The projections of the vector equation on the d and q axis yield:

$$\begin{cases} v_d = R_{\text{s}}\,i_d + \dfrac{d\lambda_d}{dt} - j\,\omega\,\lambda_q \\ v_q = R_{\text{s}}\,i_q + \dfrac{d\lambda_q}{dt} + j\,\omega\,\lambda_d \end{cases} \tag{3.6}$$

These equations can be represented by means of electrical equivalent circuits, as shown in figure 3.3.

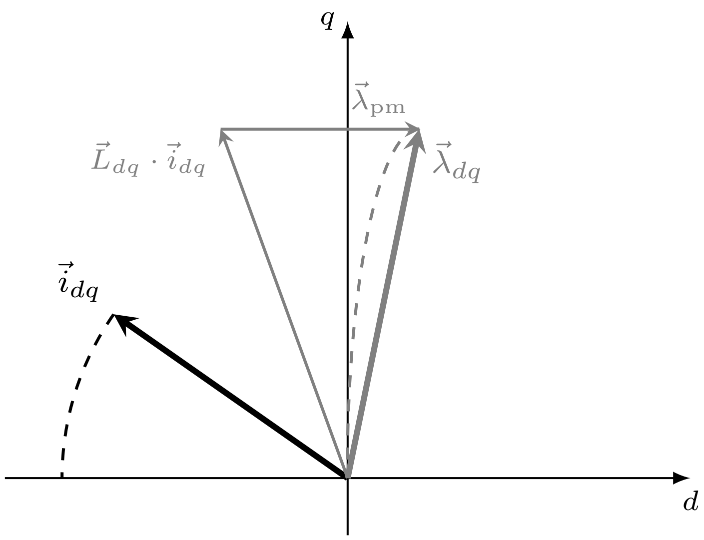

Figure 3.2: Motor dq vector diagram for an ideally infinite CPSR design.

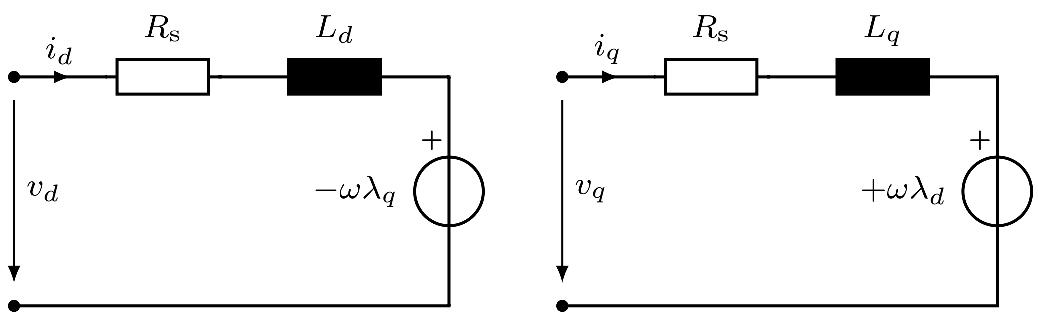

Figure 3.3: Motor equivalent electrical circuits: d-axis (left) and q-axis (right).

The mechanical torque equation is also unaltered between induction and synchronous motors:

$$T = \frac{3}{2}\, p\, (\vec{\lambda}_{dq} \wedge \vec{i}_{dq}) = \frac{3}{2}\, p\, (\lambda_d\, i_q - \lambda_q\, i_d) \tag{3.7}$$

Where p is the number of motor pole pairs and the $3/2$ factor derives from the usual Park and Clarke transformations. Finally, the mechanical power equation can be expressed:

$$P = \frac{T\,\omega}{p} \tag{3.8}$$

Where ω/p is the rotor mechanical angular velocity.

It is worth mentioning that the PMASR motor torque is provided by two different contributions:

- **permanent magnet torque** T_{pm}, generated by the interaction between the stator current and the permanent magnet flux;

- **reluctance torque** T_{r} produced by the interaction between the stator current and its generated flux.

This phenomenon is better illustrated by expanding and recombining equation (3.7):

$$T = T_{\mathrm{pm}} + T_{\mathrm{r}} = \frac{3}{2}\, p \left[\lambda_{\mathrm{pm}}\, i_d + (L_d - L_q)\, i_d\, i_q\right] \tag{3.9}$$

Therefore, the same machine torque performance can be obtained if a reduction in the permanent magnet flux is counteracted by an equivalent increase in the rotor structure anisotropy.

The motor chosen for this dissertation is an IPM synchronous machine, provided by BRUSA Elektronik AG. Because of its high saliency design, this motor qualifies as a PMASR machine. The motor picture and most relevant electromechanical properties are shown in figure 3.4.

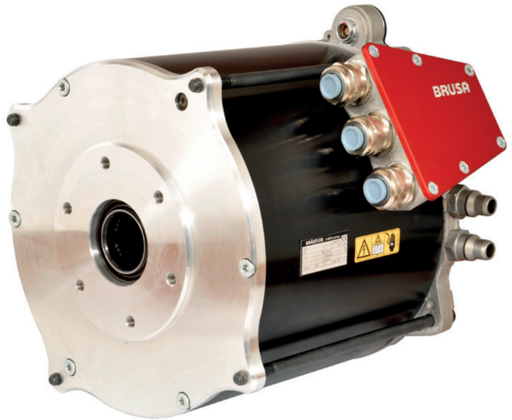

Property	Value
Maximum torque (S1)	165 Nm
Maximum power (S1)	93 kW
Nominal speed	5000 rpm
Maximum speed $n_{\max}$	15 000 rpm
Number of pole pairs p	5
Weight	51 kg
Rotor inertia J_{m}	0.06 $\mathrm{kg\,m^2}$

Figure 3.4: HSM1 - 10.18.13 from BRUSA Elektronik AG [23]: picture (left) and main properties (right) considering $V_{\mathrm{dc}} = 400$ V.

3.2 Flux and Torque Maps

As well known, the motor performance is strictly linked to the magnetic relationship between the stator current and flux linkage (see equation 3.7). Therefore, an accurate extraction of the motor magnetic model is fundamental both for improving the motor electromagnetic design and for implementing the best possible machine control strategy. However, the PMASR current-to-flux relationships can prove to be extremely challenging to model, due to high levels of saturation and cross-coupling effects (typical of SyR machines). A thorough analysis of a PMASR performance and magnetic modeling procedure is provided in [24].

While every electrical machine, independently on its kind, is characterized by magnetic saturation for high flux-density values, the PMASR topology is also subject to a relevant cross-coupling effect, better known as *cross-saturation*. This phenomenon has already been subject of extended analysis in literature, such as in [25–27]. Even though always being present, this effect is particularly evident in high-saliency machines, where rotor flux paths are usually narrower in order to achieve the required anisotropy level. Cross-saturation means that an increase of the d or q axis current value yields a change in the q or d axis flux respectively. This happens because the iron flux paths are shared between the two flux components, therefore an increase of the generated flux on one axis intensifies the saturation on the same path, causing the other flux component to decrease. In particular, the PMASR structure, similar to the transverse laminated SyR one, shows the characteristic iron ribs (see figure 3.1). These structural components have only a mechanical retention function, since they need to contain the rotor iron and the permanent magnets during high-speed, high-centrifugal stress operating conditions. Unfortunately they introduce a magnetic drawback, since they "break" the flux barrier continuity, decreasing the overall saliency ratio. However, because of their narrow section, they already saturate for low current values, thus magnetically behaving as air afterwards and restoring the equivalent rotor anisotropy. It is worth mentioning that, for PMASR machines, iron ribs are normally directly saturated by the permanent magnet flux.

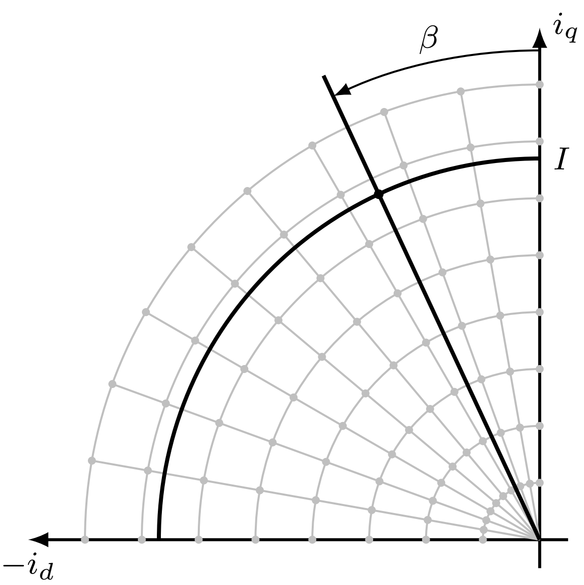

Figure 3.5: Polar grid of the operating points evaluated by FEM simulations in the dq reference frame.

In the present work, the magnetic model of the motor is extracted by means of finite element method (FEM) simulations. The commercial software Flux from CEDRAT has been adopted for the task. Compared to laboratory extraction procedures (see [28,29]), finite element analysis provides the main advantage of not requiring either expensive equipment or validated measurement setups. Nevertheless, the full FEM model of the machine must be available, which is mostly never the case if the motor is purchased. [30] describes an IPM magnetic model extraction procedure based on magneto-static current-driven 2-D FEM simulations. However, in this thesis, magneto-dynamic simulations are performed. While being more cumbersome and time-consuming, these simulations yield more accurate results and they are necessary to obtain an estimation of the iron losses. The phase flux linkage waveform over a full electrical period can be extracted and an FFT analysis is performed to derive phase and magnitude of its first harmonic. This procedure allows to remove the stator slot, stator winding and rotor flux barrier effects from the flux waveform, thus successfully isolating only the torque-generating flux component. Moreover, the flux waveforms can be leveraged to estimate the motor iron losses by means of post-processing calculations.

As well known, the total flux generated by the magnets decreases with temperature. The amount of this performance decline highly depends on the magnet technology. The considered machine is equipped with NdFeB sintered magnets, which are pretty sensitive to temperature variation: a residual flux density coefficient of -0.11 %/°C is provided by the magnet manufacturer. Therefore, a representative operating temperature of 125 °C is chosen for the finite element analysis.

In order to extract satisfactory current-to-flux relationship maps, a large set of (i_d, i_q) working points has to be considered. These points belong to the regular polar grid shown in figure 3.5, where I is the amplitude of the dq current vector (i.e. the peak current value), while β is the angle between the operating point and the q-axis. I

is varied between 0 A and 800 A with a 50 A discretization, while β is varied between 0° (q-axis direction) and 90° ($-d$-axis direction) with 1° steps. A total of 1441 points is evaluated. It is worth mentioning that only the motor operation quadrant has been considered for the flux extraction procedure, since the generator operation quadrant shows a perfect symmetry with respect to the d-axis. The obtained λ_d and λ_q polar maps are then converted into easier-to-use Cartesian maps (i.e. 2-D LUTs), by means of scattered data gridded interpolation in Matlab environment. Therefore, there is no intermediate step adopting conventional d-axis and q-axis inductances. The flux linkages are extracted and directly stored, as in equation (3.4). The main advantage of doing so consists in not separating the contribution of the permanent magnet flux from the current-generated one, which would only require additional effort, yielding no practical benefit. Figure 3.6 shows the extracted $\lambda_d\left(i_d, i_q\right)$ and $\lambda_q\left(i_d, i_q\right)$ 3-D maps. The cross-saturation effect is better highlighted by figure 3.7, which separately shows the d and q flux dependence on i_d and i_q. The complexity of the magnetic model is evident. While $\lambda_q\left(i_q\right)$ has a typical current-to-flux shape, $\lambda_d\left(i_d\right)$ shows a quasi straight line behaviour. This is due to the different flux paths in the d and q directions. While the q path is mostly made up by iron which starts saturating for high current values, the d path encounters a great amount of air (i.e. the flux barriers) and is already mostly saturated by the permanent magnet flux contribution, therefore i_d has little to no influence on the equivalent d inductance value.

The torque map is shown in figure 3.8 and is simply derived from the two flux maps, by means of equation (3.7). The torque iso-level curves are also shown. These curves represent the fundamental component for the motor control strategy identification process.

Since the 2-D FEM simulations only consider the radial electromagnetic phenomena, these models are unable to take into account the end-winding leakage inductance of the machine. The leakage flux doesn't influence the motor torque, but does increase the phase voltage drop during operation. Therefore, to take into account this contribution, an analytical estimation based on geometrical quantities has been performed, yielding an end winding phase leakage inductance value of ~ 1 µH. This value is then included in the phase voltage estimation in equation (3.5).

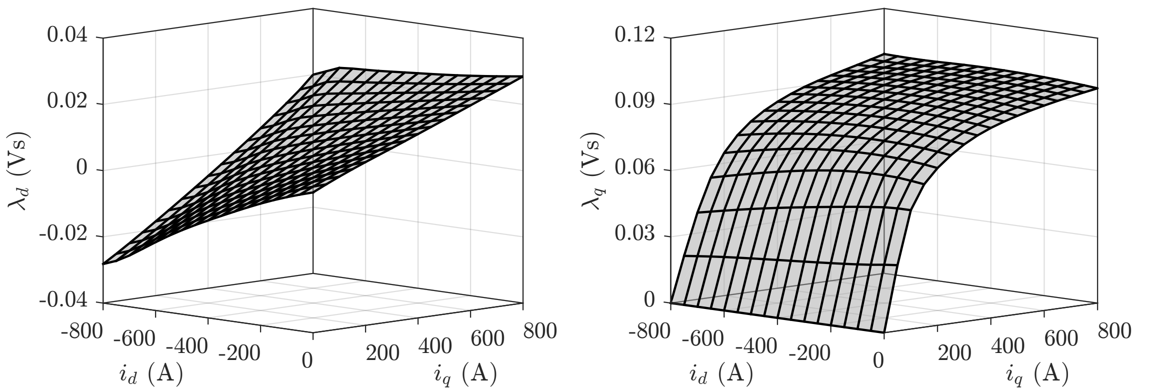

Figure 3.6: Motor current-to-flux relationships: $\lambda_d\left(i_d, i_q\right)$ (left) and $\lambda_q\left(i_d, i_q\right)$ (right).

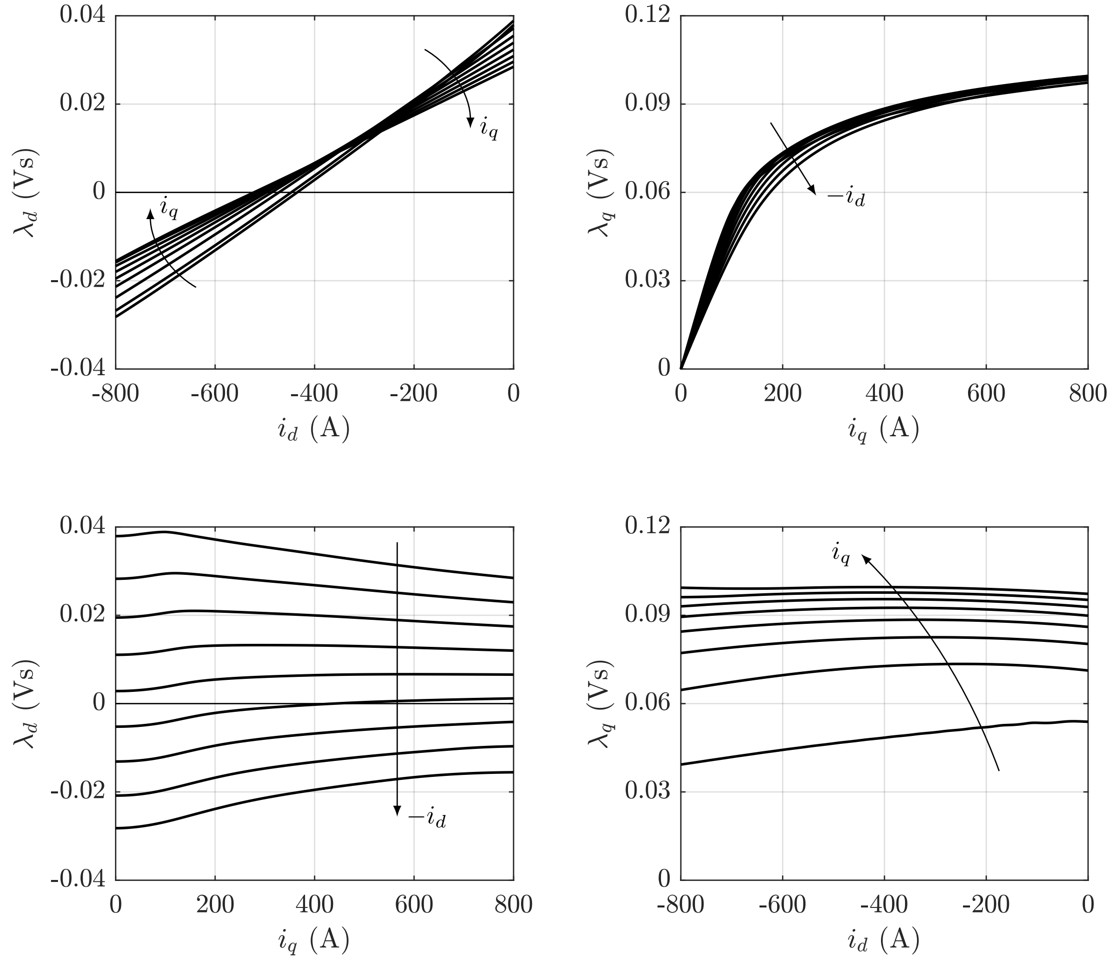

Figure 3.7: Motor current-to-flux relationships: $\lambda_d\,(i_d)$ for different i_q values (top-left), $\lambda_q\,(i_q)$ for different i_d values (top-right), $\lambda_d\,(i_q)$ for different i_d values (bottom-left), $\lambda_q\,(i_d)$ for different i_q values (bottom-right).

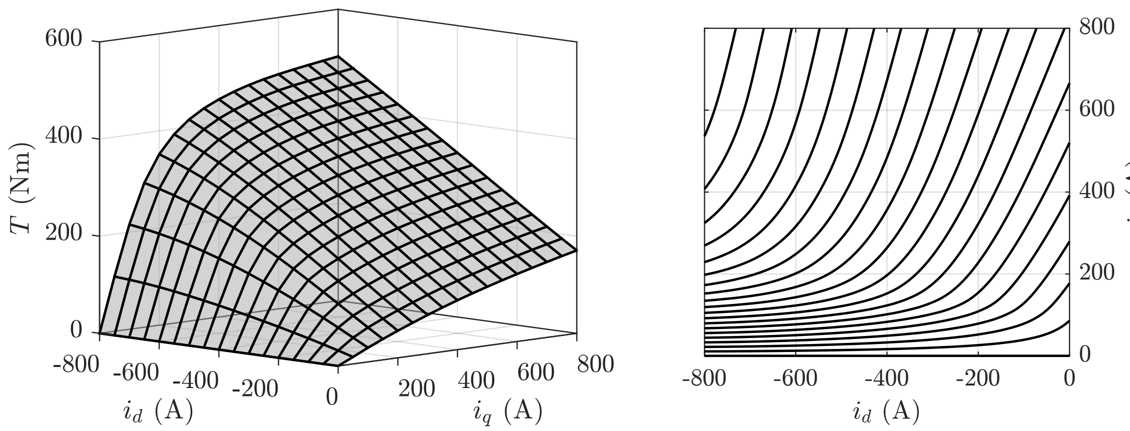

Figure 3.8: Motor torque map (left) and iso-level curves (right) as functions of (i_d, i_q).

3.3 Voltage and Current Limits

Electrical machines have a set of inherent maximum voltage and current values which can be applied to their phase windings. If these values are exceeded, the machine can permanently lose its functionality. The maximum voltage value which the stator winding can withstand is related to the dielectrical strength of the winding insulation material and, if exceeded, can lead to internal short circuits. If current is considered, two distinct maximum values exist for permanent magnet machines:

- instantaneous maximum current; this value is related to the permanent magnet demagnetization. If the current value is high enough, the generated flux can permanently demagnetize portions of the rotor magnets.

- maximum current in continuous operation (I_{S1}); this value is related to thermal issues. The ohmic losses caused by the current flowing in the stator winding heats up the machine, which has an inherent thermal limit related to different aspects, such as the thermal dilatation, the bearing wear, the permanent magnet performance decrease and the life reduction of the winding insulation material. The maximum current in continuous operation for the considered PMASR machine is $\sim$ 210 A_{rms} at 125 °C average stator temperature. This translates in a peak value of:
$$I_{\text{S1}} \approx 300 \text{ A} \tag{3.10}$$

However, while I_{S1} is determined by the machine itself, the practical maximum voltage and current values that can be applied to the motor are inverter-limited. Therefore, the machine transient overload capabilities (i.e. $I > I_{\text{S1}}$) are determined by the power converter design.

The voltage limit is strictly linked to the available DC-link voltage, which, in automotive application, coincides with the battery voltage (400 V in the present case). The maximum output peak phase voltage of a 2-level VSI controlled with SVM is:

$$V_{\text{lim}} = V_{\text{max}} = \frac{V_{\text{dc}}}{\sqrt{3}} \approx 231 \text{ V} \tag{3.11}$$

It is worth noting that this voltage limit value has been derived disregarding the overmodulation possibility. Throughout this work, the SVM technique is only operated in linearity (i.e. $0 \leq m \leq 1$).

The current limit coincides with the inverter rated current, which depends on the number of parallel semiconductor devices per switch. Once the necessary motor torque/power overload is determined by the specific application, the inverter can be designed to withstand the maximum required current value I_{max}. In fact, while the maximum current represents a temporary overload condition for the motor, it is perceived as stationary operation by the power converter. This is due to the fact that the thermal transients of the semiconductor devices ($\sim 10^{-1}$ s) are 2-3 orders of magnitude faster than the machine ones ($\sim 10^1$ - 10^2 s).

Inverter voltage and current limits restrict the so called *feasible operating region* of the motor. In order to show this region on the (i_d, i_q) plane, it is necessary to express the inverter limits as functions of the dq axis currents. The current limit is clear:

$$\sqrt{i_d^2 + i_q^2} \leq I_{\text{lim}} \tag{3.12}$$

Equation (3.12) suggests that the current limit in the (i_d,i_q) is independent on the motor speed and has the shape of a circle. The voltage limit

$$\sqrt{v_d^2 + v_q^2} \leq V_{\text{lim}} \tag{3.13}$$

is not so straightforward to express in terms of dq axis current values, because of the complex 2-D current-to-flux relationships (3.4) and the electrical equation (3.5). To get a better idea of the voltage limit shape on the (i_d, i_q) plane, the following

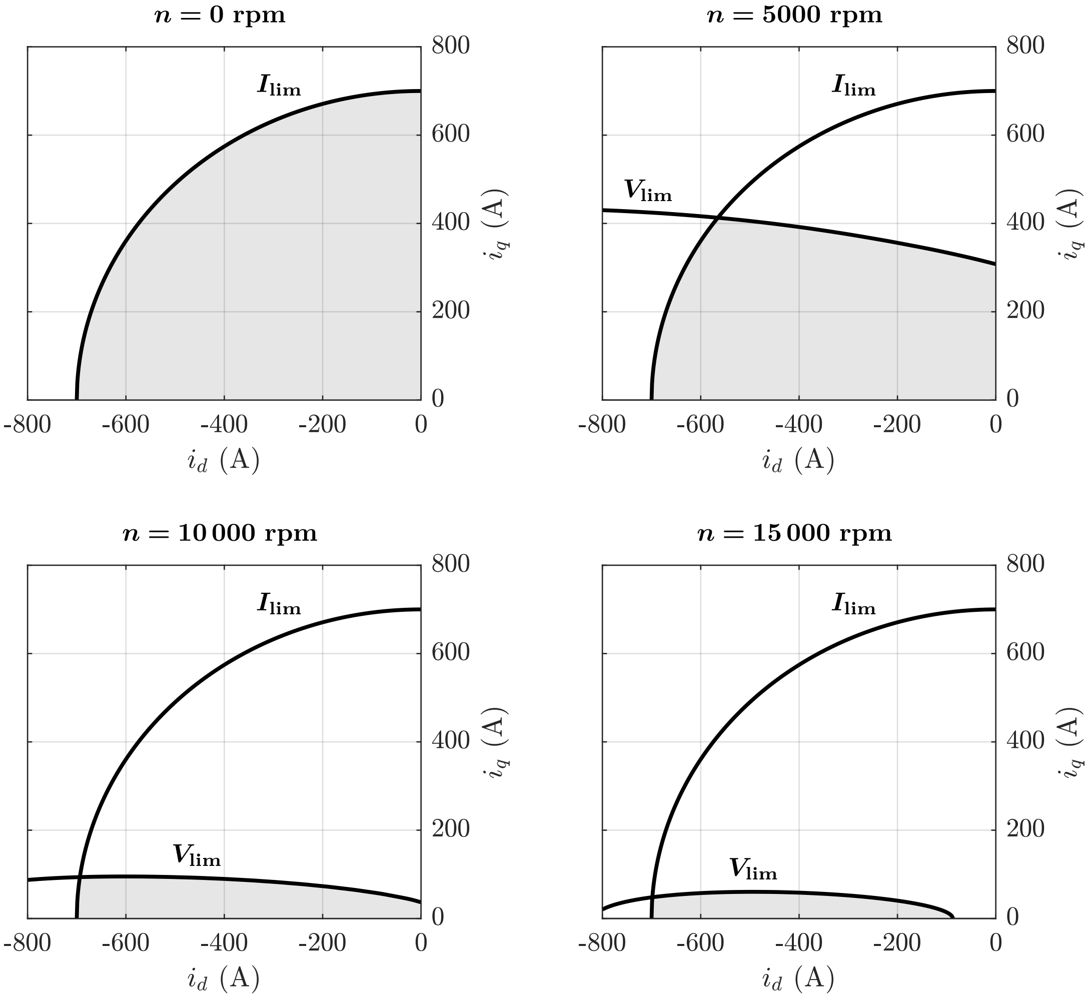

Figure 3.9: Current limit $I_{\text{lim}} = 700$ A and voltage limit $V_{\text{lim}} = 231$ V in the (i_d,i_q) plane for different values of rotating speed. The motor feasible operating region is highlighted in grey.

simplification, valid for sufficiently high speed and/or low current values, is adopted:

$$\begin{cases} v_d \approx -\omega\,\lambda_q \\ v_q \approx \omega\,\lambda_d \end{cases} \tag{3.14}$$

As a consequence, the voltage limit relation can be approximated as:

$$\sqrt{\lambda_d^2 + \lambda_q^2} \leq \frac{V_{\text{lim}}}{\omega} \tag{3.15}$$

Where λ_d and λ_q are a function of both i_d and i_q. By the inversion of the current-to-flux relationships it is thus possible to determine the voltage limit in the (i_d, i_q) plane as a function of the motor speed. It is worth reminding the relationship between the motor electrical frequency ω and the mechanical rpm speed of the machine n:

$$n = \frac{60}{2\,\pi}\,\frac{\omega}{p} \tag{3.16}$$

Figure 3.9 displays the current and voltage limits in the (i_d, i_q) plane as a function of the motor speed, while highlighting the motor feasible operating area.

By tracing the maximum torque point in the feasible operating region as a function of the machine speed, it is possible to derive the motor maximum torque-speed and power-speed curves for a given set of current and voltage limits. While the voltage limit is not a variable, since it only depends on the battery voltage, the current limit can be increased by means of the inverter design (i.e. adding power semiconductor devices in parallel). Figure 3.10 shows the maximum T-n and P-n curves as functions of the current limit I_{lim}, with an available DC-link bus voltage $V_{\text{dc}} = 400$ V. It is worth noting the wide CPSR typical of PMASR machines: when the inverter voltage limit is reached, near to the base speed value, the torque curves start decreasing with an approximate $\propto 1/n$ behaviour and the power stays nearly constant, especially for current values similar to I_{S1}.

3.4 Fundamental Losses

Motor fundamental losses refer to those power loss components which are generated in the machine when it is supplied by an ideal sinusoidal source. These losses characterize the machine itself, as they only depend on the motor design and the operating point. They are therefore independent on the power inverter switching frequency and modulation scheme.

As this work considers an already available motor, fundamental losses cannot be optimized during the design phase. However, since these loss components depend on the electrical and/or mechanical operating point, they must be accurately modeled in order to derive the minimum system loss control strategy.

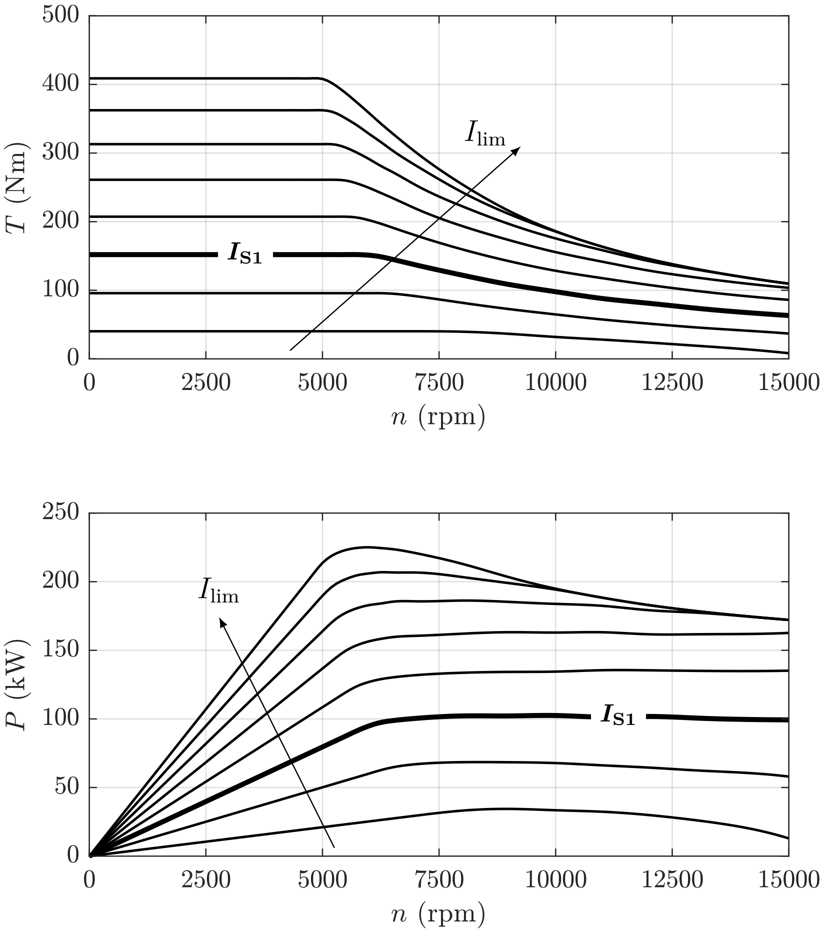

Figure 3.10: Maximum motor torque (top) and power (bottom) as a function of speed for $V_{\mathrm{lim}} = 231$ V and different values of $I_{\mathrm{lim}} = 100, 200, \ldots, 800$ A. $I_{S1} = 300$ A is highlighted.

3.4.1 Copper Losses

The motor copper losses, also known as winding losses or ohmic losses, are generated by the current flow into the stator windings:

$$P_{\mathrm{Cu}} = \frac{3}{2} R_{\mathrm{s}} I^2 \tag{3.17}$$

Where R_{s} is the stator phase resistance and I is the peak value of the motor phase current. R_{s} has been measured at 25 °C, resulting in a 5.85 mΩ value. Since the electrical resistivity of metal (copper in this case) depends on temperature, the aforementioned 125 °C reference value has been considered for the resistance evaluation:

$$R_{\mathrm{s}}\,(125°\mathrm{C}) = R_{\mathrm{s}}\,(25°\mathrm{C}) \left[1 + \alpha_{\mathrm{Cu}}\,(125°\mathrm{C} - 25°\mathrm{C})\right] \approx 8.2\ \mathrm{m}\Omega \tag{3.18}$$

Where $\alpha_{\mathrm{Cu}} = 4.04 \times 10^{-3}\ \mathrm{K}^{-1}$ is the copper resistivity temperature coefficient.

Depending on the conductor cross-section area, when high electrical frequencies are involved, skin and proximity effects should also be taken into account. However,

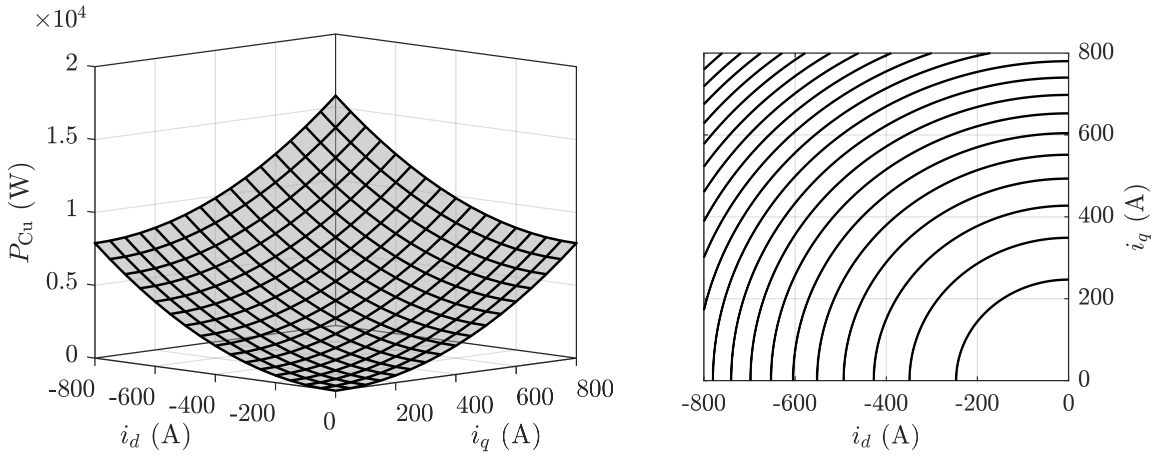

Figure 3.11: Motor copper loss map (left) and iso-level curves (right) as functions of (i_d, i_q).

these effects are here neglected, since the stator winding has been designed with a high number of wires per strand to minimize high frequency repercussions.

Figure 3.11 shows the copper loss map and iso-level curves as functions of (i_d, i_q). The circular shape of the P_{Cu} iso-level curves is due to equation (3.17), since they directly reflect constant I curves.

3.4.2 Iron Losses

Iron losses, also known as core losses or magnetic losses, are generated by the alternating flux density in the stator and rotor cores of the machine. These losses are traditionally split into:

- **hysteresis losses**, which relate to the hysteresis properties of ferromagnetic materials;
- **eddy current losses**, which are generated by the induced voltages and consequent currents in the conducting magnetic material.

Other than having a complex behaviour, iron losses cannot be directly measured, thus only indirect extraction procedures can be carried out. This poses a great limit to the accuracy level of iron loss data. Iron sheet manufacturers always provide the specific loss data of their materials, however the subsequent manufacturing process to assemble the finished machine can create big discrepancies between datasheet and real values. These inconsistencies can be reduced by means of "loss correction" factors obtained by suitable measurements on the assembled machine. However, for simplicity reasons, the here derived model is directly based on the available manufacturer loss data.

Due to their complex behaviour, depending on frequency and flux density, iron losses represent also a modeling challenge. A comprehensive comparison of the most adopted iron loss models in literature is provided in [31]. A modified version of the Steinmetz equation is here adopted, which articulates the specific iron losses (W/kg)

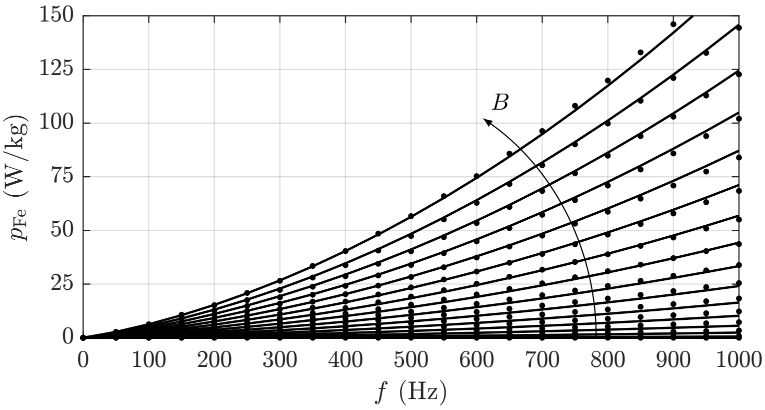

Figure 3.12: Iron loss data provided by the manufacturer (dots) and fitted curves (lines). f values 0, 50, ..., 1000 Hz, B values 0, 0.1, ..., 1.5 T.

as a function of peak flux density (B) and frequency (f):

$$p_{\mathrm{Fe}} = k_{\mathrm{h}}\, f^{\alpha}\, B^{\beta} + k_{\mathrm{e}}\, f^{2}\, B^{2} \tag{3.19}$$

Where k_{h}, k_{e}, α and β are coefficients which depend on the adopted ferromagnetic material. The standard Steinmetz equation is changed by the addition of a second term, which aims to consider the eddy current contribution to the total loss amount. Moreover, being α and β adjustable, the first term tries to take into account both the hysteresis and the anomalous (or excess) loss components. All of the parameters in equation (3.19) are extracted by fitting the manufacturer loss data, as shown in figure 3.12. The fitting procedure yields the following coefficients: $k_{\mathrm{h}} = 1.358 \times 10^{-2}$, $k_{\mathrm{e}} = 4.690 \times 10^{-5}$, $\alpha = 1.084$ and $\beta = 2.373$.

In order to derive the total iron loss value (P_{Fe}) for each (i_d, i_q) operating point, the aforementioned magneto-dynamic FEM simulations have been leveraged. The flux density knowledge in each point of the domain (i.e. stator and rotor cores) as a function of time is already available. In post-processing, it is thus possible to calculate the specific iron losses in every point of the domain by means of equation (3.19) and integrate these values over the whole machine cross-section and stack length. These losses are extracted at the motor rated speed (i.e. 5000 rpm) and are shown in figure 3.13. Nevertheless, the obtained loss map can be easily extrapolated for every speed value belonging to the machine operating range. With the simplifying assumption that the variation frequency of local flux densities in the stator and rotor cores is proportional to the machine speed, it is possible to adopt the following extrapolating relation:

$$P_{\mathrm{Fe}} = P_{\mathrm{Fe,hys}} \left(\frac{n}{n_{\mathrm{ref}}}\right)^{\alpha} + P_{\mathrm{Fe,eddy}} \left(\frac{n}{n_{\mathrm{ref}}}\right)^{2} \tag{3.20}$$

Where $P_{\mathrm{Fe,hys}}$ and $P_{\mathrm{Fe,eddy}}$ are respectively the hysteresis and eddy-current loss components calculated at the reference motor speed n_{ref}, while n is the operating motor speed.

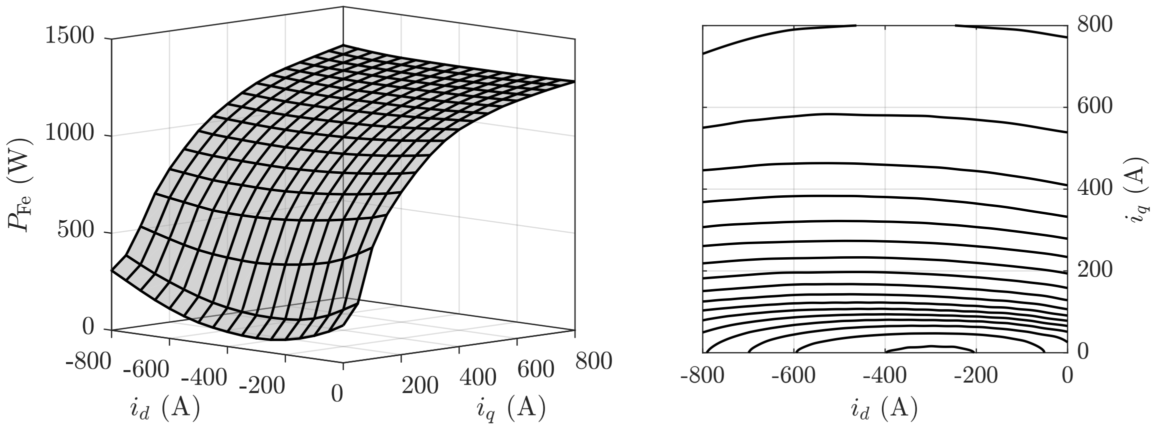

Figure 3.13: Motor iron loss map (left) and iso-level curves (right) as functions of (i_d, i_q) for $n = 5000$ rpm.

3.4.3 Permanent Magnet Losses

Losses inside the PMs are generated by the changing flux density in the magnet volume. Since the PM material has a non-negligible electrical conductivity, alternating magnetic fields lead to an eddy-current flow and thus to power losses. These losses represent a substantial issue in PMSMs since every magnet technology has a temperature threshold (Curie point) beyond which the material permanently loses its magnetic capabilities (i.e. the residual flux density). Moreover, the magnetic characteristics of the material rapidly worsen with increasing temperature, leading to a decrease in the motor performance. Therefore, in order to keep the magnet temperature from rising excessively, it is of utmost importance to estimate and limit PM losses.

While in SPM machines PM losses can be significant, since the magnets directly face the air gap and are thus subject to the high frequency magnetic field harmonic components (due to slotting, non-sinusoidal winding distribution, etc.), in IPM machines these losses are normally very low, as the magnets are "shielded" by the rotor iron.

FEM simulations, considering the magnet volume as a solid block with a finite electrical conductivity, confirm the theoretical suppositions, yielding negligible PM loss values in all operating conditions:

$$P_{\mathrm{pm}} \approx 0 \tag{3.21}$$

3.4.4 Mechanical Losses

Motor mechanical losses are normally subdivided into two contributions:

- **friction losses**, caused by the mechanical resistance of the bearings;
- **windage losses**, generated by the air drag on the machine rotor surface.

A resistive mechanical torque T_{m} is applied to the rotating machine and it increases with the mechanical speed ω_{m}, thus becoming relevant at high speed operation. The

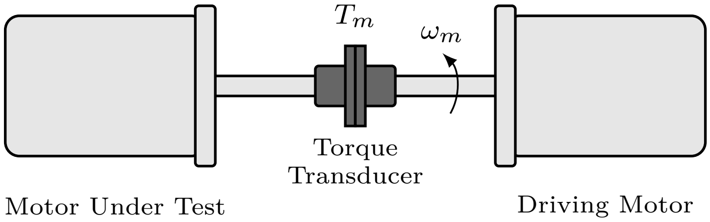

Figure 3.14: Motor mechanical loss measurement setup.

mechanical power losses are therefore defined:

$$P_{\mathrm{m}} = \omega_{\mathrm{m}}\, T_{\mathrm{m}}(\omega_{\mathrm{m}}) = k_a\, \omega_{\mathrm{m}}^{k_b} \tag{3.22}$$

Where k_a and k_b are two coefficients which depend on the specific motor.

In order to estimate the mechanical loss dependence on speed a measurement procedure is carried out. The resistive mechanical torque is measured by means of a torque transducer, while a speed-controlled external motor drives the machine under test in a no-load condition. The test setup is shown in figure 3.14. This test is performed for different values of mechanical speed, ranging from 0 to 10 000 rpm and a mechanical power loss curve is thus extracted. Finally, this curve is fitted with equation (3.22) yielding $k_a = 5.756 \times 10^{-3}$ and $k_b = 1.816$. The result is shown in figure 3.15.

It is worth noting that, because of their only dependence on operating speed, mechanical losses cannot be subject to optimization by means of control strategies. However, they are taken into account in this work in order to have a better estimation of the overall drive train efficiency.

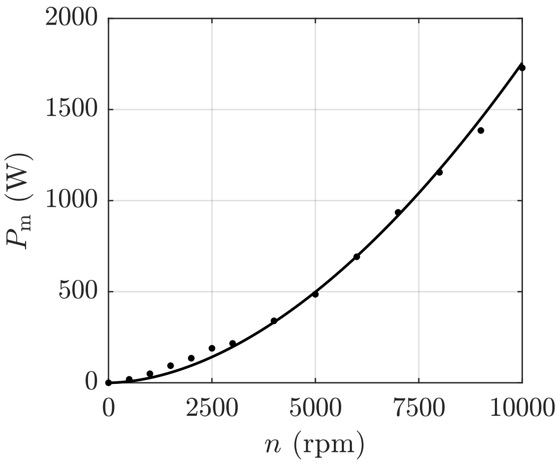

Figure 3.15: Motor mechanical loss as a function of speed: measured data (dots) and fitted curve (line).

3.5 Harmonic Losses

It is well known that distorted (i.e. non-sinusoidal) supply voltages lead to an increase in the machine losses. Voltage harmonics generate harmonic currents, which increase the total RMS current value, and create high-frequency asynchronous rotating magnetic fields in the motor air gap, which cause additional iron losses in the stator and rotor cores. Overall, this loss increase in the machine is commonly known as harmonic loss component. It is worth emphasizing that these losses are unrelated to the flux harmonics generated by the non-sinusoidal distribution of the stator winding or the motor slotting effects (space-harmonics), but they are only referred to the time-harmonics introduced by the switching operation of the inverter.

Many studies have already been carried out in literature to understand the effect of a PWM inverter supply on the iron core losses of electrical machines [32–39], however it still represents an open topic, since it has not been fully comprehended. Moreover, the determination of the inverter-related harmonic loss component represents a substantial challenge, since these losses make up a small fraction of the total motor power. Different measurement approaches can be found in [31, 40].

Harmonic losses can be normally distincted in two different contributions [3]:

- **copper losses**; generated by the harmonic currents I_h flowing in the stator winding. These currents can be expressed in terms of the harmonic voltages V_h, with the simplifying assumption that the winding inductance (either L_d or L_q) dominates the overall impedance:

$$P_{\mathrm{Cu,h}} = \frac{3}{2} R_{\mathrm{s}} {I_{\mathrm{h}}}^2 \approx \frac{3}{2} R_{\mathrm{s}} \left(\frac{V_{\mathrm{h}}}{2\,\pi\, f_{\mathrm{h}}\, L} \right)^2 \propto \frac{1}{{f_{\mathrm{h}}}^2} \tag{3.23}$$

  Where $P_{\mathrm{Cu,h}}$ is the additional copper loss generated by the h-order harmonic. The harmonic copper losses thus decay with the squared harmonic frequency. Even if conductor skin effect is taken into account, which causes the winding resistance to increase $\propto \sqrt{f_{\mathrm{h}}}$, the harmonic copper losses show a $\propto 1/{f_{\mathrm{h}}}^{1.5}$ behaviour.

- **iron losses**; generated by the flux density variation in the stator and rotor cores of the machine. If an average area for the different flux paths is assumed, the average harmonic flux density peak value B_h is directly linked with the harmonic voltage V_h:

$$B_{\mathrm{h}} \propto \frac{V_{\mathrm{h}}}{f_{\mathrm{h}}} \tag{3.24}$$

  Therefore, the hysteresis and eddy current contributions to the harmonic iron losses can be expressed as a function of the harmonic frequency:

$$\begin{cases} P_{\mathrm{Fe,hys,h}} \propto f_{\mathrm{h}}\, {B_{\mathrm{h}}}^{\beta} \propto {f_{\mathrm{h}}}^{1-\beta}\, V_{\mathrm{h}}^{\beta} \propto \dfrac{1}{{f_{\mathrm{h}}}^{\beta-1}} \\ P_{\mathrm{Fe,eddy,h}} \propto {f_{\mathrm{h}}}^2\, {B_{\mathrm{h}}}^2 \propto V_{\mathrm{h}}^2 \propto \mathrm{cost} \end{cases} \tag{3.25}$$

  Where $\beta > 1$ is the exponent coefficient which defines the hysteresis loss dependence on flux density.

With increasing frequency, harmonic iron losses become rapidly dominant over copper losses [32, 41, 42]. This is because the frequency dependent increase in winding resistance caused by skin and proximity effects cannot counteract the rapid decrease in the current harmonic amplitude, as previously mentioned. Moreover, the conductor skin effect usually starts having a significant effect at very high frequencies, since high speed machines are normally wounded with a high number of wires per strand. It is worth mentioning that permanent magnet losses in IPM machines do not provide a significant contribution to the total harmonic losses, for the same reasons as the fundamental losses: the solid magnets are in fact "shielded" from the harmonic flux variations thanks to the rotor iron.

Equation (3.25) highlights that also hysteresis losses rapidly decrease with frequency ($\beta \approx 2$), leaving the eddy current contribution to dominate the total harmonic loss at high frequencies. While this loss component does apparently not depend on the harmonic frequency, its constant behaviour starts vanishing for frequency values high enough to trigger the skin effect in the iron lamination (i.e. 10 - 100 kHz). Therefore, (3.25) is no longer valid in this frequency range.

3.5.1 Reflected Impedance

The effect of the eddy currents on thin iron sheets has been extensively analysed in literature [43, 44] and the main results are reported in the following. The equivalent motor magnetic model proposed by Polinder [42] is here adopted to evaluate the eddy current effects on the machine lamination. This model is sketched in figure 3.16 and it consists in a laminated core (dark gray), with length l_{Fe} and sheet thickness t_{Fe}, an air gap with length l_{air} and an ideal core (light gray) to close the magnetic flux lines. Moreover, an energizing coil is wounded around the iron core, which represents the machine phase winding. In order to effectively solve the Maxwell equations in the iron lamination, the following assumptions are made:

- the ideal core has infinite resistivity (no eddy current losses) and infinite permeability (no magneto-motive force drop);

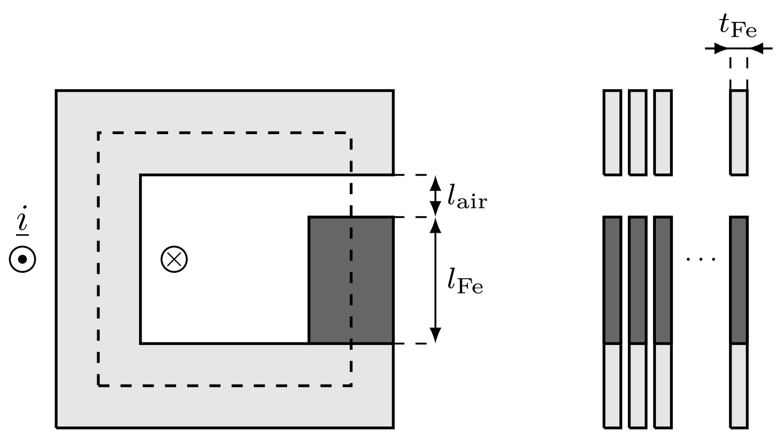

Figure 3.16: Simplified motor magnetic model for the high-frequency eddy current analysis.

- the magnetic field varies sinusoidally in time;
- the leakage flux is negligible (all flux lines remain in the magnetic circuit);
- the flux lines in the iron core and in the air gap are parallel to the dashed line in figure 3.16;
- the end effects are neglected.

It is also useful to define the *skin depth* (or penetration depth):

$$\delta = \sqrt{\frac{2\,\rho_{\mathrm{Fe}}}{\omega\,\mu_0\,\mu_{\mathrm{r,Fe}}}} \tag{3.26}$$

Where ρ_{Fe} and $\mu_{\mathrm{r,Fe}}$ are the electrical resistivity and the relative magnetic permeability of the iron lamination material. It is now possible to identify the relation between the current $\underline{i}$ flowing in the energizing winding and its flux linkage $\underline{\lambda}$ [42]:

$$\underline{\lambda} = \frac{1 + \dfrac{l_{\mathrm{Fe}}}{l_{\mathrm{air}}\,\mu_{\mathrm{r,Fe}}}}{1 + \dfrac{l_{\mathrm{Fe}}}{l_{\mathrm{air}}\,\mu_{\mathrm{r,Fe}}}\,\dfrac{\underline{a}\,t_{\mathrm{Fe}}}{2}\,\dfrac{\cosh\left(\frac{1}{2}\,\underline{a}\,t_{\mathrm{Fe}}\right)}{\sinh\left(\frac{1}{2}\,\underline{a}\,t_{\mathrm{Fe}}\right)}}\,L_0\,\underline{i} \tag{3.27}$$

Where L_0 is the inductance of the stator winding at $f = 0$, $\underline{a}$ is defined as

$$\underline{a} = \frac{1 + j}{\delta} \tag{3.28}$$

and the term

$$\underline{\mu_{\mathrm{e}}} = \mu_0\,\mu_{\mathrm{r,Fe}}\,\frac{2}{\underline{a}\,t_{\mathrm{Fe}}}\,\frac{\sinh\left(\frac{1}{2}\,\underline{a}\,t_{\mathrm{Fe}}\right)}{\cosh\left(\frac{1}{2}\,\underline{a}\,t_{\mathrm{Fe}}\right)} \tag{3.29}$$

is commonly known as *complex permeability* [44]. It is worth noting that the underline symbol indicates complex quantities.

The impedance of the energizing coil, or the equivalent impedance seen by the motor phase terminals, has the following expression:

$$\underline{Z} = R_{\mathrm{s}} + j\,\omega\,\frac{\underline{\lambda}}{\underline{i}} \tag{3.30}$$

The term

$$\underline{Z_{\mathrm{e}}} = j\,\omega\,\frac{\underline{\lambda}}{\underline{i}} = R_{\mathrm{e}} + j\,\omega\,L_{\mathrm{e}} \tag{3.31}$$

is commonly known as *reflected impedance* and contains a real part R_{e}, representing the iron core losses, and an imaginary part $j\,\omega\,L_{\mathrm{e}}$ defining the current-to-flux relationship. Figure 3.17 shows the high-frequency single-phase equivalent circuit of the machine stator winding. It is worth noting that R_{s}, R_{e} and L_{e} all depend on frequency.

From equations (3.27) and (3.31) it is evident that the presence of eddy currents in the iron lamination changes the equivalent impedance of the winding. However,

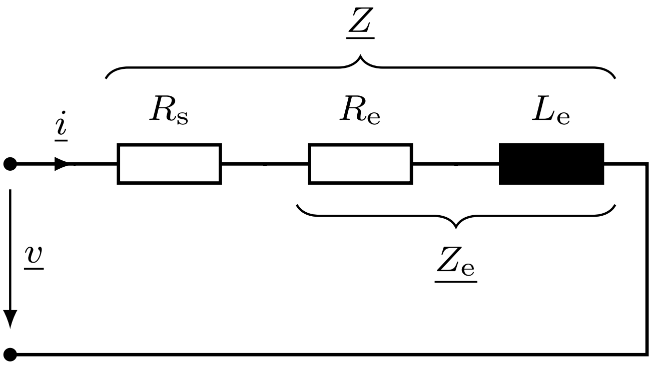

Figure 3.17: High-frequency single phase equivalent circuit of the motor.

this rate of change highly depends on the frequency range involved. There are three main frequency regions where a different impedance and loss behaviour is observed. Figure 3.18 shows the frequency behaviour of the resistance, inductance and impedance of the energizing winding in these three different regions:

(A) **dominant copper losses**; the resistance and inductance show a constant behaviour (they maintain their zero frequency value) and, being the reactance contribution ωL dominant, the impedance rises $\propto f$. The equivalent resistance behaviour $R \approx R_s$ shows that in this region iron losses are negligible compared to ohmic losses.

(B) **dominant iron losses** and $\boldsymbol{\delta \gg t_{Fe}}$; the eddy currents, while still not causing a sensible magnetic field displacement (i.e. $L \approx$ cost), become the dominant loss contribution. This is reflected in the resistance value, which starts rising $\propto f^2$ and totally dominates R_s. The equivalent impedance continues to increase $\propto f$, as the reactance still represents its major component. This region is also known as *resistance limited* eddy current region.

(C) **dominant iron losses** and $\boldsymbol{\delta \ll t_{Fe}}$; the eddy currents cause a non-negligible magnetic field displacement and both current and flux density in the lamination start to concentrate towards its surface. The eddy current reaction to the incoming flux density is reflected into the inductance value, which starts decreasing $\propto 1/\sqrt{f}$. However, since the flux concentrates towards the iron sheet edges, the flux lines exploit a narrower section of the lamination, causing an overall loss decrease. This region is also known as *inductance limited* eddy current region.

The frequency value for which $\delta = t_{Fe}$ is also known as *frequency limit of the lamination*, as it separates the resistance-limited and inductance-limited eddy current regions.

The h-order harmonic power losses can be expressed as:

$$P_h = \frac{3}{2} R \, {I_h}^2 = \frac{3}{2} {V_h}^2 \frac{R}{Z^2} \propto \frac{R}{Z^2} \tag{3.32}$$

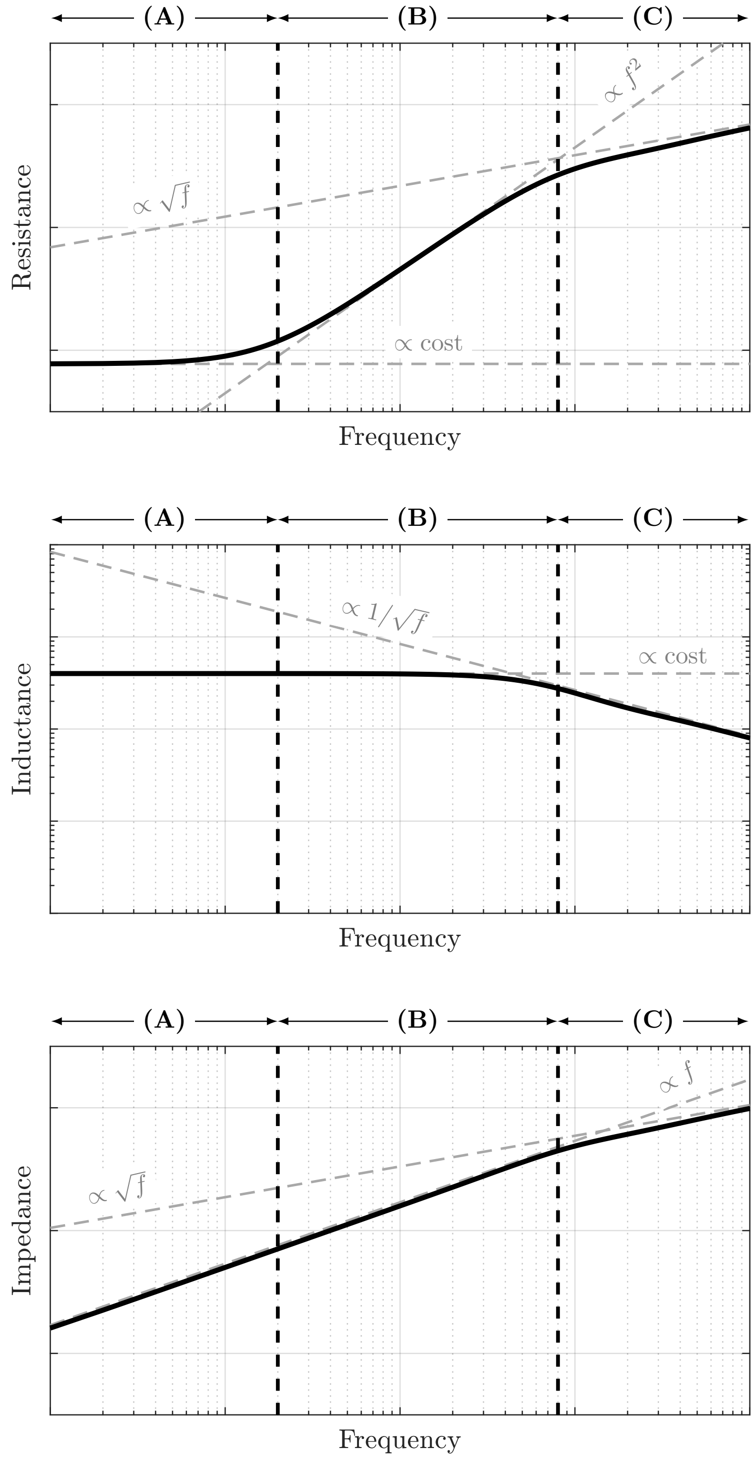

Figure 3.18: Frequency dependence of the stator winding resistance (top), inductance (middle) and impedance (bottom) according to equations (3.27) and (3.31).

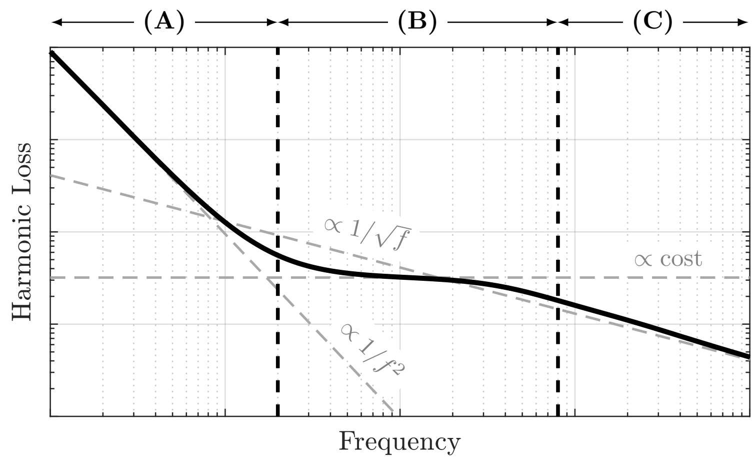

Figure 3.19: Frequency dependence of the harmonic power losses.

Where $R = R_\mathrm{s} + R_\mathrm{e}$ is the total equivalent resistance. Figure 3.19 shows the harmonic power loss behaviour in the three aforementioned frequency regions. In region (A) the losses are dominated by the ohmic component and decrease $\propto 1/f^2$. In region (B) eddy current losses become dominant and, since the magnetic field displacement effect is still insignificant, the losses show a flat behaviour as in equation (3.25). Finally, in region (C) the eddy currents start affecting the flux distribution and the losses restart decreasing $\propto 1/\sqrt{f}$.

The impedance-based harmonic loss model here introduced provides a great simplification in the measurement procedure, compared to harmonic injection [40] or direct/indirect loss measurements [31]. This is because only impedance measurements are needed. Nevertheless, for this extraction procedure to be meaningful, some assumptions must be justified:

- the measurements are carried out with a locked-rotor; in a real condition, the three-phase inverter voltage time-harmonics generate rotating magnetic fields with a rotational frequency equal to their harmonic order. For this assumption to be justified, the usual rotating frequency of these fields must be much higher than the motor rotating speed, so that the rotor can be considered at standstill. Since the lowest harmonic frequency is strictly linked to f_sw and being $f_\mathrm{sw} \gg f$ for control purposes, this assumption in verified.

- the measurements are performed injecting an alternating field (i.e. not rotating); the additional loss effects of field rotation compared to a simple pulsating field are neglected, however these effects are normally negligible for non-oriented Si-Fe laminations.

- the impedance is measured in a no-load condition; harmonic losses depend on the machine load for low frequency values (i.e. when copper losses dominate), since the iron core saturation causes the inductance to drop and the ohmic losses to increase, according to equation (3.23). However, for higher frequency values the eddy current loss component becomes dominant and, since it is directly determined by the harmonic voltages, losses become nearly independent on load conditions [40,41].

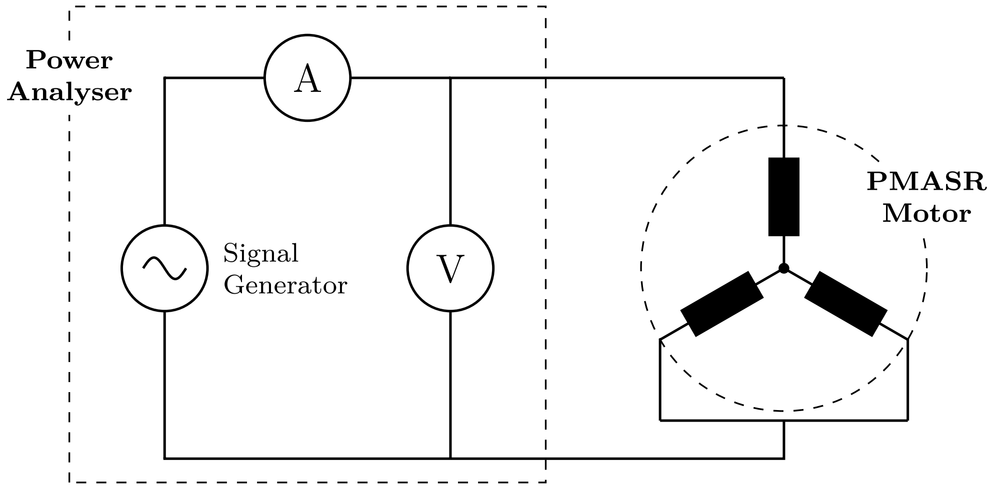

Figure 3.20: Test setup for the high-frequency machine impedance measurement.

The test setup is shown in figure 3.20, where the machine connection to the power analyser is illustrated. The role of the power analyser is to apply variable-frequency sinusoidal voltage waveforms to the stator winding terminals, while measuring the amplitude and phase of both current $\underline{i}(f)$ and voltage $\underline{v}(f)$. The equivalent phase impedance is thus obtained:

$$\underline{Z}(f) = \frac{2}{3}\,\frac{\underline{v}(f)}{\underline{i}(f)} \tag{3.33}$$

Where the 2/3 factor is due to the phase winding connection. The resistance and inductance values can finally be extracted:

$$\begin{cases} R(f) = \mathrm{Re}\left[\underline{Z}(f)\right] \\ L(f) = \dfrac{1}{2\,\pi\,f}\,\mathrm{Im}\left[\underline{Z}(f)\right] \end{cases} \tag{3.34}$$

Since the PMASR motor, as all of the IPM machines, is characterized by an anisotropic structure (i.e. $L_d \neq L_q$), the phase winding equivalent impedance is highly affected by the rotor position. This issue can be solved by simply measuring the phase impedance for different selected rotor positions and averaging the results. This has been done for six different rotor angular positions, equispaced by 12 mechanical degrees (i.e. 60 electrical degrees for the adopted 10 pole motor). The results are shown in figure 3.21, where the averaged phase resistance and inductance are illustrated in a 100 Hz - 100 kHz frequency range. Overall, a good level of correlation with the predictions is observed, however it is worth pointing out that the transition between regions (B) and (C) only starts towards the end of the measured frequency range (i.e. 10 - 100 kHz).

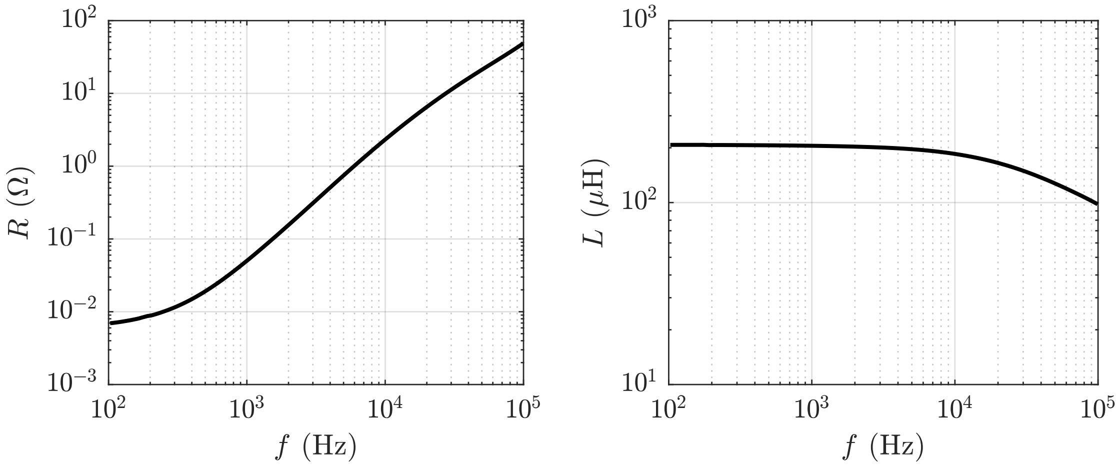

Figure 3.21: High frequency equivalent resistance (left) and inductance (right) of the PMASR motor.

3.5.2 Loss Factor Curve

The h-order harmonic power loss, detailed in equation 3.32, can be normalized by the squared peak amplitude of the harmonic voltage. By doing so, the so called *harmonic loss factor* is obtained:

$$LF(f_h) = \frac{P_h}{V_h^2} = \frac{3}{2}\frac{R(f_h)}{Z^2(f_h)} \tag{3.35}$$

An harmonic loss expression independent on V_h is obtained, therefore the additional machine losses caused by a certain harmonic order can be characterized by a unique f_h-dependent loss factor curve. This concept was first introduced in [41] and applied to induction machines, but has also been validated by more recent studies [40, 45]. The extracted loss factor curve of the PMASR motor is shown in figure 3.22. The LF shape resembles the predicted harmonic power loss frequency dependence of figure 3.19 and the three different loss regions can be identified by the slope changes of the curve.

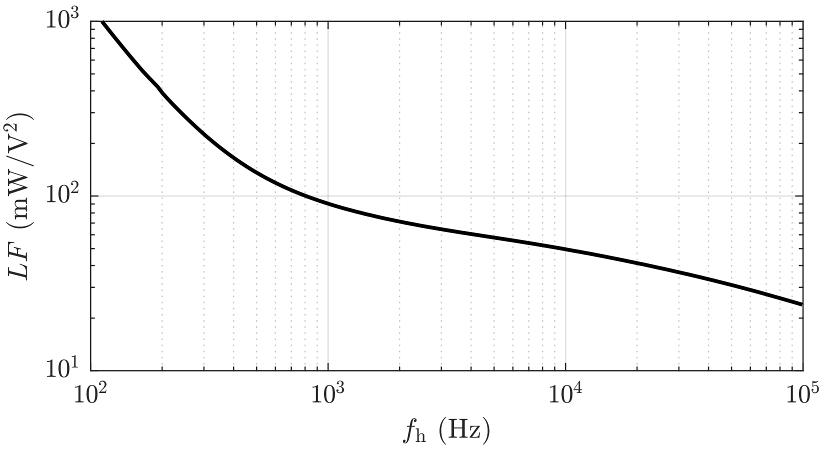

Figure 3.22: Harmonic loss factor curve of the PMASR motor.

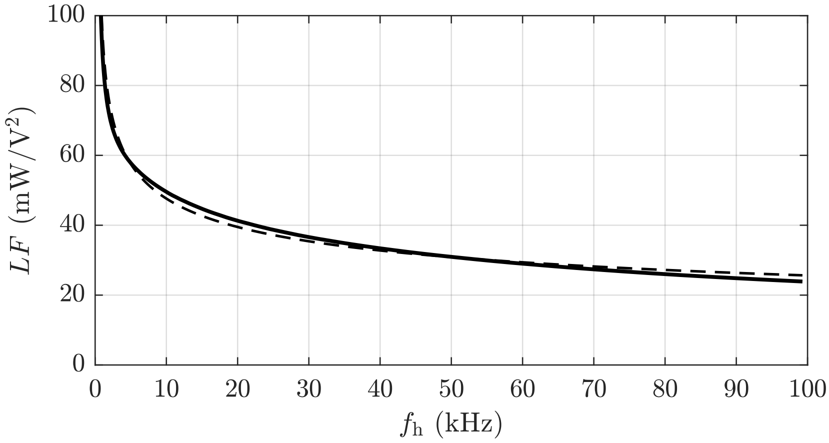

Figure 3.23: Harmonic loss factor curve of the PMASR motor in a linear scale: measured (full line) and fitted (dashed line) data.

The total harmonic losses caused by the distorted supply voltage can be derived by superimposition: the loss contributions of different time harmonics can be separately calculated and added. If the output voltage spectrum of the inverter is known, evaluating the motor harmonic power loss simply consists in taking one voltage harmonic V_h at a time, squaring it, and multiplying the result by $LF(f_h)$. The summation of every harmonic contribution provides the total loss:

$$P_{h,\mathrm{tot}} = \sum_{h=2}^{\infty} LF(f_h)\, V_h^2 \tag{3.36}$$

From a theoretical standpoint, however, the additivity of the loss components is not given for hysteresis losses. Nevertheless, as previously shown, frequency regions (B) and (C) are totally dominated by eddy current losses, which are additive. Being the considered switching frequencies restricted to $f_\mathrm{sw} > 10$ kHz in order to achieve a satisfactory control performance (the motor maximum fundamental frequency is ~ 1000 Hz), the whole voltage harmonic spectrum resides in the aforementioned frequency regions and the superimposition principle is valid.

In order to effectively use the loss factor curve for the harmonic loss calculations, the extracted data are fitted by means of a least-square algorithm with the following function:

$$LF(f_h) = \frac{k_\mathrm{a}}{f_h^\mathrm{a}} + \frac{k_\mathrm{b}}{f_h^\mathrm{b}} \tag{3.37}$$

The fitting results are shown in a linear scale in figure 3.23 and the correlating coefficients are thus obtained: $k_\mathrm{a} = 0.566$, $k_\mathrm{b} = 2.038 \times 10^4$, a $= 0.269$, b $= 2.138$.

With the availability of the motor loss factor curve it is possible to compare modulation techniques by their effective influence on the harmonic losses. The comparison between total harmonic losses caused by continuous and discontinuous SVM strategies is shown in figure 3.24. The loss dependence on both peak phase voltage V and switching frequency f_sw is presented.

Since, for the reasons illustrated in chapter 2, doubling the switching frequency for the 5-segment SVM strategy approximately yields the same switching losses as the

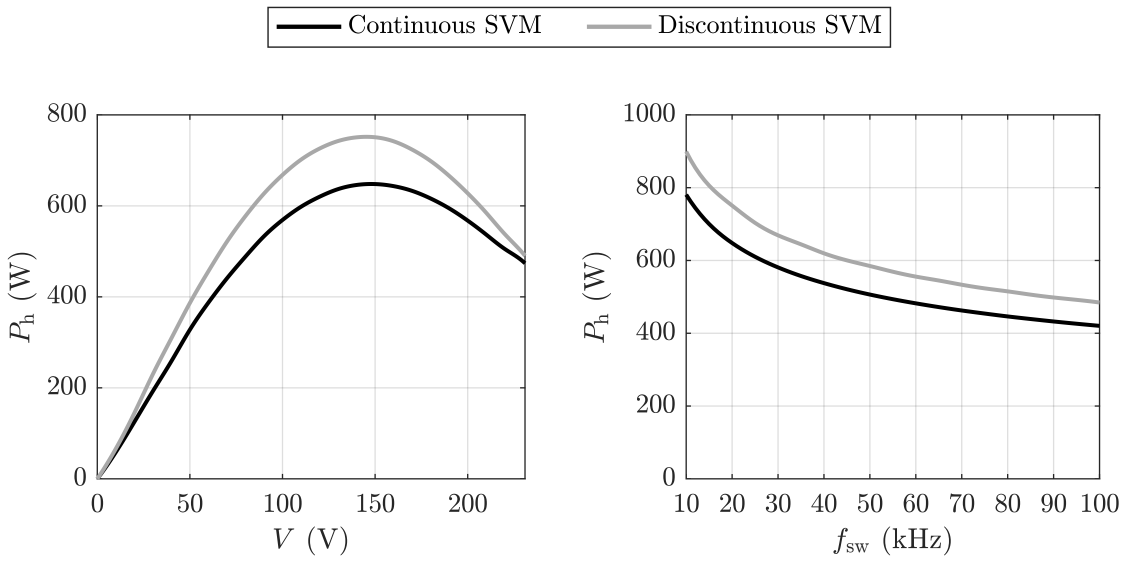

Figure 3.24: Motor harmonic loss dependence on V (left) and f_{sw} (right) for $V = 150$ V and $f_{sw} = 20$ kHz.

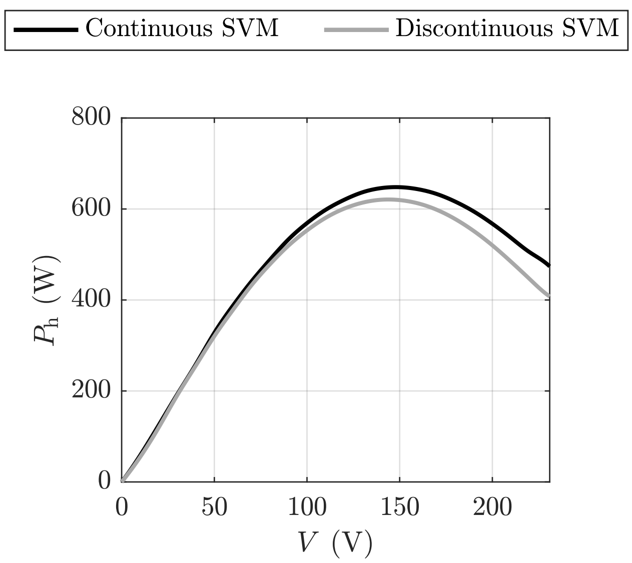

Figure 3.25: Motor harmonic loss dependence on V. Comparison between 7-segment SVM at $f_{sw} = 20$ kHz and 5-segment SVM at $f_{sw} = 40$ kHz.

7-segment one, a comparison between the two techniques with an adjusted f_{sw} value is provided in figure 3.25. The results show that the discontinuous modulation technique with optimal clamping has a better behaviour over the full voltage range. This means that, for the considered motor, there is no advantage in adopting a continuous modulation strategy. However, this conclusions is only valid for this specific situation. A different loss factor curve can yield other results and usually no clear winner can be identified, at least not over the full voltage range.

It is important to note that the loss factor curve, while fairly depending on the specific motor design, can drastically change between motor topologies (i.e. IM,

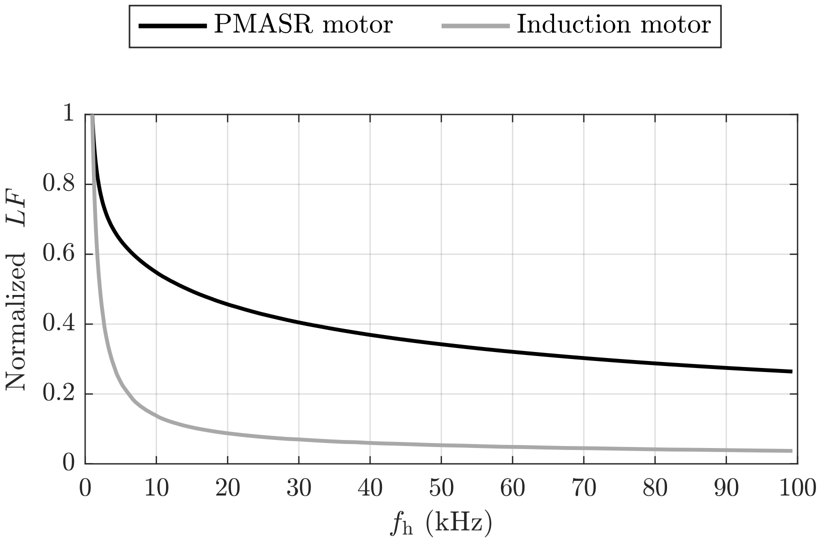

Figure 3.26: Comparison between loss factor curves of two different machines, normalized at 1 kHz.

SPM, IPM, etc.). Figure 3.26 provides a comparison between the loss factor curves belonging to the adopted PMASR motor and to an induction machine of similar size. The loss factors have been normalized in respect to their value at 1 kHz in order to compare the relative behaviour of the two machines. It is evident that the major part of the induction motor harmonic losses drops before reaching the 10 kHz frequency value. This is due to the IM rotor cage, which causes the machine to behave as a transformer with a short circuited secondary winding for high frequency harmonics. This phenomenon rapidly prevents the harmonic flux to penetrate the rotor, thus leaving only the stator core iron loss contribution. In this case there is realistically little to no advantage in increasing the switching frequency higher than $\sim$ 10 kHz, since the loss factor curve shows a flat behaviour. In comparison, the PMASR motor still shows a fair loss decline in the whole reported frequency range, therefore increasing the inverter switching frequency beyond 10 kHz can still prove to be advantageous.

Chapter 4

Vehicle Model

Since both the inverter design and the system-level optimization procedure strongly depend on the specific application, a suitable vehicle model must be developed and a set of target specifications must be identified. The vehicle performance requirements allow to determine the necessary motor overload torque in transient operation, thus establishing the minimum possible current rating of the traction inverter. Moreover, the dynamical simulation of the vehicle along a meaningful standardized driving cycle allows to identify its most frequent operating conditions, in terms of speed and motive force. These conditions can be translated into the operating points of the electrical machine (i.e. n, T) and, once a motor control strategy is defined, of the power converter (i.e. V, I, φ). This knowledge is required since, as mentioned in chapter 2 and chapter 3, the drive train (i.e. motor and inverter) losses highly depend on the operating conditions. Therefore, identifying the most relevant application-specific operating points is the first necessary step to carry out of the system efficiency optimization procedure.

4.1 Vehicle Dynamics

The total resistance to vehicle motion is given by the sum of different components [46], which are schematically represented in figure 4.1:

- **aerodynamic drag** is caused by the viscous resistance of air:

$$F_{\mathrm{a}} = \frac{1}{2}\,\rho_{\mathrm{air}}\,C_{\mathrm{x}}\,A_{\mathrm{f}}\,u^2 \tag{4.1}$$

  Where $\rho_{\mathrm{air}} = 1.225\ \mathrm{kg/m^3}$ is the air density, C_{x} and A_{f} are respectively the drag coefficient and frontal area of the vehicle and u is the vehicle speed.

- **rolling resistance** is caused by the tire deformation on the road:

$$F_{\mathrm{r}} = C_{\mathrm{r}}\,M\,g\,\cos(\gamma) \tag{4.2}$$

  Where C_{r} is the rolling resistance coefficient, M the loaded vehicle mass, $g = 9.81\ \mathrm{m/s^2}$ the gravitational acceleration and γ the road grade angle.

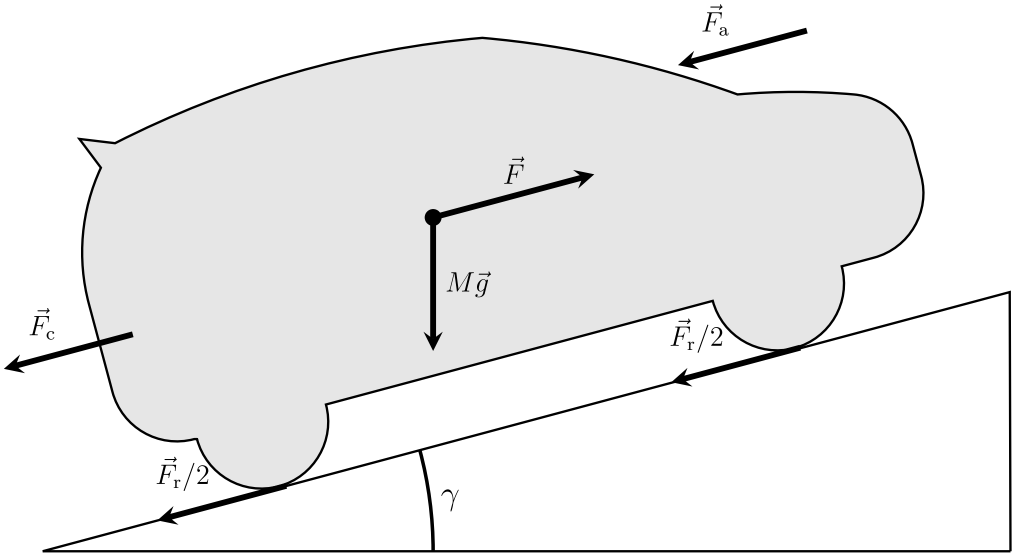

Figure 4.1: Schematic of the forces applied to a generic vehicle in motion.

► **climbing resistance** is due to the road slope:

$$F_{\mathrm{c}} = M\, g\, \sin(\gamma) \tag{4.3}$$

In order to overcome the total resistance to motion, a sufficient amount of motive force F has to be applied to the driving wheels. The vehicle acceleration is produced by the resulting net force:

$$a = \frac{F - F_a - F_r - F_c}{M_{\mathrm{eq}}} \tag{4.4}$$

Where

$$M_{\mathrm{eq}} = M + J_{\mathrm{w}}\, \frac{1}{R_{\mathrm{w}}^2} + J_{\mathrm{m}}\, \frac{\tau^2}{R_{\mathrm{w}}^2} \tag{4.5}$$

is the equivalent mass of the vehicle, accounting for the additional "rotational mass" of motor and wheels. J_{m} and J_{w} are the motor and wheels inertias respectively, R_{w} is the wheel radius and τ is the mechanical transmission ratio (i.e. motor-to-wheel speed ratio).

In order to analyse a real-case application, Model 3 from Tesla is chosen as reference vehicle throughout this dissertation. The main vehicle characteristics and performance specifics are reported in figure 4.2. Moreover, to effectively exploit the chosen PMASR electric motor over the full vehicle operating range, the mechanical transmission ratio is adjusted to match the maximum motor rotating speeds n_{max} with the vehicle top speed u_{max}:

$$\tau = \frac{2\pi}{60}\, \frac{n_{\mathrm{max}}}{u_{\mathrm{max}}/R_{\mathrm{w}}} \approx 9.0 \tag{4.6}$$

Property	Value
Empty vehicle mass	1610 kg
Loaded vehicle mass M	1810 kg
Wheel radius R_w	0.335 m
Wheels inertia J_w	5.20 kg m^2
Frontal area A_f	2.515 m^2
Drag coefficient C_x	0.23
Rolling coefficient C_r	0.015
Maximum speed u_max	210 km/h
Acceleration (0 - 100 km/h)	5.6 s

Figure 4.2: Tesla Model 3 picture (top) and main specifications (bottom).

4.2 Performance Constraints

The vehicle must satisfy different performance constraints, which can be subdivided in *transient* or *continuous* depending on their operational time requirement. Because of their temporary nature, transient constraints can be fulfilled by means of a temporary overload of the electrical machine, while continuous requirements must be ideally satisfied for an infinite amount of time (S1 operation) and must therefore comply with the rated continuous machine performance. As already mentioned in chapter 3, while the machine torque-speed characteristic in continuous operation only depends on the motor itself, the maximum transient overload torque capability is determined by the power converter current rating (see figure 3.10) and is thus a design variable. The main vehicle performance constraints are:

(1) maximum cruising speed on a flat road (*continuous*): $\gamma = 0$ °, $u = 210$ km/h

(2) low cruising speed on an uphill road (*continuous*): $\gamma = 15$ °, $u = 50$ km/h

(3) maximum slope at standstill (*transient*): $\gamma = 30$ °, $u = 0$ km/h

(4) acceleration time (*transient*): $t_{(0-100\,\mathrm{km/h})} = 5.6$ s

Specifics (1) and (2) are required in continuous operation and must thus be fulfilled by the motor S1 torque-speed curve. Since the electrical machine has already been

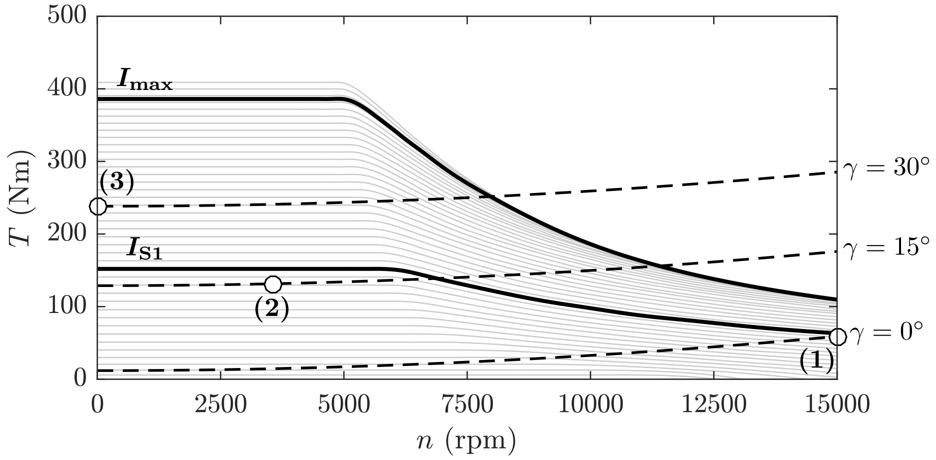

Figure 4.3: Torque-speed curves for different inverter current ratings $I = 20, 40, \ldots,$ 800 A (grey). Vehicle performance constraints (1), (2) and (3) are highlighted, together with the continuous motor torque capability (I_{S1}) and the inverter-enabled transient torque overload (I_{max}).

selected and the power converter cannot affect the continuous torque capability of the motor, the fulfillment of these requirements is only a matter of verification. When these constraints are not met, a machine characterized by a higher rated torque must be selected. Figure 4.3 shows that the continuous torque capability of the motor satisfies both requirements, as both (1) and (2) lie beneath the motor S1 torque-speed curve, proving that the electrical machine is correctly chosen for the application.

Specifics (3) and (4) are required in transient operation. In order to establish the necessary overload torque, the worst of the two conditions must be determined. Constraint (3) can be represented in the torque-speed plane (see figure 4.3), therefore the minimum acceptable torque-speed characteristic to satisfy it is directly determined. Constraint (4) must instead undergo some additional steps to be converted in a torque overload requirement. Given a certain torque-speed curve, the acceleration of the vehicle can be determined by means of equation (4.4), where $F_{\mathrm{c}} = 0$ since a flat road is considered. The vehicle speed time dependence during an acceleration run is obtained by integration:

$$u(t) = \int_0^t a(t)\, dt = \int_0^t \frac{F(t) - F_{\mathrm{a}}(t) - F_{\mathrm{r}}}{M_{\mathrm{eq}}}\, dt \tag{4.7}$$

Where:

$$F(t) = \frac{\tau}{R_{\mathrm{w}}}\, T(t) \tag{4.8}$$

Larger torque-speed curves, enabled by higher inverter current ratings, allow to decrease the vehicle 0 - 100 km/h acceleration time. This is illustrated in figure 4.4, where the vehicle acceleration runs (i.e. speed-time curves) related to different overload torque characteristics are displayed. Condition (4) is also highlighted. The minimum overload torque which satisfies both performance constraints (3) and (4) is therefore determined and is represented both in figures 4.3 and 4.4. This condition corresponds

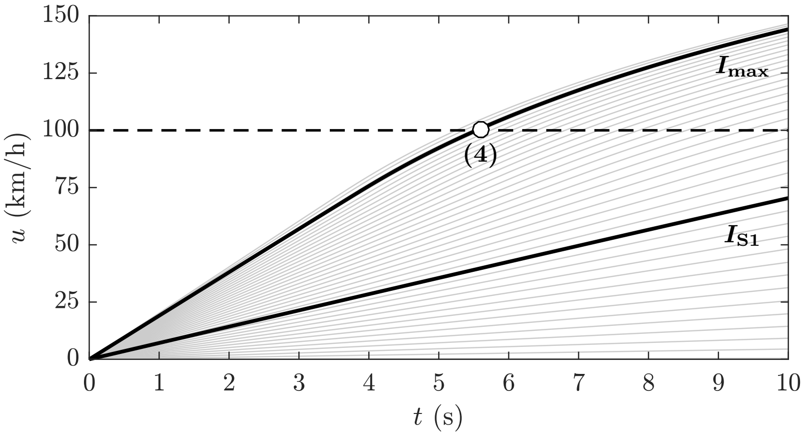

Figure 4.4: Speed-time curves during acceleration for different inverter current ratings $I = 20, 40, \ldots, 800$ A (grey). Vehicle performance constraint (4) is highlighted, together with the continuous motor torque capability (I_{S1}) and the inverter-enabled transient torque overload (I_{max}).

to an inverter peak current rating of:

$$I_{max} = 750 \text{ A} \tag{4.9}$$

It is worth noting that I_{max} directly determines the inverter size and cost, by requiring a minimum number of paralleled devices per switch in order to comply with the semiconductor junction temperature limits. This current value is therefore the main input specific for the inverter design.

4.3 Driving Cycle

The most relevant vehicle operating points must be identified in order to carry out the system efficiency optimization procedure, therefore a standardized driving cycle is selected for the task. Since the Worldwide harmonized Light vehicles Test Cycles (WLTC) represent the first attempt to reach a global harmonized standard for determining vehicle energy consumption, this driving cycle category is considered for the present evaluation. In particular, the drive train performance is assessed on the basis on the WLTC class 3 profile [47], as the selected vehicle has a power-to-weight ratio $PWr > 34$ kW/t. The WLTC driving cycle for a class 3 vehicle is made up by a 30 min (i.e. 1800 s) 23.3 km route, with a mixed combination of urban and highway driving. It is divided in four main parts with different speed levels (i.e. low, medium, high, and extra-high) for a total average speed of 53.5 km/h and a top speed of 131.3 km/h. Moreover, the driving cycle is discretized in 1 s intervals, for a total of 1800 points.

A dynamical simulation in a flat road condition is performed, adopting equations (4.1), (4.2) and (4.4) to estimate the required motive force to follow the driving cycle profile. The time dependence of the vehicle speed and motive force values are shown in figure 4.5. From these two quantities it is possible to determine the motor

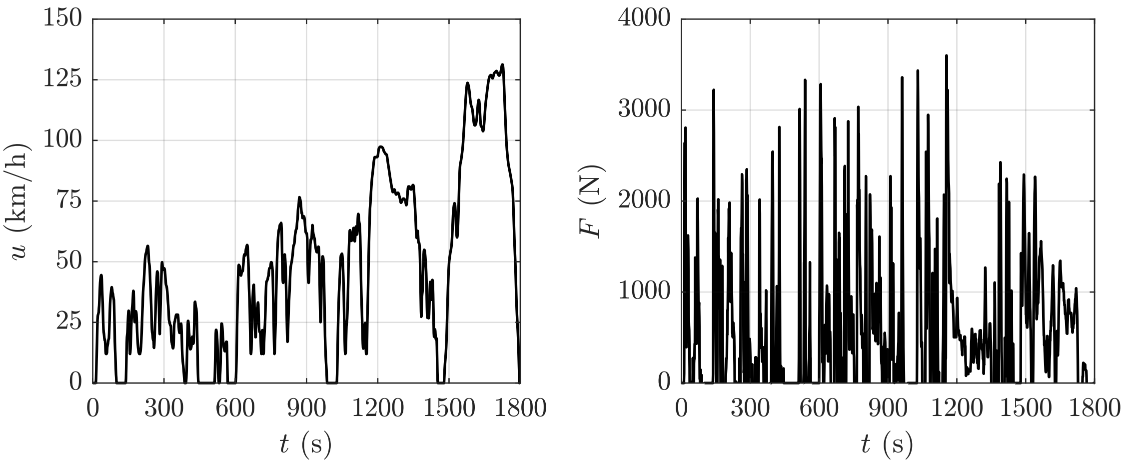

Figure 4.5: WLTC class 3 speed profile (left) and required motive force (right).

rotational speed n and the total torque required from the machine T:

$$\begin{cases} n = \tau \, \dfrac{60}{2\,\pi} \, \dfrac{u}{R_{\mathrm{w}}} \\ T = \dfrac{1}{\tau} \, \dfrac{F\,R_{\mathrm{w}}}{\eta_{\mathrm{g}}} \end{cases} \tag{4.10}$$

Where $\eta_{\mathrm{g}} = 0.95$ is the gearbox efficiency value assumed for the calculations. Figure 4.6 shows the operating points of the electrical machine in the (T, n) plane according to the WLTC class 3 profile. It can be observed that the motor works below the S1 torque-speed curve for the whole driving cycle and thus all of the operating points are achievable in continuous operation. This also means that high current values are never reached during normal operation, thus they have a rather small impact on the overall system energy consumption. It is worth mentioning that the regenerative braking

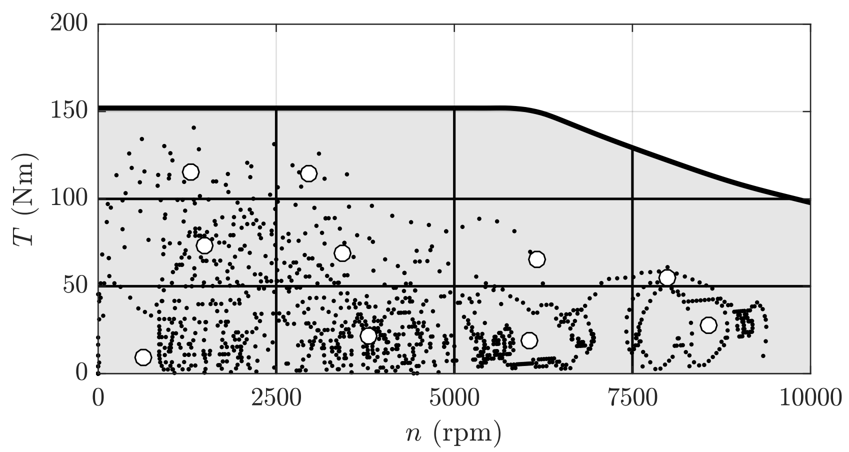

Figure 4.6: Motor operating points in the (T, n) plane according to the WLTC class 3 profile. The representative points are highlighted with a white circle.

contribution is here disregarded, since it complicates the overall system-efficiency evaluation, therefore only the motoring operation of the machine is considered in this study.

The extracted operating points represent the actual working conditions of the electric vehicle traction drive train, therefore they are at the core of the system efficiency optimization. However, an efficiency evaluation in every point belonging to the driving cycle would be extremely time-consuming and thus not suitable for a wide optimization procedure. In order to solve this issue, the technique proposed in [48] is here adopted. This method is based on the evaluation of a small number of equivalent driving cycle operating points, determined by the analysis of density patterns of the working points in the whole (T, n) plane. Moreover, a weight coefficient is assigned to each representative point, in order to provide a quantitative indication of the total time share of that specific equivalent operating condition.

Since no driving cycle point exceeds the motor continuous torque-speed characteristic and as all operating conditions reside below $n = 10\,000$ rpm, the (T, n) plane is subdivided in the 12 regular different sectors highlighted in figure 4.6. For each one of these areas, identified by an (i, j) pair, a representative equivalent torque $T_{\text{eq},ij}$ and speed $n_{\text{eq},ij}$ are determined in terms of geometrical center of gravity, together with a related weight coefficient $\mathrm{w}_{\text{eq},ij}$:

$$\begin{cases} T_{\text{eq},ij} = \sum_k T_{k,ij} \Big/ \nu_{ij} \\ n_{\text{eq},ij} = \sum_k n_{k,ij} \Big/ \nu_{ij} \\ \mathrm{w}_{\text{eq},ij} = \dfrac{\nu_{ij}}{\nu} \end{cases} \tag{4.11}$$

Where $T_{k,ij}$ and $n_{k,ij}$ are the k-th torque and speed values in each (i, j) operating area, while ν_{ij} and ν are the number of torque-speed points in the (i, j) area and in the total driving cycle, respectively. It is worth noticing that areas with a higher weight coefficient correspond to regions with higher clustering of working points and they are thus more important in the system efficiency optimization.

Table 4.1 illustrates the equivalent representative points in terms of $T_{\text{eq},ij}$, $n_{\text{eq},ij}$ and $\mathrm{w}_{\text{eq},ij}$ values. It is worth noting that 80.6% of the vehicle operation resides in the lower four sectors (i.e. low torque). This means that the drive train mostly operates at low load and thus at low current values. This is an extremely important information for the overall efficiency optimization procedure, as the most important efficiency gains must be obtained at low load.

It is important to mention that the (i, j) grid subdivision and thus the number of equivalent representative points result in a critical decision. While increasing the number of sectors yields a more precise operating point estimation, it comes with a higher computational time cost. The 12 region subdivision here presented is a fair compromise, since the total mechanical energy calculated along the actual driving cycle is 14.7 MJ, while the one computed by considering the weighted representative points is 14.4 MJ, yielding a total underestimation error of ~ 2 %, which may be considered negligible for the present purpose.

Table 4.1: Drive train equivalent representative points in terms of $T_{\mathrm{eq},ij}$ (top), $n_{\mathrm{eq},ij}$ (middle) and $\mathrm{w}_{\mathrm{eq},ij}$ (bottom).

	Speed (rpm)			
Torque (Nm)	0 - 2500	2500 - 5000	5000 - 7500	7500 - 10 000
0 - 50	9.5 Nm	21.9 Nm	19.1 Nm	27.6 Nm
50 - 100	73.1 Nm	68.7 Nm	65.4 Nm	54.8 Nm
100 - 150	115.8 Nm	114.1 Nm	-	-

	Speed (rpm)			
Torque (Nm)	0 - 2500	2500 - 5000	5000 - 7500	7500 - 10 000
0 - 50	633 rpm	3805 rpm	6055 rpm	8577 rpm
50 - 100	1501 rpm	3433 rpm	6157 rpm	7997 rpm
100 - 150	1297 rpm	2947 rpm	-	-

	Speed (rpm)			
Torque (Nm)	0 - 2500	2500 - 5000	5000 - 7500	7500 - 10 000
0 - 50	31.3 %	21.4 %	17.6 %	10.3 %
50 - 100	9.0 %	5.7 %	0.9 %	1.0 %
100 - 150	2.2 %	0.6 %	-	-

Once the application-specific representative points are available, it is possible to calculate an average efficiency value, weighted on the effective operating locations:

$$\eta = \frac{\sum_{ij} \mathrm{w}_{\mathrm{eq,ij}}\, P_{\mathrm{eq,ij}}}{\sum_{ij} \mathrm{w}_{\mathrm{eq,ij}}\, (P_{\mathrm{eq,ij}} + P_{\mathrm{loss,eq,ij}})} = 1 - \frac{\sum_{ij} \mathrm{w}_{\mathrm{eq,ij}}\, P_{\mathrm{loss,eq,ij}}}{\sum_{ij} \mathrm{w}_{\mathrm{eq,ij}}\, (P_{\mathrm{eq,ij}} + P_{\mathrm{loss,eq,ij}})} \tag{4.12}$$

where

$$P_{\mathrm{eq,ij}} = \frac{2\,\pi}{60}\, T_{\mathrm{eq},ij}\, n_{\mathrm{eq},ij} \tag{4.13}$$

is the representative (i, j) mechanical power at the machine shaft output, while $P_{\mathrm{loss,eq,ij}}$ is the drive train (i.e. inverter and motor) system loss in the same operating condition. It is important to note that the weighting process described in equation (4.12) takes into account the fact that the same efficiency figure at different mechanical power values yields a different amount of losses. It is shown that working points with a higher power value have greater importance in the overall efficiency weighting. This consideration is extremely important and wouldn't be taken into account by adopting a simple weighted sum of the individual (i, j) efficiencies.

Chapter 5

Model-Based Efficiency Optimization

Automotive components in general are subject to a strong pressure regarding cost, weight, volume and reliability, thus multi-objective optimization approaches are often needed during the system design process. However, it is normally not possible to enhance at the same time all of the aforementioned parameters. In power electronics an inherent trade-off between power density, efficiency and cost exists Therefore, once a set of requirements is provided, infinite optimal design solutions can be found. These solutions maximize one performance index at a time, forming a so-called Pareto front [49, 50].

Multi-objective optimization requires an accurate knowledge of the individual systems to be modeled and of the main performance interactions between them. This dissertation focuses on the drive train system efficiency maximization, thus other performance indices are outside the purpose of the work. Nevertheless, the trade-off between system efficiency and inverter semiconductor cost is presented in the following, in order to point out that the power converter losses cannot always be reduced without consequences on other indices.

The system efficiency optimization procedure here proposed regards both the power converter design and the motor control strategy. A model-based approach is adopted, meaning that the optimization algorithm is based on the models illustrated in the previous chapters. From the inverter design point of view, the aim is to establish the best combinations among the semiconductor device choice, the number of paralleled devices per switch, the adopted modulation technique and the operating switching frequency. From the control perspective, the goal is to derive a minimum system-loss strategy by mapping the speed-dependent optimal control trajectories on the motor dq current plane.

The main challenge of a system-level optimization process resides in correctly modeling the interactions between the system subcomponents, which are normally disregarded. Conventional loss minimization approaches optimize the efficiency of the individual devices without considering their interconnection inside the system. However, these procedures are unable to reach a global optimum, since they neglect those loss components which are generated from the mutual interaction of subsystems, such as the inverter-induced motor harmonic losses.

Table 5.1: Inverter and motor loss components dependence on operating conditions and design parameters.

	Operating Conditions			Design Parameters			
Loss Components	V	I	φ	f_{sw}	Device	N_{par}	Modulation
Conduction Losses (*Inverter*)	√	√	√	-	√	√	√
Switching Losses (*Inverter*)	-	√	√	√	√	√	√
Harmonic Losses (*Motor*)	√	-	√	√	-	-	√
Copper Losses (*Motor*)	-	√	-	-	-	-	-
Iron Losses (*Motor*)	√	√	√	-	-	-	-
Mechanical Losses (*Motor*)	-	-	-	-	-	-	-

The loss mechanisms of the power converter and the electrical machine have been respectively analysed and modeled in chapter 2 and chapter 3 and their dependence on the operating conditions and design parameters is summarized in table 5.1.

Loss models and representative system working points are now available, therefore it is possible to combine them and execute a model-based system-level optimization procedure, aimed at maximizing the overall vehicle drive train efficiency.

5.1 Optimal Switching Frequency

The switching frequency of the traction inverter must satisfy several constraints of different nature. A minimum value is set by either the audible noise emission or the control performance requirements, whichever is more strict. Moreover, since increasing the switching frequency yields a great benefit in reducing the common and differential mode filtering effort, high frequency values can substantially decrease the weight and cost of the power converter. However, these filter-related benefit considerations are outside the scope of this dissertation. As already pointed out, one of the main goals of this work is to find the switching frequency value which minimizes the total system losses.

When increasing the switching frequency, the inverter switching losses increase, whereas the time-harmonic losses induced in the electrical machine are decreased. Therefore, a minimum system loss switching frequency value exists and must be identified. However, the actual f_{sw} value must comply with both a lower and an upper boundaries. In order to satisfy the machine control performance requirement, the minimum inverter switching frequency has been set to 10 kHz, as the maximum fundamental frequency of the selected motor is 1250 Hz at 15 000 rpm. Nevertheless, there is ideally no upper switching frequency limit if the semiconductor devices are switched with a sufficiently low dv/dt to comply with the machine stator winding isolation. This limit is set in practice by the increasing semiconductor losses, which require a higher cooling effort and thus negatively impact the weight, volume and cost of the power converter by the need of a larger heat sink. Therefore, a reasonable maximum value of 100 kHz has been selected, in order to avoid evaluating unrealistic f_{sw} values. The only system loss mechanisms which depend on the switching frequency are the inverter switching losses and the inverter-induced motor harmonic losses. Both loss phenomena also highly depend on the electrical operating conditions.

Inverter switching losses scale linearly with switching frequency, as illustrated in chapter 2, and overall depend on the following operating conditions:

$$P_{\text{sw}} = f(I, \varphi) \approx f(I) \tag{5.1}$$

In case the 7-segment SVM modulation technique is adopted, the switching losses do not depend on the power factor angle. The discontinuous modulation strategy generates instead φ-dependent switching losses, as shown in figure 2.22. However, this dependence can be neglected if a PMASR machine is considered, since φ lies in a $\pm 30°$ range for most of the operating time.

Motor harmonic losses decrease with increasing switching frequency values, as shown in chapter 3, and have the following operating point dependence:

$$P_{\text{harm}} = f(V, \varphi) \approx f(V) \tag{5.2}$$

The continuous modulation strategy generates an output voltage waveform which is independent on the power factor angle, therefore its induced harmonic losses do not change. Moreover, while the output voltage spectrum of the optimal-clamping 5-segment modulation technique changes with φ, this dependence does not have a significant effect on the voltage HDF and thus neither on the machine harmonic losses.

Since the inverter switching losses depend on the load current I and the machine harmonic losses depend on the load voltage V, different optimal switching frequency values are obtained for different (V, I) operating conditions. Figure 5.1 shows the switching and harmonic loss variation with f_{sw} in the defined 10 - 100 kHz range, for two different (V, I) pairs. The optimal switching frequency f^*_{sw} is identified and highlighted in both cases. It can be observed that this value can drastically change for different (V, I) operating pairs. When the load current is high and the load voltage is low (e.g. vehicle accelerating at low speed or riding uphill), the inverter switching losses prevail and reduce the optimal switching frequency value. However, when the load current is low and the load voltage is high (e.g. vehicle cruising at high speed on a flat road), the motor harmonic losses become dominant and shift the optimal switching frequency to higher values.

It is worth noting that this loss trade-off also depends on the inverter design, being the combination of the adopted semiconductor device, the number of devices in parallel per switch and the selected modulation technique. A comprehensive comparison of the optimal switching frequency as a function of the operating condition (V, I) and the inverter design combination is provided in figure 5.2. Other than pointing out the loss trade-off dependence on the load voltage and current values, this figure

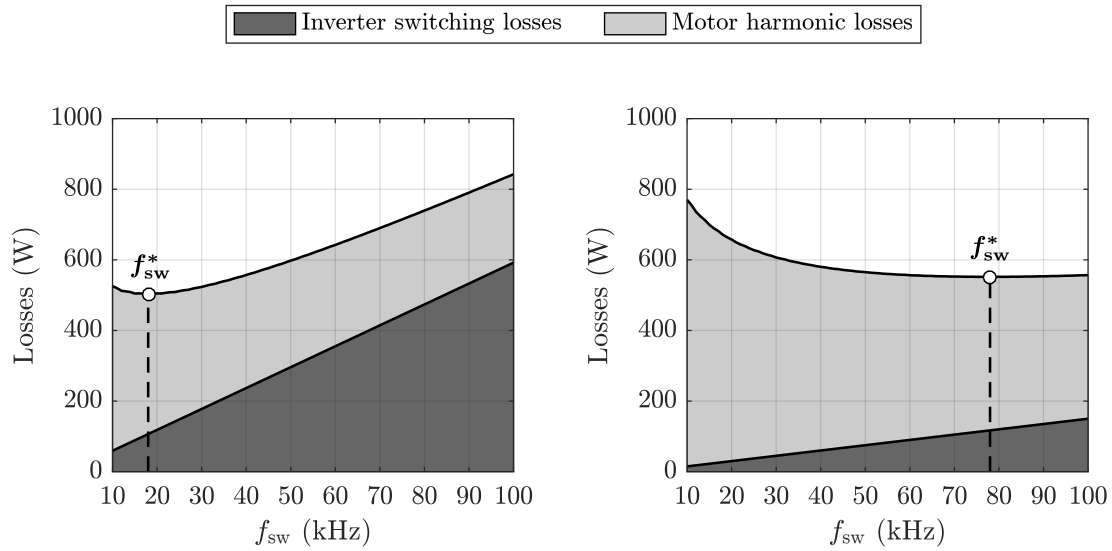

Figure 5.1: Inverter switching loss and motor harmonic loss behaviour as a function of switching frequency in the following operating conditions: $V = 50$ V, $I = 400$ A (left) and $V = 200$ V, $I = 100$ A (right). 12 paralleled ROHM SCT3022AL SiC MOSFETs are considered and the proposed 5-segment SVM modulation strategy is adopted.

highlights the strong impact of choosing a specific semiconductor device or changing the modulation technique. It can be observed that both choices of adopting a SiC MOSFET instead of a conventional IGBT and selecting a discontinuous modulation strategy in spite of a standard continuous one push the optimal switching frequency to higher values. The SiC MOSFET device generates lower switching losses compared to the IGBT, while yielding exactly the same output voltage spectrum. This increases the relative importance of harmonic losses, therefore a higher switching frequency becomes beneficial to reduce them. The 5-segment SVM strategy, compared to the 7-segment one, decreases the number of switching events per period, while increasing the output voltage distortion, as described in chapter 2. Both of these phenomena move the best trade-off switching frequency to higher values.

It is worth noting that, while an ideal optimal efficiency control strategy should adapt the switching frequency value to the operating point, in order to minimize the total losses in every condition, this represents an issue in common practice, since the power converter filtering systems are usually designed and optimized for a single switching frequency value. For this reason, a unique switching frequency must be selected, thus a global optimum must be identified. This value depends on the specific application and can be found by weighting the inverter switching losses and motor harmonic losses on the most relevant working points during operation. The extraction of the system-level optimal switching frequency value will be shown in the following.

Although a specific electrical machine has been selected for the present investigation, together with a precise application, the aforementioned approach can identify the optimal switching frequency of an arbitrary inverter and motor combination with a generic operating profile.

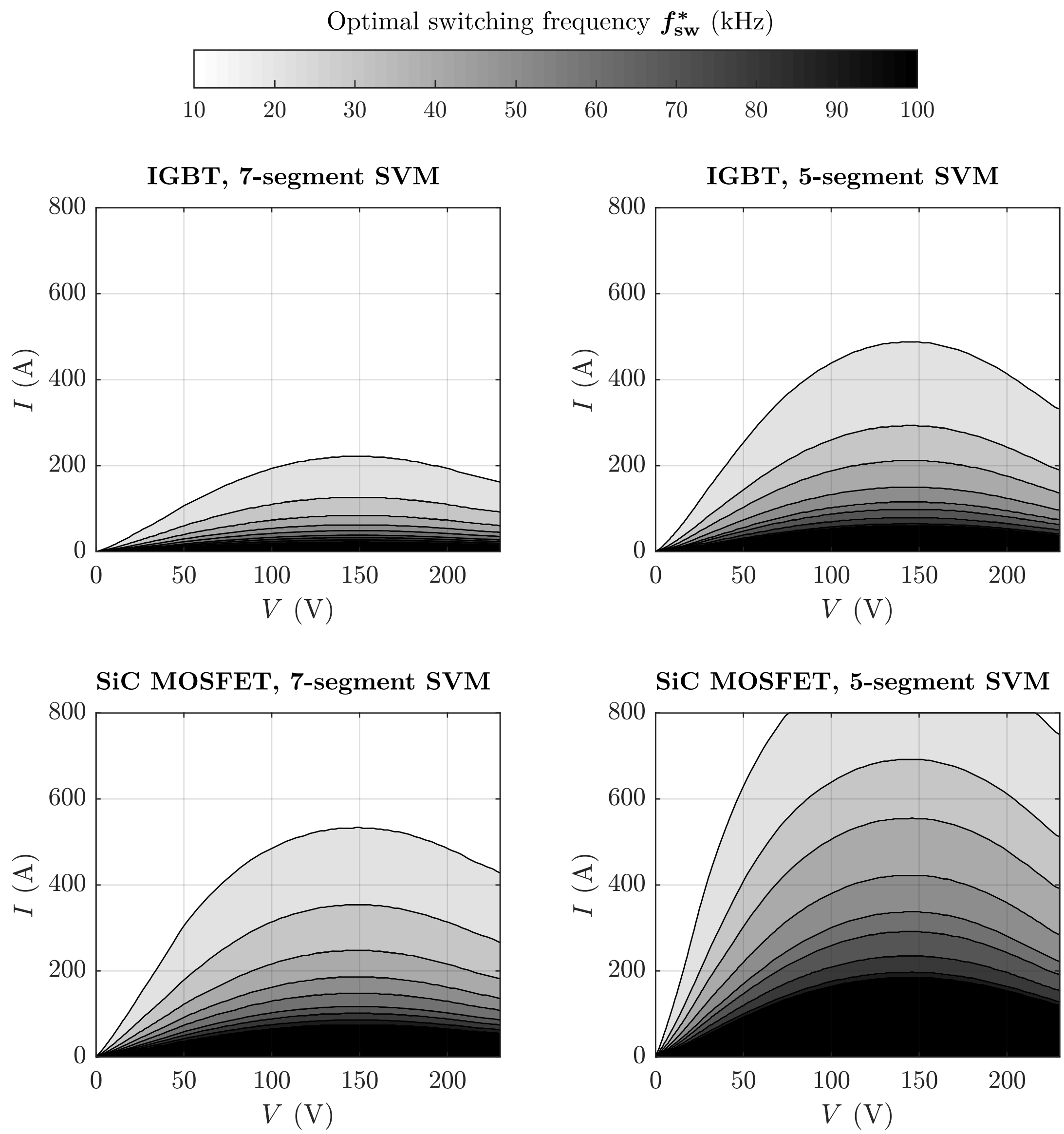

Figure 5.2: Optimal switching frequency maps for different V and I values and inverter designs. 12 paralleled semiconductor devices are considered in all cases.

5.2 Optimal Motor Control Strategy

Several minimum-loss motor control strategies have been proposed in literature. Early optimal control schemes have been developed for induction machines, because of their wide industrial adoption [51–56]. Nevertheless, a great interest in loss minimization control of permanent magnet machines has emerged more recently, due to their higher efficiency and torque performance [57–64]. Most of the research has been focused on accurately modeling the loss mechanisms of the motor, without taking into account its driving inverter in the optimal control strategy. This is because the electrical machine, due to its mechanical nature, normally shows the highest losses and dominates the drive efficiency, allowing to disregard the semiconductor losses. However, due to the continued historical increase in machine efficiencies (i.e. with the adoption of new designs and materials), the inverter contribution to the total drive loss can no longer be neglected. This is particularly true for high-power drives, as in our case, since electrical machines become more efficient with increasing size. Additional studies have therefore been developed to take into account the whole drive efficiency in the optimal working point calculation, modeling both inverter and motor losses [3,65–70]. However, the adopted loss models are normally analytical and thus extremely simplified.

Model-based energy-saving controllers rely on accurate models of the loss mechanisms of the drive system. These controllers estimate or measure the machine working point and directly calculate the optimal reference for the controlled variables, exploiting the motor and inverter models derived off-line. The loss models developed in this dissertation are based on manufacturer data, FEM analysis and measurements when possible. Moreover, the additional inverter-induced motor harmonic loss component has been derived and implemented. Therefore, a more accurate and comprehensive estimation of the optimal efficiency working point can be provided compared to conventional approaches. It is worth noting that the implemented models are based on steady-state assumptions, therefore the found optimal solution is not valid in transient operation. Nevertheless, in electric vehicle applications the operating point dynamics follow the vehicle mechanical transients, which are much slower compared to electrical ones. Therefore, the energy-saving controller steady-state assumption may be considered appropriate.

The machine torque reference can be obtained by means of an infinite number of (i_d, i_q) combinations, therefore a degree of freedom exists from the control point of view and should ideally be exploited to minimize the system losses. The most frequently adopted control technique in industry is the so called maximum-torque-per-ampere (MTPA). This strategy identifies the control trajectory which minimizes the current value for a given torque reference. The MTPA implementation only requires the knowledge of the machine torque map as a function of the direct and quadrature axis currents (see figure 3.8), since this information is sufficient to identify, for a given torque value, the (i_d, i_q) pair which minimizes the total current. By minimizing the required current, the MTPA strategy minimizes the motor copper losses, while also reducing the inverter conduction and switching losses. However, this technique does not take into account the machine iron loss component, which can become significant in high speed operation. Other control techniques have therefore been introduced, in order to also consider the machine core losses to find the optimal reference, and are here referred to as maximum-torque-per-loss (MTPL) strategies. Once both motor copper and iron loss models are available, the minimum machine loss point can be identified in the (i_d, i_q) plane and the MTPL trajectory can be derived. Compared to MTPA, this strategy tries to reduce the machine flux with increasing speed, thus rotating counterclockwise the current vector towards the $-d$ direction. This effect is particularly evident at high speed and low torque values, where the iron loss dominates over the copper loss.

While the aforementioned MTPL technique only takes into account the machine fundamental loss components, a maximum efficiency control strategy taking into account inverter, motor and mutual-induced losses is here described. Due to the availability of the previously derived loss models, the control degree of freedom in selecting the (i_d, i_q) pair for a given torque reference can be exploited to minimize the complete drive train system losses. Therefore, the goal of the here presented MTPL strategy is to identify the system loss minimizing dq current references for each given torque value.

Motor fundamental losses represent the major loss component of the total drive system and they depend on three main variables. The choice of these variables is not unique: for instance both (i_d, i_q, n) and (i_d, T, n) combinations are sufficient to identify the motor fundamental losses, but other combinations may be adopted. However, once the mechanical operating point (T, n) is fixed, only one variable can be freely chosen and must therefore be exploited to enable the optimal control strategy. Moreover, the (i_d, i_q, n) motor operating point can directly be translated into the load condition (V, I, φ) seen by the inverter, by means of the machine electrical equation (3.5):

$$\begin{cases} V = f(i_d, i_q, n) \\ I = f(i_d, i_q) \\ \varphi = f(i_d, i_q, n) \end{cases} \tag{5.3}$$

Changing the motor operating point to minimize the fundamental losses yields a considerable variation of the machine terminal voltage, current and power factor angle, thus having a substantial impact on both the inverter semiconductor losses and the inverter-induced machine time-harmonic losses. Equation (5.3) suggests that every system loss mechanism derived in chapter 2 and chapter 3 can be expressed in terms of (i_d, i_q, n). Therefore, by adding together all of the loss components, the minimum system loss control strategy can be derived. Unfortunately, there is no suitable analytical solution to this optimization problem, however the optimal reference values can be identified off-line and implemented in the control by means of look-up tables (LUTs).

Figure 5.3 shows the extracted (i_d, i_q) control trajectories for different n values, considering three different control strategies: the MTPA, the MTPL which minimizes the motor fundamental losses and the proposed system-level MTPL. It is worth mentioning that, for this comparison, an inverter characterized by 12 paralleled Infineon AIKW50N65DF5 IGBTs per switch, controlled with 7-segment SVM at 10 kHz has been considered. Moreover, the peak current limit of 750 A derived in chapter 4 is adopted.

When the machine is at standstill, the three control trajectories coincide. This is because the machine supply frequency is zero, therefore no iron losses are generated and a small feeding voltage is required from the inverter, making harmonic losses negligible. The remaining loss components (i.e. copper, conduction and switching) dominate the system losses, thus the MTPA strategy yields at the same time the highest motor and system efficiency.

When increasing the machine speed, the three trajectories depart one from the other, mostly because motor iron losses start rising. The machine-based MTPL reduces flux while accepting higher current values, in order to follow the best iron/copper loss trade-off. This results in a control trajectory shifted towards the $-d$ axis compared to

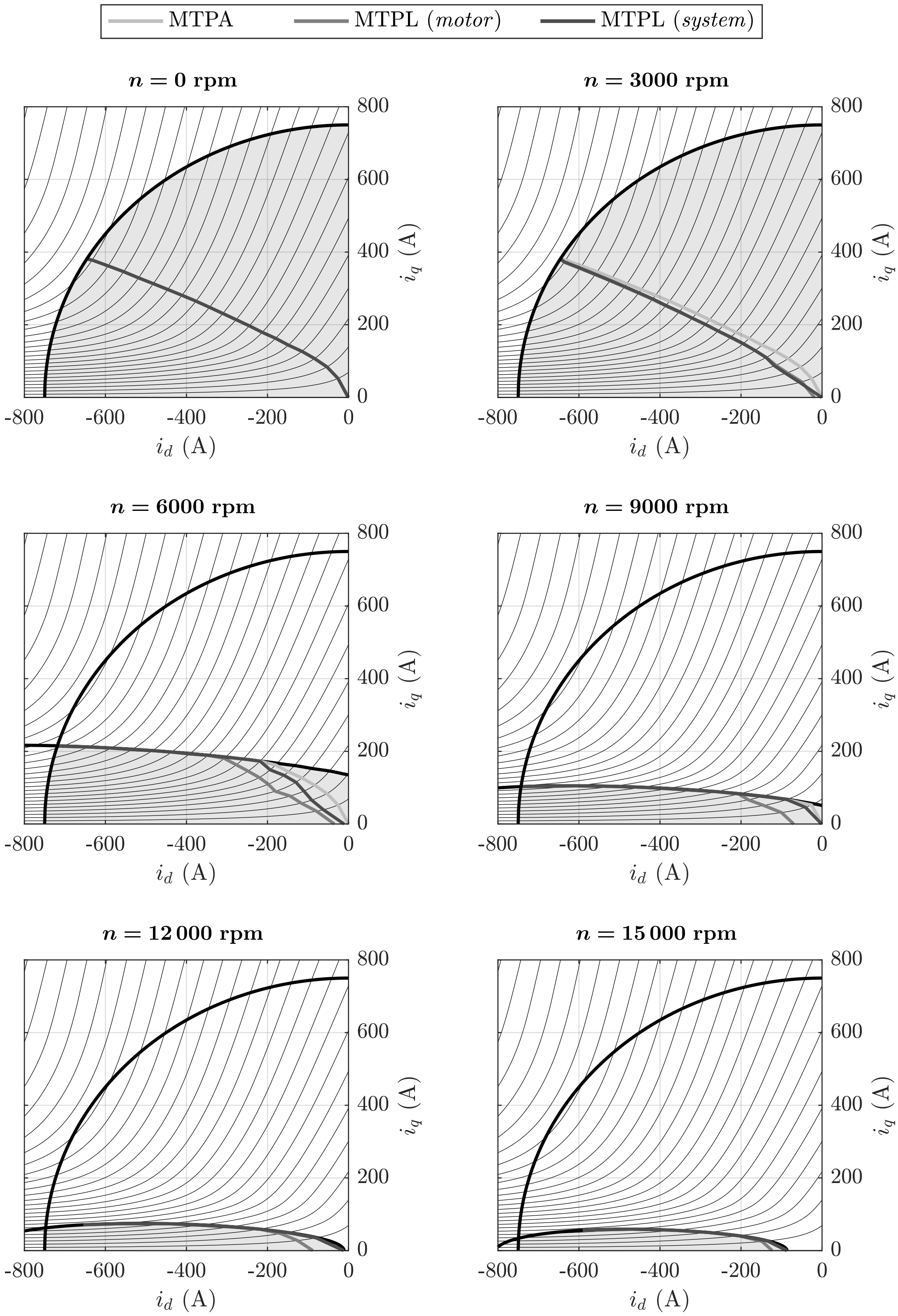

Figure 5.3: Comparison between MTPA, motor MTPL and system MTPL control strategies for different speed values. An inverter with 12 paralleled Infineon AIKW50N65DF5 IGBTs per switch, controlled with 7-segment SVM at 10 kHz has been considered. Torque iso-level curves and feasible operating region ($V_{\text{lim}} = 231$ V, $I_{\text{lim}} = 750$ A) are also depicted.

the MTPA, as the current vector must be rotated counterclockwise to limit the machine flux. The system-based MTPL lies between the two aforementioned trajectories. This is because the proposed strategy takes into account also semiconductor and harmonic losses, compared to the previous MTPL. While harmonic losses are quite small compared to the other system loss components and do not influence considerably the optimal trajectory, the inverter semiconductor losses can be relevant and, due to their current dependence, push the control trajectory towards the MTPA.

Finally, at very high speed (i.e. in sustained flux-weakening), the three trajectories return similar, since they are bounded for the most part by the voltage limit.

With the availability of the control trajectories as a function of (i_d, i_q, n) it is now possible to uniquely relate the vehicle working points on the (T, n) plane with the inverter operating conditions (V, I, φ) and the individual drive train loss components. As an example, figure 5.4 shows the derived loss maps as a function of the generic (T, n) working point, extracted with the proposed system-level MTPL strategy and the same inverter design as before. Different loss components may dominate the total system losses depending on the operating point. It can be observed that conduction, switching and copper losses directly depend on torque and they roughly follow the constant current characteristics. Therefore, at high torque values, these loss components are totally dominant. However, at low torque and sufficiently high speed, both iron and harmonic losses become relevant, due to their rough load independence. It is important to note that the vehicle operation during the driving cycle mostly resides in the low torque region (see figure 4.6), therefore it is very important to take iron and harmonic losses into account during the optimization procedure. Finally, mechanical losses do not depend on the control strategy, as they only increase with speed, and are not subject to optimization. However, their contribution is considered in order to estimate realistic efficiency values for the complete drive train.

The presented minimum system-loss control strategy may be implemented with a simple current control scheme, depicted in figure 5.5. The torque reference T^*, together with the speed information ω (measured or estimated), are fed into a 3D-LUT that stores the torque-to-current optimal relationships for different speed values. Since the optimal control trajectories are derived off-line, there is no need for demanding real-time calculations, as all the relevant information is stored in the LUT itself. Moreover, since a constant DC-link voltage is considered, this LUT also contains the information about the speed-related voltage limit, as it already affects the shape of the extracted control trajectories. The output of the LUT consists in the i_d^* and i_q^* reference values, which then enter the current controller loop. This block also receives the measured current information, in order to effectively close a feedback control loop. Finally, the resulting output voltage references v_d^* and v_q^* are processed by the SVM modulator, which directly controls the inverter switching behaviour by means of PWM signals. Therefore, the PMASR machine is controlled in a conventional way. The only control implementation difference compared to a regular MTPA strategy resides in the content of the LUT.

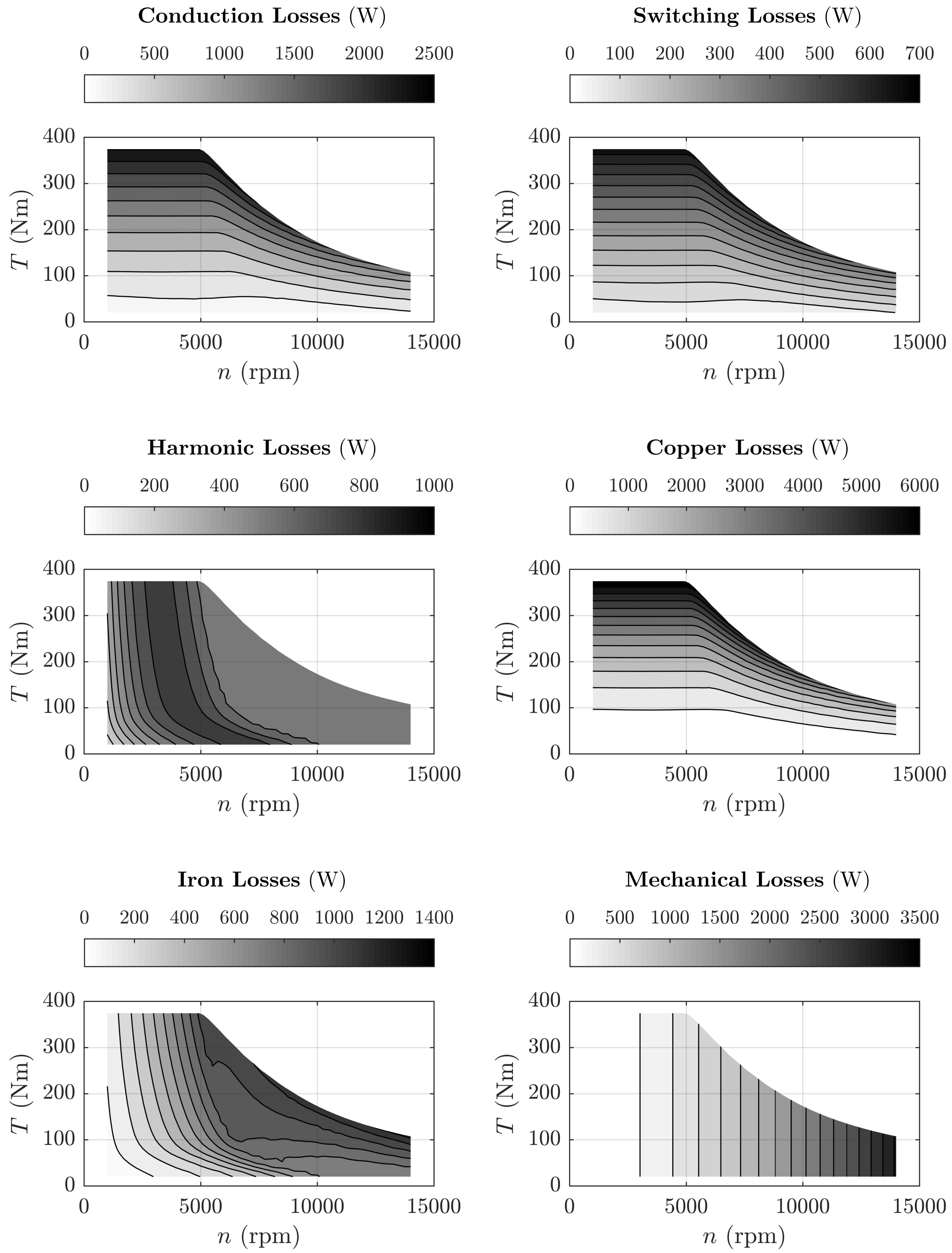

Figure 5.4: Individual loss component maps as a function of the (T, n) working point. The system-level MTPL has been adopted, together with a 12 paralleled Infineon AIKW50N65DF5 IGBTs per switch inverter design, controlled with 7-segment SVM at 10 kHz.

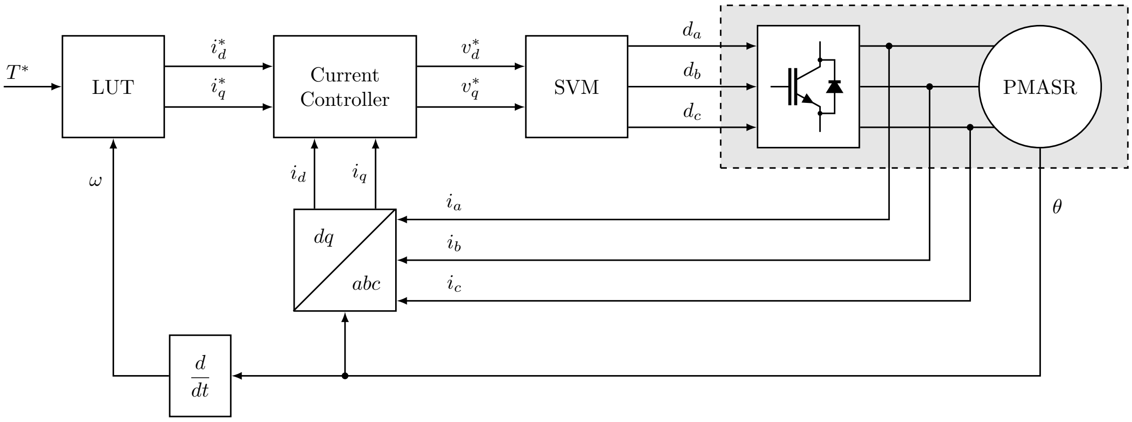

Figure 5.5: Schematic of the control structure.

5.3 System-Level Optimization

Now that either the loss models and the machine control strategies are available, the system-level efficiency optimization procedure can be performed. All of the systems must be cleverly interconnected and a limited set of design variables must be selected, in order to minimize the computational effort and reduce the simulation time.

The design space (i.e. set of variables) chosen for the presented optimization procedure is illustrated in table 5.2. The inverter rated current $I_{\max}$ represents the current value that the semiconductor devices must withstand during the machine maximum torque overload and has been derived in chapter 4. This current, together with the heat sink parameters, determines the minimum number of paralleled devices per switch for a given switching frequency, so that the maximum device junction temperature (i.e. 175 °C) is not exceeded. The inverter switching frequency is varied in a 10 - 100 kHz range for the previously mentioned reasons, while the maximum number of semiconductors devices in parallel is limited to 50. This value is unrealistically high, however it is needed to show the system efficiency saturation towards high N_{par} values. Moreover, both semiconductor devices (i.e. IGBT and SiC MOSFET) and both modulation techniques (i.e. 7-segment and 5-segment SVM) are included in the analysis. Finally, also different motor control strategies are taken into account, since they influence the system operating point and have therefore a substantial impact on the overall efficiency. The conventional MTPA is compared to the proposed system-level MTPL.

The main goal of the optimization procedure is to find the optimal inverter switching frequency which maximizes the system weighted efficiency for every design combination. It is worth reminding that the system losses are weighted on the most relevant vehicle working points in the WLTC driving cycle, derived in chapter 4. The other major aim is to analyse and quantify the contribution of each design variable to the overall efficiency enhancement.

Figure 5.6 depicts the flow chart of the optimization procedure. This process generates converter designs by means of successive combinations and evaluates their overall loss performance. Both system weighted losses and efficiency are stored in a

Table 5.2: Design variables for the optimization procedure.

Design Variables	**Values**
Rated peak current $I_{\max}$	750 A
Switching frequency f_{sw}	10 ... 100 kHz
Semiconductor device	IGBT, SiC MOSFET
Number of devices in parallel N_{par}	1 ... 50
Modulation technique (SVM)	7-segment, 5-segment
Control strategy	MTPA, MTPL

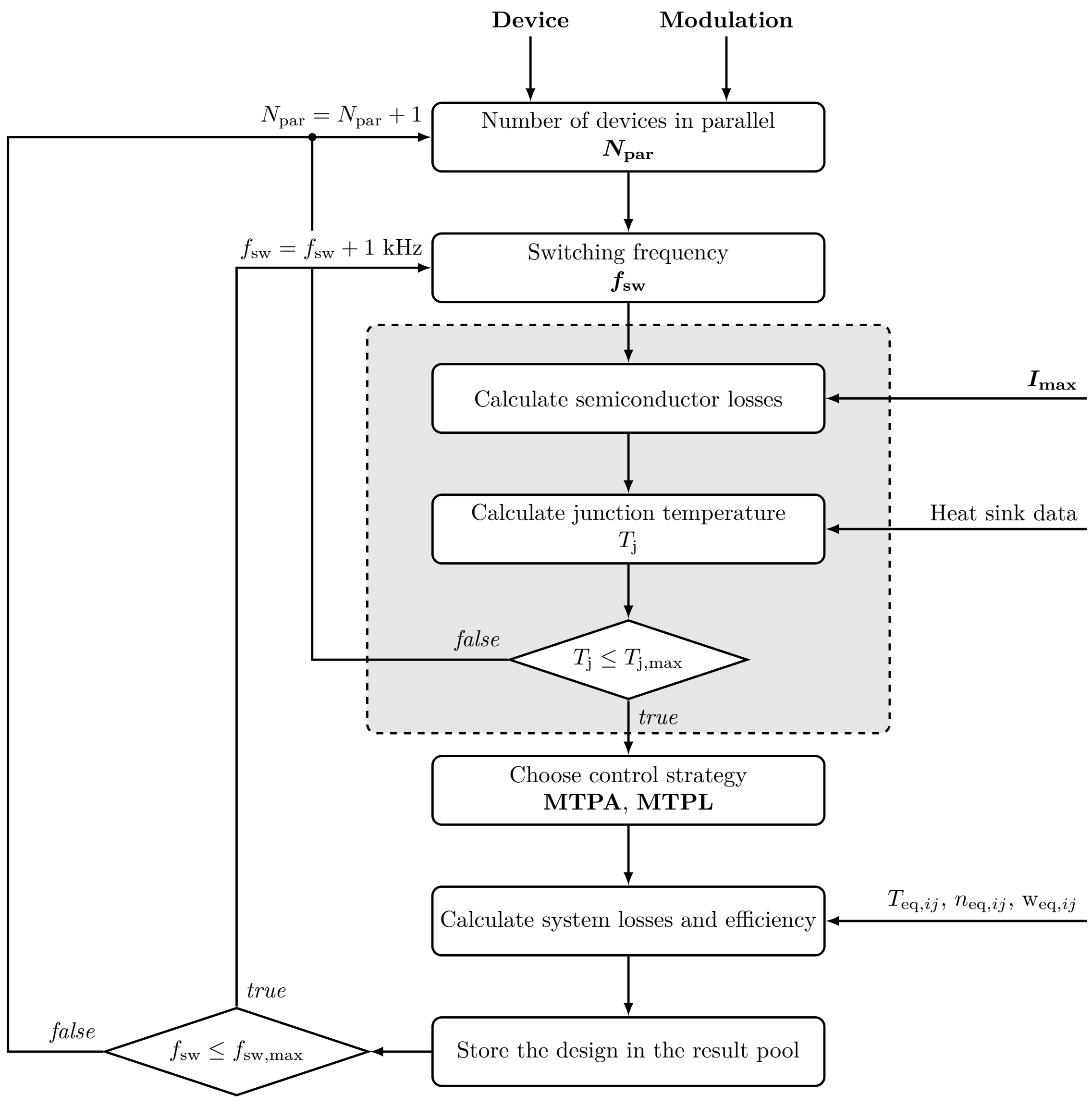

Figure 5.6: Flow chart of the system-level efficiency optimization procedure.

pool of results for each investigated design. This optimization method belongs to the "brute-force" type, since all the existing design variable combinations are evaluated. Due to the system non-linearities and overall complexity it is not possible to apply conventional optimization methods, therefore a large number of designs must be considered. This is the main argument behind why the design parameter pool must be limited to a reasonable amount of values, as the computational effort would otherwise increase dramatically. Moreover, verification algorithms with the aim of finding the not suitable designs must be integrated wherever possible, in order to discard these designs at an early stage of the optimization procedure.

In a first step, the main inverter design parameters are selected. Once the semiconductor device type and the modulation technique are chosen, the highest level iterative loop is entered, where the number of parallel devices per switch N_{par} is increased at each iteration. A further inner loop selects one by one all of the switching frequency values in the predefined range. Ahead of starting the system loss evaluation for the selected design variable combination, the semiconductor device junction temperature is verified, in order to early discard the designs which do not comply with the $T_{\mathrm{j,max}}$ constraint. The device conduction and switching losses are calculated in the worst case condition (i.e. at I_{max}) and the semiconductor junction temperature is evaluated by means of the thermal model presented in chapter 2. If the selected design does not comply with the semiconductor junction temperature limit it is discarded and the switching frequency loop is interrupted, since higher f_{sw} values would only further increase the semiconductor losses and thus the junction temperature. Once the thermal verification in completed, the design is passed to the control strategy selector. Both MTPA and MTPL are evaluated and the overall system losses and efficiency are calculated by means of the weighted driving cycle points extracted in chapter 4. These values are stored in the design result pool and the calculation procedure is repeated for a higher switching frequency value or an increased number of paralleled devices. The overall procedure is done for both semiconductor device types (i.e. IGBT and SiC MOSFET) and both modulation techniques (i.e. 7-segment and 5-segment SVM).

The results of the system-level efficiency optimization procedure are shown in figure 5.7, where the weighted system efficiency for every evaluated design combination has been plotted. Changing the switching frequency for a given set of design variables yields different system losses and thus a cloud of points is generated. The set of maximum efficiency values for an increasing inverter cost (which is proportional to N_{par}) represents a so-called Pareto front in the (η - €) performance space. These curves facilitate the identification of optimal converter designs, as they reveal the best possible trade-off between efficiency and cost. Moreover, each figure shows the design result pool for both MTPA and MTPL control strategies, so that the superior performance of the maximum system-efficiency strategy is highlighted.

According to the results, SiC MOSFETs provide a considerably higher efficiency compared to IGBTs. Even by increasing the number of devices in parallel, the optimal IGBT designs cannot reach the loss performance provided by optimal SiC MOSFET designs with lower N_{par} values. This result was certainly expected, due to the technology advantage of SiC devices, however the performance difference between

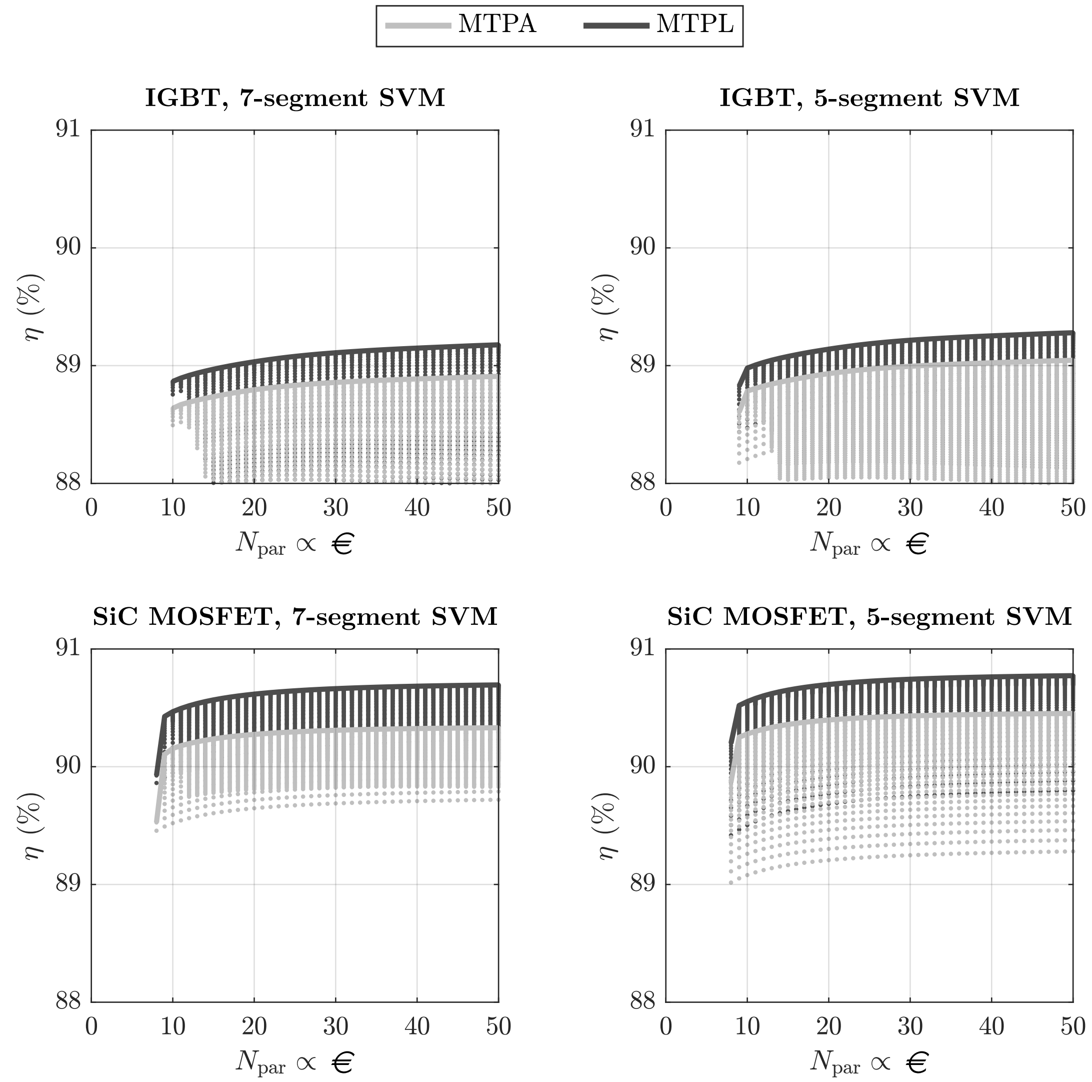

Figure 5.7: (η - €) Pareto fronts with different combinations of semiconductor device type, modulation technique and control strategy. All of the f_{sw} acceptable design combinations are also displayed (dots).

the two technologies is here assessed and quantified. It is worth mentioning that, due to the great price disparity between the IGBT and the SiC MOSFET power devices (i.e. a factor of ~ 9), the Pareto fronts related to different semiconductor technologies are not straightforward to compare. SiC devices are still prohibitively expensive compared to conventional Si components, however it is expected for their purchase cost to drop considerably in the near future, due to a higher market adoption. Since accurate cost considerations are outside the goal of this thesis, a pure performance approach is here adopted. The number of paralleled device is directly related to the power converter volume. Moreover, due to their TO-247 packaging format, the physical dimensions of the two devices are the same. Therefore, the same inverter volume can be expected for a specific number of paralleled devices per switch, independently on the considered semiconductor technology.

From figure 5.7 it is evident that a minimum number of devices in parallel is required in order to comply with the semiconductor thermal limits. For the present application (i.e. worst case operating condition of 750 A), the minimum N_{par} value varies between 8 and 10 depending on the selected power device, which mainly determines the semiconductor losses and the overall thermal resistance, and the adopted modulation technique, which has a substantial influence on the switching losses.

Even if not directly visible from the Pareto fronts, the optimal switching frequency is highly dependent on the specific design combination. However, only those design variables that actually impact switching and harmonic losses can influence the switching frequency optimum. Therefore, the device choice and the modulation technique are the most influencing factors, while N_{par} and the motor control strategy do not have a visible effect. In particular, even though increasing the number of parallel devices per switch yields lower conduction losses, it doesn't have a relevant impact on switching losses, since the device loss characteristics become almost linear towards low current values (see figure 2.6). Therefore, the optimal trade-off between switching and harmonic losses remains unchanged. If IGBTs are adopted, the optimal switching frequency values are 17 kHz for the continuous modulations technique and 30 kHz for the discontinuous one. If SiC MOSFETs are considered, the optimal f_{sw} value turns out to be 36 kHz for the 7-segment SVM and 71 kHz for the 5-segment SVM.

Overall, the influence of the individual design variables on the total system efficiency may be summarized by the following considerations:

- $\boldsymbol{f_{\mathrm{sw}}}$ has a considerable impact on the system losses. This can be inferred by the wide distribution of the design points on the (η, N_{par}) plane. Therefore, choosing the optimal switching frequency value is of utmost importance.

- increasing $\boldsymbol{N_{\mathrm{par}}}$ has a limited influence on the system efficiency and its benefit rapidly fades. One reason is that semiconductor losses represent only a limited part of the system total loss. Moreover, the switching loss behaviour becomes more linear for low current values, thus nullifying the benefit of increasing N_{par}.

- the **device** choice is the most influential factor, since selecting a SiC MOSFET over a conventional IGBT drastically reduces the inverter switching losses. This also changes the balance between switching and harmonic losses, thus pushing the optimal switching frequency to higher values. However this design choice come with the drawback of a higher converter cost.

- the **modulation technique** does not have a strong impact on the system efficiency, because of the inherent trade-off between lower switching frequency and higher harmonic distortion. However, a modest overall performance increase is provided by the 5-segment technique compared to the 7-segment one, as highlighted in chapter 3.

- the **control strategy** has a moderate influence on the system efficiency. This impact is higher if SiC MOSFETs are adopted, since the inverter losses decrease and the system MTPL shifts away from the MTPA.

Table 5.3: Overview of the two designs combinations selected for the comparison.

	Conventional	**Optimized**
Switching frequency f_{sw}	10 kHz	71 kHz
Semiconductor device	IGBT	SiC MOSFET
Number of devices in parallel N_{par}	12	12
Modulation technique (SVM)	7-segment	5-segment
Control strategy	MTPA	MTPL

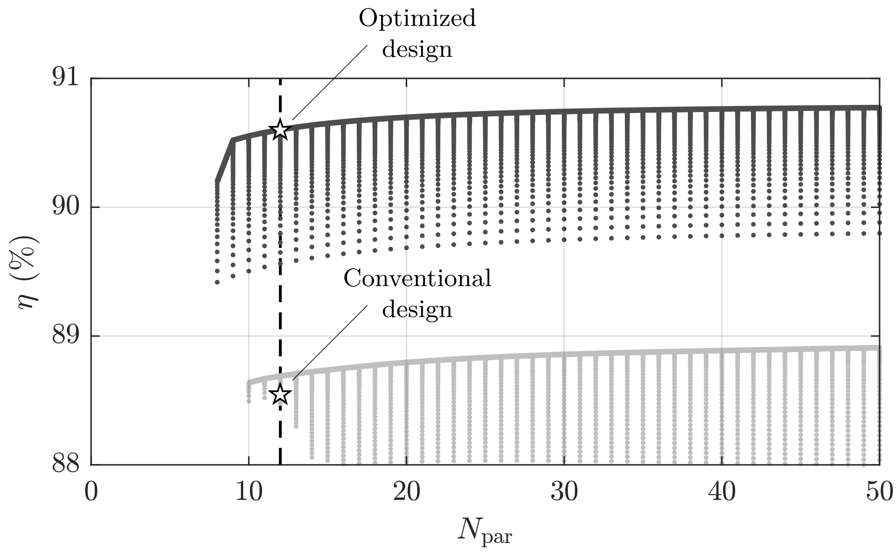

Figure 5.8: Highlight of the two designs selected for the comparison.

5.4 Case Study

To better highlight the performance enhancement resulting from the proposed system-level optimization procedure, a conventional design is compared to an optimized one. The same number of paralleled semiconductor devices per switch has been assumed, in order to have the same inverter physical dimension. The conventional design is based on 12 paralleled Infineon AIKW50N65DF5 IGBT devices per switch, the standard 7-segment SVM technique and a 10 kHz switching frequency. Moreover, a MTPA motor control strategy is adopted. This design has been selected to represent the current industry standard. The optimized design is extracted from the best Pareto front and consists of 12 paralleled ROHM SCT3022AL MOSFET devices per switch, the proposed optimal-clamping 5-segment SVM technique and a 71 kHz switching frequency, while adopting the system-level MTPL motor control strategy. The main characteristics of the two chosen designs are summarized in table 5.3. Moreover, their performance difference is highlighted in figure 5.8, where the two designs are identified in the (η, N_{par}) plane.

To get a better understanding of the performance difference between the two designs, a comparison of the system losses and efficiency can be carried out over the full (T, n) plane. Figures 5.9 and 5.10 show the system loss and efficiency maps respectively, as a function of the motor torque and speed. While only a slight difference between the conventional and the optimized design may be noted from the loss maps, efficiency is much better suited to highlight their performance gap.

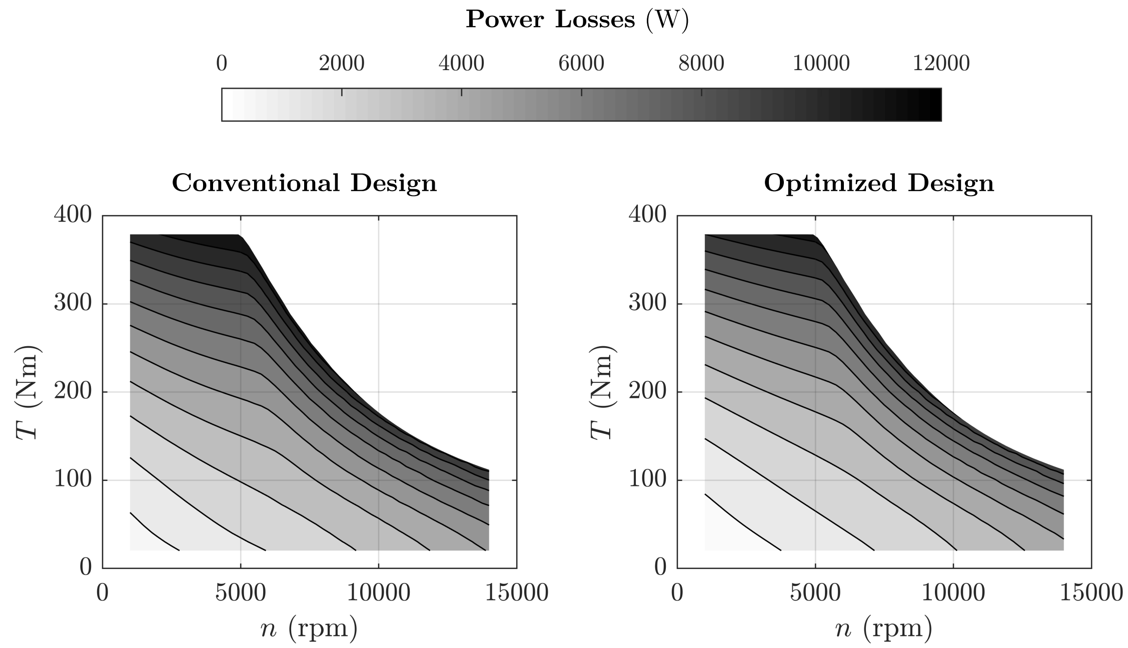

Figure 5.9: Power loss comparison between the two proposed designs on the (T, n) plane.

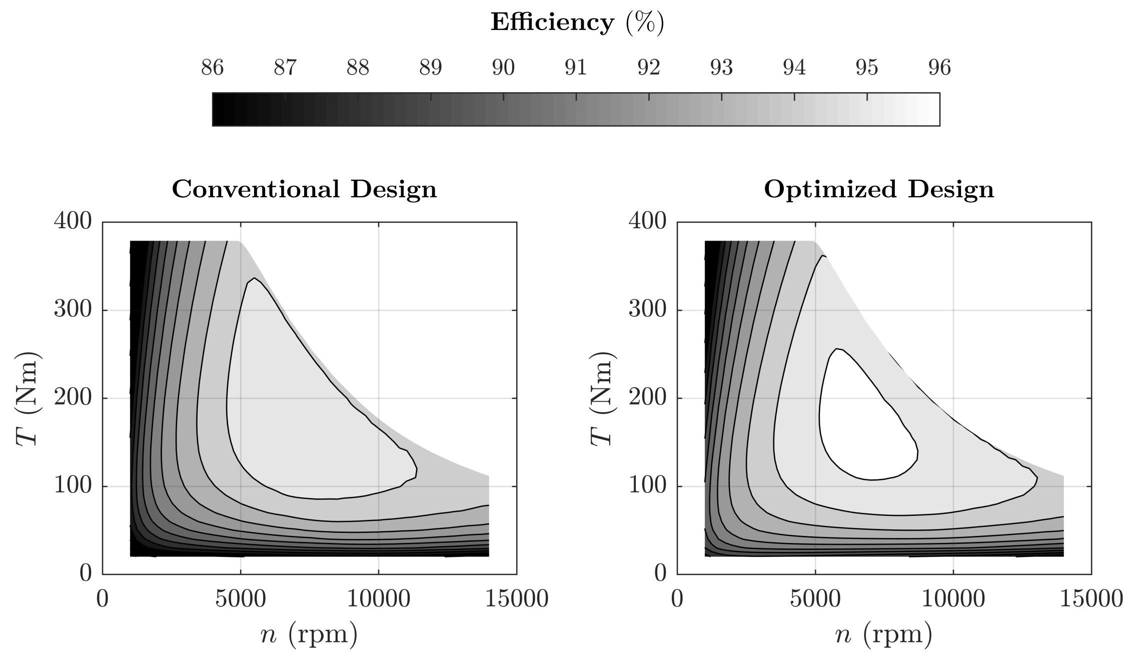

Figure 5.10: Efficiency comparison between the two proposed designs on the (T, n) plane.

Table 5.4: Overview of the design comparison results.

	Conventional	**Optimized**
Total losses	516 Wh	414 Wh
Loss gain	-	-19.8 %
Average efficiency	88.5 %	90.6 %
Efficiency gain	-	$+2.1$ %

According to the results, the optimized design better performs over the full plane, reaching a maximum combined inverter and motor efficiency of 96 % in a limited region.

Overall, an average efficiency gain of 2.1 % is obtained during the WLTC class 3 driving cycle, together with an almost 20 % energy loss reduction. These results are summarized in table 5.4. It may thus be concluded that combining the best design choices can have a substantial impact on the overall system efficiency. Therefore, the system-level optimization procedure is proven to be valuable.

Chapter 6

Conclusion

In this thesis, a system-level efficiency optimization procedure of an electric vehicle drive train has been proposed. The main goal was to provide a comprehensive approach to the optimal system design and control, while understanding and clarifying the most relevant system loss mechanisms. This analysis has also allowed to determine and quantify the various interactions between subsystems, showing that a change in the power converter design has an indirect impact on the machine losses.

Therefore, an automatic design procedure of a traction inverter that meets the vehicle performance requirements and optimizes the drive train efficiency by means of a minimum system-loss control strategy has been described. Despite being based on a specific case study, the here built subsystem models and optimization tools have broader validity, making the proposed method suitable for a wide range of applications.

6.1 Summary

A short summary of the topics discussed in this thesis is here provided.

In **chapter 1** an introduction to the main subject of the dissertation has been carried out. A brief problem statement and the description of the main goals of the work have been given.

In **chapter 2** the inverter model has been derived. A three-phase 2-level VSI topology has been selected. An Infineon AIKW50N65DF5 IGBT and a ROHM SCT3022AL SiC MOSFET have been chosen for a performance comparison between different power device technologies. Making use of the available manufacturer data, a semiconductor loss model has been built, in order to enable the evaluation of both conduction and switching losses of a generic power device. An inverter thermal model from the semiconductor chip to the liquid-cooled heat sink has also been derived, to estimate the semiconductor device junction temperature during operation. This has been exploited to properly determine the minimum number of paralleled devices per switch of the inverter as a function of the worst-case current. Furthermore, a duty cycle and voltage waveform generation tool has been built and two different inverter modulation techniques have been implemented (i.e. a 7-segment continuous SVM and an optimal loss clamping 5-segment discontinuous SVM). This tool computes the inverter switch duty cycles and generates the output phase voltage waveforms as a function of electrical frequency, switching frequency and reference output voltage value.

Combining the semiconductor loss model and the voltage waveform generation tool, the inverter losses and output harmonic distortion have been derived for generic load conditions (i.e. combination of voltage, current and power factor angle) and operating switching frequencies. Finally, a performance comparison between the two modulation techniques, concerning output voltage harmonic distortion and semiconductor device power losses, has been provided.

In **chapter 3** the electrical machine loss mechanisms have been investigated and the motor model has been derived. An available motor from Brusa Elektronik AG has been chosen for the case-study. The main advantages of the selected PMASR machine topology have been pointed out and its electrical and magnetic equations have been illustrated. Then, the motor flux and torque maps have been extracted by means of finite element analysis and the peculiar magnetic behaviour of the machine has been highlighted. Moreover, inverter voltage and current limits have been translated into boundary conditions for the motor operating region in the dq current plane. Therefore, maximum torque-speed and power-speed curves of the machine have been extracted as a function of the inverter rated current. Next, motor fundamental loss mechanisms have been described and evaluated, by means of both finite element analysis and measurements, starting from copper losses, iron losses and permanent magnet losses, together with mechanical friction losses. A major part of the chapter has been dedicated to the inverter-induced time harmonic loss component of the motor. A simplified model, based on the high-frequency machine impedance, has been derived and has therefore been exploited to evaluate the effect of the two different modulation techniques on the additional inverter-induced motor losses.

In **chapter 4** a vehicle model has been built, in order to provide the necessary specifics for the inverter dimensioning and some realistic drive train operating conditions for the system-level optimization procedure. The most relevant equations regarding dynamical resistance to motion have been described, therefore the necessary force to move the vehicle in different operating conditions has been derived. Tesla Model 3 has been selected as reference vehicle for the investigation and its main data and performance specifics have been provided. Both maximum-speed constraints on a flat and a uphill road have been verified to lie under the motor S1 (i.e. continuous operation) torque-speed characteristic. Moreover, the vehicle acceleration requirement has proven to be the worst-case load condition and has thus defined the inverter rated current $I_{\max} = 750$ A. The standardized WLTC class 3 driving cycle profile has been selected for the operating condition investigation. The vehicle dynamical model has been exploited to identify the cloud of most relevant application-specific drive train working points. These points have then been clustered and gathered together into a lower number of time-weighted representative points, to be employed in the subsequent system-level efficiency optimization procedure.

In **chapter 5** the model-based system-level efficiency optimization has been developed and detailed. The loss models of the power converter and the electrical machine, derived in the previous chapters, have been interlinked, enabling the power loss calculation for the complete drive train system as a function of the operating condition and the chosen switching frequency. The switching frequency value which optimizes the trade-off between inverter switching losses and motor harmonic losses has been found to be highly dependent on the inverter design (i.e. choice of semiconductor technology, number of paralleled devices per switch, modulation technique) and the working load point (i.e. output voltage and current). Maps of these dependences have been shown and explained. Furthermore, the derived loss models have allowed to extract both inverter and motor losses as a function of the machine direct and quadrature axis currents and rotational speed (i_d, i_q, n). By combining these loss maps, a maximum system efficiency motor control strategy has been derived and compared to more conventional strategies such as maximum-torque-per-ampere (MTPA) and machine-only maximum-torque-per-loss (MTPL). As a result, the whole motor torque-speed operating range has been mapped by means of minimum system loss trajectories in the dq current plane and the overall loss distribution has been illustrated. With the availability of the relevant drive train working points, the subsystem loss models and the optimal control strategy, the system-level efficiency optimization procedure has been performed and the resulting set of optimal inverter designs has been represented by means of efficiency vs cost (η - €) Pareto fronts. One curve has been extracted for each semiconductor technology, inverter modulation technique and machine control strategy, while identifying the loss-optimal inverter switching frequency in each case. The results have shown that this frequency value drastically depends on the inverter design combination, reaching values higher than 70 kHz if SiC MOSFET adoption is combined with a discontinuous modulation strategy, while remaining below 30 kHz if Si IGBTs are used. Finally, one out of the multiple Pareto-optimal inverter designs has been selected (12 SiC MOSFETs per switch, 5-segment SVM technique, $f_{\text{sw}} = 71$ kHz) and the total drive train efficiency performance has been evaluated along the considered driving cycle, while adopting the proposed system-level MTPL motor control strategy. These results have been compared to a conventional non-optimized inverter design (12 IGBTs per switch, 7-segment SVM technique, $f_{\text{sw}} = 10$ kHz) with a standard motor control strategy (MTPA), to highlight the achievable system efficiency improvements. Overall, an average efficiency gain of 2.1 % has been obtained by the optimized design, together with an almost 20 % energy loss reduction over the complete driving cycle. Therefore, the system-level optimization procedure has proven to be valuable.

6.2 Outlook

While a broad variety of topics has been covered in this dissertation, still several aspects have been left out and could be implemented in a both more accurate and wider-level optimization procedure. Some of the remaining open topics are hereby listed:

- additional performance indices besides efficiency, such as power density (i.e. volume, weight) and cost, could be analysed and considered, extending the purpose of the optimal design procedure. A higher number of design variables and multiple "cost" functions would have to be considered, translating in a so-called multi-objective optimization. This procedure would require accurate knowledge of quantities outside the power losses and would thus drastically increase the modeling effort.

- the loss dependence on temperature should be taken into account, both for the inverter and the motor. Lower junction temperature values considerably reduce semiconductor losses, thus increasing the benefit of a better cooling system and a higher number of devices in parallel. Moreover, temperature has a substantial impact on the machine copper losses, which represent the biggest loss component of the drive train in most of the operating region.

- other inverter topologies, besides the 2-level VSI, could be considered in the analysis. This has already been done to a certain extent in [3], however an extension could be made including current source inverters (CSI) and n-level topologies adopting a high number of cheap low-voltage MOSFET devices.

- the influence of changing switching frequency on the system filtering components, such as the input DC-link capacitor or the common-mode choke, should be evaluated. Higher switching frequencies have a beneficial impact on these devices in terms of volume, weight and cost. Therefore, with the availability of accurate filter models, the overall system benefit of an increased switching frequency could be assessed.

- finally, a comprehensive system optimization, embracing also the electrical machine in the design procedure, is still missing in literature. While being an extremely challenging task to approach, the benefits of designing together motor and power converter could be substantial. For instance, increasing the motor rotational speed directly translates in a machine size and cost reduction, but this can only be achieved by means of a concurrent increase of the inverter switching frequency.

Bibliography

[1] E. Levi, "Multiphase Electric Machines for Variable-Speed Applications," *IEEE Transactions on Industrial Electronics*, vol. 55, pp. 1893–1909, May 2008.

[2] R. Bojoi, A. Cavagnino, A. Tenconi, A. Tessarolo, and S. Vaschetto, "Multiphase electrical machines and drives in the transportation electrification," in *2015 IEEE 1st International Forum on Research and Technologies for Society and Industry Leveraging a better tomorrow (RTSI)*, pp. 205–212, Sept. 2015.

[3] M. Schweizer, *System-Oriented Efficiency Optimization of Variable Speed Drives*. PhD thesis, ETH Zurich, 2012.

[4] R. Teichmann and S. Bernet, "A comparison of three-level converters versus two-level converters for low-voltage drives, traction, and utility applications," *IEEE Transactions on Industry Applications*, vol. 41, pp. 855–865, May 2005.

[5] J. Biela, M. Schweizer, S. Waffler, and J. W. Kolar, "SiC versus Si - Evaluation of Potentials for Performance Improvement of Inverter and DC-DC Converter Systems by SiC Power Semiconductors," *IEEE Transactions on Industrial Electronics*, vol. 58, pp. 2872–2882, July 2011.

[6] Infineon Technologies, *AIKW50N65DF5 datasheet*, June 2017. Available: https://www.infineon.com.

[7] ROHM Semiconductor, *SCT3022AL datasheet*, Aug. 2017. Available: http://www.rohm.com.

[8] A. Wintrich, U. Nicolai, W. Tursky, and T. Reimann, *Application Manual Power Semiconductors*. SEMIKRON, 2015.

[9] Y. Khersonsky, M. Robinson, and D. Gutierrez, *Application Note AN-989: The HEXFRED Ultrafast Diode in Power Switching Circuits*. International Rectifier, 1992.

[10] Electrolube, *HTC datasheet*, 2013. Available: https://www.electrolube.com.

[11] MeccAl, *LCP 180x20 datasheet*, 2017. Available: http://www.meccal.com.

[12] J. Holtz, "Pulsewidth modulation for electronic power conversion," *Proceedings of the IEEE*, vol. 82, pp. 1194–1214, Aug. 1994.

[13] D. G. Holmes and T. A. Lipo, *Pulse Width Modulation for Power Converters: Principles and Practice.* No. 2 in IEEE Press series on power engineering, Piscataway, NJ: IEEE Press, 2003. OCLC: 248797580.

[14] B. Wu, *High-Power Converters and AC Drives.* Hoboken, NJ, USA: John Wiley & Sons, Inc., Feb. 2006. DOI: 10.1002/0471773719.

[15] K. Zhou and D. Wang, "Relationship between space-vector modulation and three-phase carrier-based PWM: a comprehensive analysis," *IEEE Transactions on Industrial Electronics*, vol. 49, pp. 186–196, Feb. 2002.

[16] J. W. Kolar, H. Ertl, and F. C. Zach, "Influence of the modulation method on the conduction and switching losses of a PWM converter system," *IEEE Transactions on Industry Applications*, vol. 27, pp. 1063–1075, Nov. 1991.

[17] A. M. Hava, R. J. Kerkman, and T. A. Lipo, "A high-performance generalized discontinuous PWM algorithm," *IEEE Transactions on Industry Applications*, vol. 34, pp. 1059–1071, Sept. 1998.

[18] M. Bierhoff, H. Brandenburg, and F. W. Fuchs, "An Analysis on Switching Loss Optimized PWM Strategies for Three Phase PWM Voltage Source Converters," in *IECON 2007 - 33rd Annual Conference of the IEEE Industrial Electronics Society*, pp. 1512–1517, Nov. 2007.

[19] P. Guglielmi, M. Pastorelli, G. Pellegrino, and A. Vagati, "Position-sensorless control of permanent-magnet-assisted synchronous reluctance motor," *IEEE Transactions on Industry Applications*, vol. 40, pp. 615–622, Mar. 2004.

[20] G. Pellegrino, A. Vagati, P. Guglielmi, and B. Boazzo, "Performance Comparison Between Surface-Mounted and Interior PM Motor Drives for Electric Vehicle Application," *IEEE Transactions on Industrial Electronics*, vol. 59, pp. 803–811, Feb. 2012.

[21] G. Pellegrino, A. Vagati, B. Boazzo, and P. Guglielmi, "Comparison of Induction and PM Synchronous Motor Drives for EV Application Including Design Examples," *IEEE Transactions on Industry Applications*, vol. 48, pp. 2322–2332, Nov. 2012.

[22] G. Pellegrino, A. Vagati, and P. Guglielmi, "Design Tradeoffs Between Constant Power Speed Range, Uncontrolled Generator Operation, and Rated Current of IPM Motor Drives," *IEEE Transactions on Industry Applications*, vol. 47, pp. 1995–2003, Sept. 2011.

[23] BRUSA Elektronik AG, *HSM1 - Hybrid Synchronous Motor*, June 2015. Available: http://www.brusa.biz.

[24] E. Armando, P. Guglielmi, G. Pellegrino, M. Pastorelli, and A. Vagati, "Accurate Modeling and Performance Analysis of IPM-PMASR Motors," *IEEE Transactions on Industry Applications*, vol. 45, pp. 123–130, Jan. 2009.

[25] N. Bianchi and S. Bolognani, "Magnetic models of saturated interior permanent magnet motors based on finite element analysis," in *Conference Record of 1998 IEEE Industry Applications Conference. Thirty-Third IAS Annual Meeting (Cat. No.98CH36242)*, vol. 1, pp. 27–34 vol.1, Oct. 1998.

[26] A. Vagati, M. Pastorelli, F. Scapino, and G. Franceschini, "Impact of cross saturation in synchronous reluctance motors of the transverse-laminated type," *IEEE Transactions on Industry Applications*, vol. 36, pp. 1039–1046, July 2000.

[27] B. Stumberger, G. Stumberger, D. Dolinar, A. Hamler, and M. Trlep, "Evaluation of saturation and cross-magnetization effects in interior permanent-magnet synchronous motor," *IEEE Transactions on Industry Applications*, vol. 39, pp. 1264–1271, Sept. 2003.

[28] E. Armando, R. I. Bojoi, P. Guglielmi, G. Pellegrino, and M. Pastorelli, "Experimental Identification of the Magnetic Model of Synchronous Machines," *IEEE Transactions on Industry Applications*, vol. 49, pp. 2116–2125, Sept. 2013.

[29] E. Armando, P. Guglielmi, G. Pellegrino, and R. Bojoi, "Flux linkage maps identification of synchronous AC motors under controlled thermal conditions," in *2017 IEEE International Electric Machines and Drives Conference (IEMDC)*, pp. 1–8, May 2017.

[30] R. Bojoi, A. Cavagnino, M. Cossale, and S. Vaschetto, "Methodology for the IPM motor magnetic model computation based on finite element analysis," in *IECON 2014 - 40th Annual Conference of the IEEE Industrial Electronics Society*, pp. 722–728, Oct. 2014.

[31] A. Krings, *Iron Losses in Electrical Machines - Influence of Material Properties, Manufacturing Processes and Inverter Operation.* PhD thesis, KTH, Stockholm, Apr. 2014.

[32] D. W. Novotny and S. A. Nasar, *High Frequency Losses in Induction Motors.* NASA Contract Report, June 1991.

[33] A. Boglietti, P. Ferraris, M. Lazzari, and F. Profumo, "Iron losses in magnetic materials with six-step and PWM inverter supply," *IEEE Transactions on Magnetics*, vol. 27, pp. 5334–5336, Nov. 1991.

[34] A. Boglietti, P. Ferraris, M. Lazzari, and F. Profumo, "Effects of different modulation index on the iron losses in soft magnetic materials supplied by PWM inverter," *IEEE Transactions on Magnetics*, vol. 29, pp. 3234–3236, Nov. 1993.

[35] A. Boglietti, P. Ferraris, M. Lazzari, and M. Pastorelli, "Change of the iron losses with the switching supply frequency in soft magnetic materials supplied by PWM inverter," *IEEE Transactions on Magnetics*, vol. 31, pp. 4250–4252, Nov. 1995.

[36] A. Boglietti, P. Ferraris, M. Lazzari, and M. Pastorelli, "Influence of the inverter characteristics on the iron losses in PWM inverter-fed induction motors," *IEEE Transactions on Industry Applications*, vol. 32, pp. 1190–1194, Sept. 1996.

[37] A. Boglietti, O. Bottauscio, M. Chiampi, M. Pastorelli, and M. Repetto, "Computation and measurement of iron losses under PWM supply conditions," *IEEE Transactions on Magnetics*, vol. 32, pp. 4302–4304, Sept. 1996.

[38] A. Boglietti, A. Cavagnino, M. Lazzari, and M. Pastorelli, "Predicting iron losses in soft magnetic materials with arbitrary voltage supply: an engineering approach," *IEEE Transactions on Magnetics*, vol. 39, pp. 981–989, Mar. 2003.

[39] A. Boglietti, A. Cavagnino, D. M. Ionel, M. Popescu, D. A. Staton, and S. Vaschetto, "A General Model to Predict the Iron Losses in PWM Inverter-Fed Induction Motors," *IEEE Transactions on Industry Applications*, vol. 46, pp. 1882–1890, Sept. 2010.

[40] K. Bradley, W. Cao, J. Clare, and P. Wheeler, "Predicting Inverter-Induced Harmonic Loss by Improved Harmonic Injection," *IEEE Transactions on Power Electronics*, vol. 23, pp. 2619–2624, Sept. 2008.

[41] F. G. G. d. Buck, P. Giustelinck, and D. d. Backer, "A Simple but Reliable Loss Model for Inverter-Supplied Induction Motors," *IEEE Transactions on Industry Applications*, vol. IA-20, pp. 190–202, Jan. 1984.

[42] H. Polinder, *On the Losses in a High-Speed Permanent-Magnet Generator with Rectifier*. PhD thesis, TU Delft, June 1998.

[43] A. Carrer, *Note di Elettrotecnica*. Levrotto & Bella, 1963.

[44] R. L. Stoll, *The analysis of eddy currents*. Clarendon Press, 1974.

[45] P. W. Wheeler, J. C. Clare, M. Apap, and K. J. Bradley, "Harmonic Loss Due to Operation of Induction Machines From Matrix Converters," *IEEE Transactions on Industrial Electronics*, vol. 55, pp. 809–816, Feb. 2008.

[46] M. Ehsani, K. M. Rahman, and H. A. Toliyat, "Propulsion system design of electric and hybrid vehicles," *IEEE Transactions on Industrial Electronics*, vol. 44, pp. 19–27, Feb. 1997.

[47] United Nations Economic Commission for Europe (UNECE), *Development of a Worldwide harmonized Light duty driving Test Cycle (WLTC)*, Dec. 2013. Available: https://www.unece.org.

[48] E. Carraro, M. Morandin, and N. Bianchi, "Traction PMASR Motor Optimization According to a Given Driving Cycle," *IEEE Transactions on Industry Applications*, vol. 52, pp. 209–216, Jan. 2016.

[49] J. W. Kolar, U. Drofenik, J. Biela, M. L. Heldwein, H. Ertl, T. Friedli, and S. D. Round, "PWM converter power density barriers," pp. P–9–P–29, IEEE, Apr. 2007.

[50] J. W. Kolar, J. Biela, S. Waffler, T. Friedli, and U. Badstuebner, "Performance trends and limitations of power electronic systems," in *2010 6th International Conference on Integrated Power Electronics Systems*, pp. 1–20, Mar. 2010.

[51] P. Famouri and J. J. Cathey, "Loss minimization control of an induction motor drive," in *Conference Record of the IEEE Industry Applications Society Annual Meeting,*, pp. 226–231 vol.1, Oct. 1989.

[52] R. D. Lorenz and S. M. Yang, "Efficiency-optimized flux trajectories for closed-cycle operation of field-orientation induction machine drives," *IEEE Transactions on Industry Applications*, vol. 28, pp. 574–580, May 1992.

[53] I. Kioskeridis and N. Margaris, "Loss minimization in induction motor adjustable-speed drives," *IEEE Transactions on Industrial Electronics*, vol. 43, pp. 226–231, Feb. 1996.

[54] F. Abrahamsen, F. Blaabjerg, J. K. Pedersen, P. Z. Grabowski, and P. Thogersen, "On the energy optimized control of standard and high-efficiency induction motors in CT and HVAC applications," *IEEE Transactions on Industry Applications*, vol. 34, pp. 822–831, July 1998.

[55] A. Mannan, T. Murata, J. Tamura, and T. Tsuchiya, "Efficiency optimized speed control of field oriented induction motor including core loss," in *Proceedings of the Power Conversion Conference-Osaka 2002 (Cat. No.02TH8579)*, vol. 3, pp. 1316–1321 vol.3, 2002.

[56] S. A. Odhano, R. Bojoi, A. Boglietti, . G. Roşu, and G. Griva, "Maximum Efficiency per Torque Direct Flux Vector Control of Induction Motor Drives," *IEEE Transactions on Industry Applications*, vol. 51, pp. 4415–4424, Nov. 2015.

[57] S. Morimoto, Y. Tong, Y. Takeda, and T. Hirasa, "Loss minimization control of permanent magnet synchronous motor drives," *IEEE Transactions on Industrial Electronics*, vol. 41, pp. 511–517, Oct. 1994.

[58] S. Vaez, V. I. John, and M. A. Rahman, "An on-line loss minimization controller for interior permanent magnet motor drives," *IEEE Transactions on Energy Conversion*, vol. 14, pp. 1435–1440, Dec. 1999.

[59] C. Mademlis, I. Kioskeridis, and N. Margaris, "Optimal efficiency control strategy for interior permanent-magnet synchronous motor drives," *IEEE Transactions on Energy Conversion*, vol. 19, pp. 715–723, Dec. 2004.

[60] Z. Biel, J. Vittek, and M. Hrkel, "Permanent magnet synchronous motor loss minimization control strategies," in *2012 ELEKTRO*, pp. 165–169, May 2012.

[61] J. Goss, M. Popescu, D. Staton, R. Wrobel, J. Yon, and P. Mellor, "A comparison between maximum torque/ampere and maximum efficiency control strategies in IPM synchronous machines," in *2014 IEEE Energy Conversion Congress and Exposition (ECCE)*, pp. 2403–2410, Sept. 2014.

[62] T. Jerčic, D. Žarko, J. Matuško, and M. Martinovic, "Minimum loss control of interior permanent magnet traction motor," in *2015 IEEE International Electric Machines Drives Conference (IEMDC)*, pp. 992–998, May 2015.

[63] G. S. Li, J. F. Xie, and L. Y. Xu, "Maximum efficiency control method of permanent magnet synchronous motor based on three-dimensional table," in *2015 International Conference on Advanced Mechatronic Systems (ICAMechS)*, pp. 392–396, Aug. 2015.

[64] Q. Guo, C. Zhang, L. Li, J. Zhang, and M. Wang, "Maximum Efficiency per Torque Control of Permanent-Magnet Synchronous Machines," *Applied Sciences*, vol. 6, p. 425, Dec. 2016.

[65] F. Abrahamsen, *Energy Optimal Control of Induction Motor Drives.* PhD thesis, Aalborg University, 2000.

[66] F. Abrahamsen, F. Blaabjerg, J. K. Pedersen, and P. B. Thoegersen, "Efficiency-optimized control of medium-size induction motor drives," *IEEE Transactions on Industry Applications*, vol. 37, pp. 1761–1767, Nov. 2001.

[67] O. Wallmark, "On Control of Permanent-Magnet Synchronous Motors in Hybrid-Electric Vehicle Applications," Master's thesis, Chalmers University of Technology, 2004.

[68] D. Pohlenz and J. Böcker, "Efficiency improvement of an IPMSM using Maximum Efficiency operating strategy," in *Proceedings of 14th International Power Electronics and Motion Control Conference EPE-PEMC 2010*, pp. T5–15–T5–19, Sept. 2010.

[69] O. S. Ebrahim, M. A. Badr, A. S. Elgendy, and P. K. Jain, "ANN-Based Optimal Energy Control of Induction Motor Drive in Pumping Applications," *IEEE Transactions on Energy Conversion*, vol. 25, pp. 652–660, Sept. 2010.

[70] T. Windisch and W. Hofmann, "Loss minimization of an IPMSM drive using pre-calculated optimized current references," in *IECON 2011 - 37th Annual Conference of the IEEE Industrial Electronics Society*, pp. 4704–4709, Nov. 2011.